

AD-A081 253

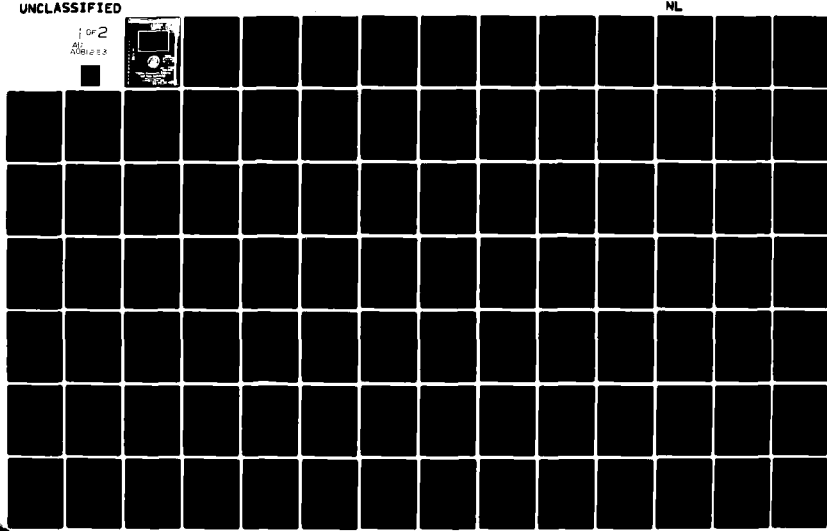
VIRGINIA POLYTECHNIC INST AND STATE UNIV BLACKSBURG D--ETC F/0 17/1
ADAPTIVE TARGET TRACKING FOR UNDERWATER MANEUVERING TARGETS.(U)

DEC 79 R L MOOSE N00014-77-C-0164

NL

UNCLASSIFIED

1 of 2
Alt
Alt 2 E.S.



NR 17273
C&H 431

FINAL REPORT

ADAPTIVE TARGET TRACKING FOR
UNDERWATER MANEUVERING TARGETS

(10) RICHARD L. MOOSE

PRINCIPAL INVESTIGATOR

DENIS H. McCABE

RESEARCH ASSOCIATE

CONTRACT NUMBER

(15) N00014-77-C-0164 Rev

(11) [REDACTED]
1 Dec 9 1979

(12) 10/4/

DEPARTMENT OF ELECTRICAL ENGINEERING
VIRGINIA POLYTECHNIC INSTITUTE AND STATE UNIVERSITY
BLACKSBURG, VA 24061



DISTRIBUTION STATEMENT A
Approved for public release
Distribution Unlimited

411053

ABSTRACT

This report examines the problem of adaptively tracking a maneuvering submarine in two dimensional space utilizing passive time delay and Doppler frequency measurements of unknown or randomly varying center frequencies. The target is free to maneuver in velocity and depth with tracking being done in the vertical plane. It is pointed out how to incorporate bearing measurements into the present polar model to achieve a three dimensional target tracking capability.

SEARCHED _____
INDEXED _____
FILED _____
SERIALIZED _____
FILED _____
JULY 1968
FBI - LOS ANGELES
Letter on file
Dist. _____ Special _____
A

T A B L E O F C O N T E N T S

Chapter 1 - INTRODUCTION

Chapter 2 - UNDERWATER PASSIVE TRACKING. INTRODUCTION AND LINEARIZED POLAR MODEL FOR THE MANEUVERING OBSERVER-SOURCE SCENARIO

Chapter 3 - PASSIVE TRACKING USING SONAR TIME DELAYS. THE ADAPTIVE EXTENDED POLAR KALMAN FILTER.

Chapter 4 - PASSIVE TRACKING OF SOURCE RELATIVE RADIAL VELOCITY PROFILE USING THE DOPPLER EFFECT AND KNOWN CONSTANT CENTER FREQUENCY

Chapter 5 - PASSIVE TRACKING OF SOURCE RADIAL VELOCITY USING THE DOPPLER EFFECT IN THE PRESENCE OF A RANDOMLY VARYING CENTER FREQUENCY

Chapter 6 - THE INTEGRATED ADAPTIVE DOPPLER FREQUENCY-REDUCED ORDER SONAR TIME DELAY TRACKING FILTER

Summary

Chapter 1

1.1 Introduction

During the past several years much effort has been spent in the development of sophisticated digital filtering algorithms for tracking maneuvering targets. A common method has been to model the target dynamics in a rectangular coordinate system which results in a linear set of state equations, but forces the measurements to be nonlinear functions of the state variables. With this model an extended Kalman filtering algorithm is frequently used both to provide current state variable estimates and, by a one-step prediction process, to linearize the next measurement vector. This method works moderately well until the target makes an abrupt change in its trajectory in response to pilot or missile-guidance program commands. In this situation the velocity and position estimates can, and often do, diverge from the true unknown values. The inherent problems of this approach can lead to large bias errors and sometimes complete filter divergence.

Earlier work on the maneuvering target tracking problem includes Jazwinski's limited memory filtering [1], in which the filter gains are prevented from decaying to zero. Another technique, described by Thorp [2], involves switching between two Kalman filters in response to a detected maneuver. A third approach, due to Singer [3], models the target trajectory as a response of the target model to a time-correlated random acceleration. With this method additional

state variables are used to generate the correlated forcing functions which, in turn, increase the dimension of the Kalman filtering algorithm. In this manner the technique provides the filter with statistical information concerning target maneuvers based on an assumed range of possible accelerations. Singer's method was subsequently extended by many others.

Parallel to the effort was the method of modeling major changes in target trajectories by a semi-Markov process. An application of this approach to tracking maneuvering targets in two-dimensions by Moose [4] was successfully extended by Gholson and Moose [5] to three-dimensional tracking.

The general approach which uses the "adaptive semi-Markov maneuver model" of [4] and [5] implies a discretization of possible vehicle accelerations or velocities. The estimation algorithm then views the maneuvering vehicle as if it is responding to commands which are modeled by a semi-Markov process, i.e., a random process with a finite number of "states" (commands) which are selected according to the transition probabilities of a Markov process. A semi-Markov process differs from a Markov process in that the duration of time in one state prior to switching to another state is itself a random variable [6]. Incorporating the semi-Markov concept into a Bayesian estimator of [4] and [5]. This estimation algorithm provides a substantial improvement in filter stability, which means that large bias errors are prevented from being built up due to unmodeled target accelerations. An important aspect of this adaptive estimation algorithm is its elimination of a "growing memory" which is prevalent in many adaptive filters.

1.2 Target Modeling

With the brief history of the maneuvering target tracking problem presented in the previous section, we see a general progression in the sophistication of tracking filter design stemming primarily from the method in which the unknown target accelerations are modeled. This trend is graphically outlined in Figure 1.1

Initially, target maneuvers were modeled as the response to uncorrelated, zero-mean variations about a nonaccelerating target, shown in Figure 1(A). As a result, the estimation algorithm could follow only those maneuvers which were comparable with the input noise level. Furthermore, the filtering results during nonmaneuvering situations were seriously degraded due to the uncorrelated input noise. As shown in Figure 1(B), Singer [3] attempted to model large-scale maneuvers by assuming a time-correlated input process and incorporating the statistics into the subsequent filter design. In Figure 1(C) large-scale target maneuvers were modeled as a stochastic process whose mean-value switched randomly from among a finite set of predetermined values. The adaptive estimation algorithm mentioned in the previous section could then be used to track the maneuvering target. This method was seriously restricted, however, by the requirement of a large number of preselected mean values in order to ensure convergence of the estimation process. In this report we show that by combining the concepts illustrated in Figure 1(B) and Figure 1(C) the number of mean values required to prevent filter divergence is greatly reduced. This combination is illustrated in Figure 1(D). The primary benefit of this approach is the large saving in computational effort. An additional benefit, at least from a subjective viewpoint, is that the

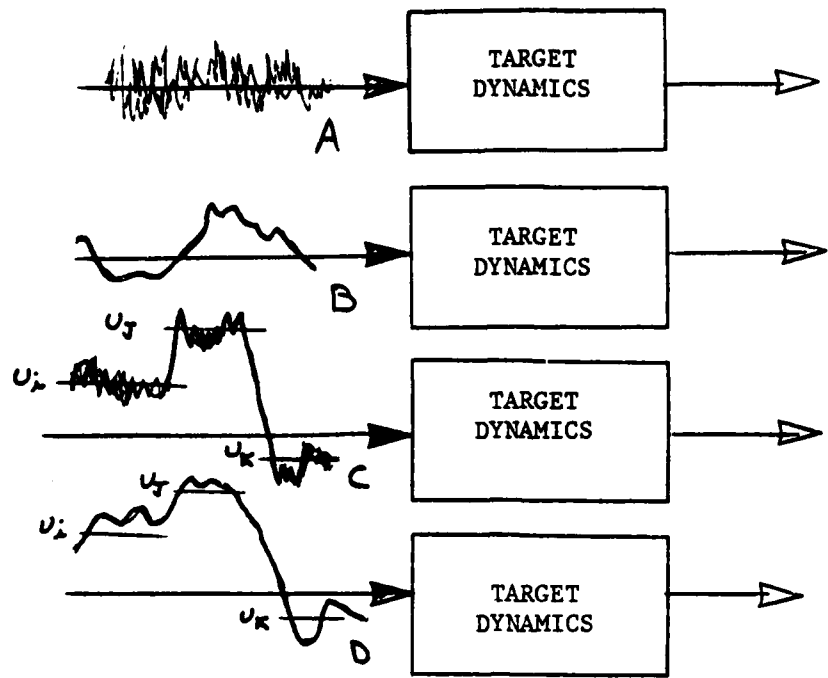


Figure 1.1. Historical development of maneuvering target model inputs.
 (A) Zero-mean white Gaussian plant disturbance. (B) Correlated, zero-mean plant disturbance. (C) White Gaussian noise with randomly switching mean. (D) Correlated Gaussian noise with randomly switching mean.

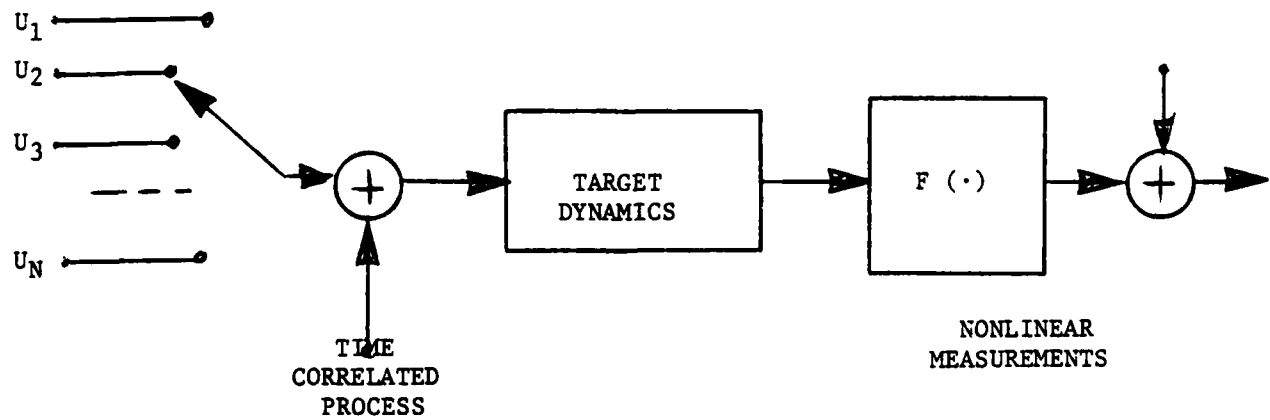


Figure 1.2. Target motion model.

time-correlated, randomly switching, mean-forcing function more adequately models real-world target maneuvers.

The basic target modeling ideas are shown in Figure 1.2. The target trajectory is generated by the random selection of an input time-correlated Gaussian process whose mean value u_i is applied to the target plant dynamics for a random duration of time. This input disturbance process lasts until a new input u_j is randomly chosen from among a finite set of n possible inputs. With this model as a background and using an appropriate choice of state variable equations to represent target dynamics, either submarine or aircraft, it is possible to develop an "optimal" (in the minimum mean-square error sense) tracking filter that adaptively learns, then quickly adjusts itself for each major alteration of target trajectory.

1.3 Incorporation of Singer Process into the Target Dynamics

In incorporating the correlated process, the linearized spherical model of [5] is preserved. To this end, consider a target whose motion in rectangular coordinates is described by

$$\begin{aligned}\ddot{x} &= -\alpha \dot{x} + u_x + w'_x \\ \dot{w}'_x &= -aw'_x + w_x\end{aligned}\tag{1.3.1}$$

where

α is a drag coefficient

u_x is the deterministic input in the x direction randomly chosen from a set of N possible inputs.

w'_x is the Singer correlated acceleration process acting in the x direction with a time constant $\tau_c = 1/\alpha$. This process used throughout the report is shown modeled in Figure 1.3.

w_x is a white Gaussian random process acting in the x direction

A similar set of equations exists for the y and z directions.

Defining

$$\dot{x}_1 = x$$

$$\dot{x}_2 = \dot{x}$$

$$x_3 = w_x'$$

the following continuous time state variable model is obtained for

Equation (1.3.1)

$$\begin{bmatrix} \dot{x}_1 \\ \dot{x}_2 \\ \dot{x}_3 \end{bmatrix} = \begin{bmatrix} 0 & 1 & 0 \\ 0 & -\alpha & 1 \\ 0 & 0 & -\alpha \end{bmatrix} \begin{bmatrix} x_1 \\ x_2 \\ x_3 \end{bmatrix} + \begin{bmatrix} 0 \\ 1 \\ 0 \end{bmatrix} u_x + \begin{bmatrix} 0 \\ 0 \\ 1 \end{bmatrix} w_x \quad (1.3.2)$$

Discretizing (1.3.2) in time yields

$$\begin{bmatrix} x_1 \\ x_2 \\ x_3 \end{bmatrix}_{k+1} = \begin{bmatrix} 1 & A & B \\ 0 & E & F \\ 0 & 0 & e^{-\alpha T} \end{bmatrix} \begin{bmatrix} x_1 \\ x_2 \\ x_3 \end{bmatrix}_k + \begin{bmatrix} C \\ A \\ 0 \end{bmatrix} u_{x_k} + \begin{bmatrix} D \\ G \\ J \end{bmatrix} w_{x_k} \quad (1.3.3)$$

where

$$A = (1 - e^{-\alpha T})/\alpha$$

$$B = [1 + (ae^{-\alpha T} - \alpha e^{-\alpha T}) / (\alpha - a)] / (\alpha a)$$

$$C = (\alpha T - 1 + e^{-\alpha T})/\alpha^2$$

$$D = [T + (aA - \alpha J)/(\alpha - a)]/(\alpha a)$$

$$E = e^{-\alpha T}$$

$$F = (e^{-\alpha T} - e^{-\alpha T})/(\alpha - a)$$

$$G = (J - A)/a - a$$

$$J = (1 - e^{-aT})/a$$

A similar state variable model is assumed to exist for the y and z directions.

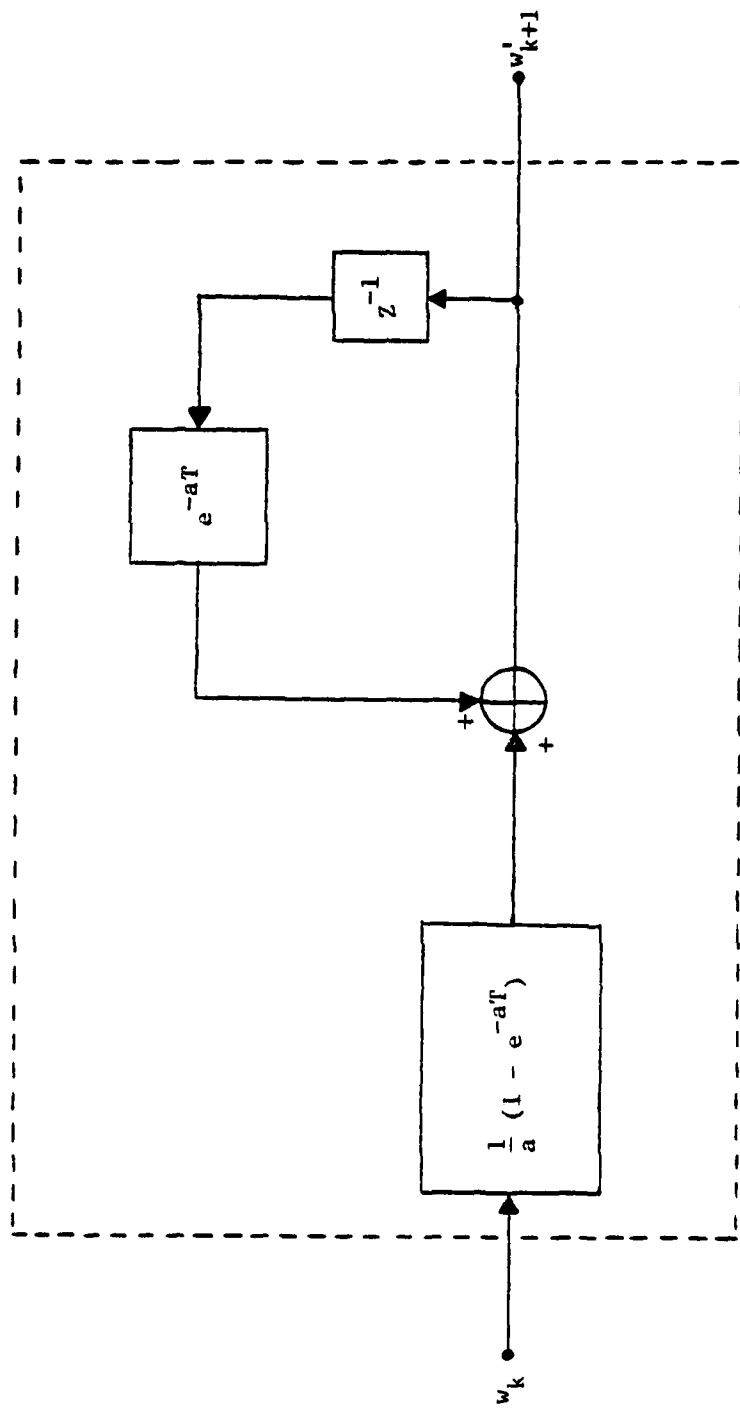


Figure 1.3 Generation of a Correlated Gaussian Random Process w' by Filtering
the White Gaussian Random Process w

Chapter 2

UNDERWATER PASSIVE TRACKING. INTRODUCTION AND LINEARIZED POLAR MODEL FOR THE MANEUVERING OBSERVER-SOURCE SCENARIO

2.1 Introduction

The tracking of air targets such as described in [7] is characterized by high quality radar data providing good system observability and high signal-to-noise ratio. In underwater passive submarine tracking on the other hand, the situation is characterized by meager data which, when it is available, is almost always a nonlinear function of the system state variables.

The particular problem which is addressed in this chapter and in the remainder of this report is how to track the target submarine (Source) from the moving Observer submarine *using sonar signals emanating from the Source*. Because the Observer does not use an active sonar but rather listens to sound waves emanating from the Source, this method of tracking has acquired the name *passive tracking*.

It is pointed out in [7] in conjunction with air targets that in order to successfully track a maneuvering target in three dimensions the dynamics must be realistically modeled in the chosen coordinate system and secondly that an adaptive feature must be designed to prevent filter divergence as the target executes evasive maneuvers. These two requirements are of equal importance in the underwater passive tracking domain.

The availability of air target radar data in spherical coordinates suggests that coordinate system as being the "natural" one in which to design a tracking filter. In the underwater case, the selection of a "natural" coordinate system based on the available data is a much more obscure process. This is true because almost all the available data are nonlinear functions of the state variables regardless of any coordinate system chosen. It is a major goal of this report to address this problem in detail. It will be shown that for a certain subset of the observables, a "natural" coordinate system does indeed exist. This discovery will then be exploited to design a "pseudo-linear" filter to process this subset of the observables using only linear filtering techniques.

2.2 State of the Art

The problem of passively tracking underwater targets has received very little attention in the literature. What little exposure has occurred has tended to concentrate on the bearings-only approach. In this method the Observer monitors his bearing to the Source, over a period of time. Usually the Observer must execute a known maneuver to remove the ambiguity that sometimes exists with this type of tracking algorithm.

In a very interesting paper, Hassab [8] passively tracks the maneuvering Source in three dimensions by exploiting the combination of bearing measurements and sonar time delays between the direct, bottom reflected and surface reflected sound waves emitted by a Source. Since

these time delays and bearing measurements are nonlinear functions of the state variables in the rectangular coordinate system used. The Extended Kalman Filter is employed to provide optimal estimates of the Source range, bearing, velocity and depth with respect to the moving Observer. The state vector consists of three rectangular position components (R_x , R_y , R_z) and three rectangular velocity components (v_x , v_y , v_z). A constant velocity model is used for the Source dynamics with an additive white Gaussian noise perturbation. Because of the choice of a rectangular coordinate system, the processing of the bearing measurements becomes coupled to the processing of the time delay measurements resulting in a 3×6 linearized measurement matrix having the following generic form:

$$H(k+1) = \begin{bmatrix} \frac{\partial \theta}{\partial R_x} & 0 & \frac{\partial \theta}{\partial R_y} & 0 & 0 & 0 \\ \frac{\partial \tau_1}{\partial R_x} & 0 & \frac{\partial \tau_1}{\partial R_y} & 0 & \frac{\partial \tau_1}{\partial R_z} & 0 \\ \frac{\partial \tau_2}{\partial R_x} & 0 & \frac{\partial \tau_2}{\partial R_y} & 0 & \frac{\partial \tau_2}{\partial R_z} & 0 \end{bmatrix} \quad (2.2.1)$$

where θ , τ_1 , τ_2 are the bearing and two sonar time delays, respectively.

In [9] a relative rectangular coordinate system is again chosen to model the Observer-Source scenario. The measurements used here are bearing and direct/surface reflected sonar time delays. Since these make the system unobservable, the Source is assumed to be at the same depth as the Observer. Again, the measurements are nonlinear

functions of the state variables with coupling occurring between the processing of bearing and time delay measurements.

One of the factors which makes rectangular coordinates appear so attractive for passive tracking is that compensation for Observer motion in this coordinate system is relatively simple, involving only a linear subtraction. For example, if

v_{x_s} = x component of Source velocity with respect to the ocean floor

v_{x_o} = x component of Observer velocity with respect to the ocean floor

R_x = relative distance between the x coordinates of the Source and Observer

then, assuming a constant velocity model for the Source [8]

$$\begin{bmatrix} R_x(k+1) \\ v_{x_s}(k+1) \end{bmatrix} = \begin{bmatrix} 1 & T \\ 0 & 1 \end{bmatrix} \begin{bmatrix} R_x(k) \\ v_{x_s}(k) \end{bmatrix} - \begin{bmatrix} T \\ 0 \end{bmatrix} v_{x_o}(k) \quad (2.2.2)$$

Thus rectangular coordinates offer a very convenient method of compensation for Observer motion.

However, rectangular coordinates are a very poor coordinate system in which to filter when one considers the types of measurement data other than sonar time delays available for passive tracking. For example, Source bearing with respect to the Observer is one of the most consistently available measurements. Another commonly available measurement data consists of Source line frequency spectra which are emitted from various mechanical elements aboard the Source.

In filtering in relative rectangular coordinates (x, y, z) these types of measurement data are inherently nonlinear functions of

the Source state variables. For example, bearing involves the arc tangent function of Source x and y relative coordinates. The line frequency spectra, when used in Doppler tracking with an unknown center frequency f_0 , involve the product of state variables and again a nonlinear estimation problem must be solved.

In an attempt to find a more suitable coordinate system for passive tracking, Tenney et al. [10] propose a relative coordinate system based on the closest point of approach (CPA) for use with Doppler tracking. This approach requires that

1. the measurement matrix be relinearized at each iteration;
2. the Source trajectory be of the "crossing" variety to produce a closest point of approach;
3. the center frequency of the transmitted signal be known and constant.

The presence of bearing observations suggests either polar or spherical coordinates as a more suitable system in which to filter. This is true in light of earlier work where a linearized spherical filter was used to process spherical measurement data using linear filtering theory while permitting decoupling of each coordinate direction. Thus, for example, the bearing measurements available to the Observer could be decoupled from the time delay measurements and processed independently in either of these two coordinate systems. While the sonar time delay measurements would continue to be coupled together and necessitate a nonlinear filter such as the Extended Kalman filter, the decoupling of the bearing tracker from the time delays would represent a significant reduction in the complexity of the nonlinear filter. For example, if filtering in polar coordinates is undertaken, then because of the decoupling of the bearing channel the time delay processing

would involve linearizing the measurement matrix about only two state variables rather than about three state variables as in Equation (1.2.1).

To distinguish between the merits of spherical and polar coordinates, consider Figure 2.3.1. Assume that both the Observer and Source depths remain unchanged; therefore $\dot{z}_{so} = 0$. If the Source radial rate $\dot{\rho}$ is non-zero then in spherical coordinates the elevation rate $\dot{\epsilon}$ is also non-zero, even if $\dot{\rho}$ is some fixed value. In polar coordinates, on the other hand, and with these same conditions, the Source vertical rate \dot{z}_{so} is, of course, zero. The implications of all this are that in spherical coordinates the generally non-zero elevation rate requires a sophisticated modeling technique for the Source input acting in the elevation direction. This technique would involve several overlapping Gaussian curves and also an adaptive technique to provide a weighted sum. It will be shown in Chapter 3 that with polar coordinates, on the other hand, the source Z direction input can be modeled in a particularly simple manner using only a single Gaussian curve having a mean value equal to zero.

It will also be shown later that polar coordinates possess extremely attractive features for passive tracking using the Doppler effect. For these reasons it is decided to undertake passive tracking of a moving Source from a moving Observer in the polar coordinate system.

Of course, while polar coordinates offer the advantages outlined above, there is a concomitant penalty in that compensation for Observer motion in this coordinate system is more difficult and complex than for the rectangular case. To appreciate this point, consider the

state model given by Equation (2.2.2). If one imagines a rectangular coordinate system attached to and moving with the Observer, then the state model (2.2.2) provides estimates of the target state variables with respect to this moving coordinate system. However, regardless of the maneuvers executed by the Source and Observer, this coordinate system always translates parallel to itself.

Referring to Figure 2.3.1, consider a polar coordinate system attached to and moving with the Observer. As the Observer and Source maneuver with respect to each other the direction of the polar radius vector ρ connecting the Observer to the Source changes its direction in keeping with the changing relative positions. Therefore the polar coordinate system attached to the Observer rotates in addition to translating and it is the added complexity caused by this rotation that renders more difficult the task of formulating a state variable model in polar coordinates which accurately compensates for Observer motion.

It is this problem which is solved in the next section.

2.3 Linearized Polar Model for the Dynamics of the Maneuvering Observer-Source Scenario

Consider Figure 2.3.1 which shows the geometry of the Observer-Source scenario in polar coordinates. In this figure, the plane defined by the X-Y axes is parallel to the ocean bed and fixed with respect thereto. The horizontal distance separating the Source and Observer is labeled ρ and will be referred to in the future simply as the radius. This polar radius is to be distinguished from the spherical radius labeled r which is the distance separating the Observer and Source in three-dimensional space. The vertical distance z_{so} is simply the differences in their depths. Figure 2.3.2 is the projection of Figure 2.3.1 onto the X-Y plane. The parameters appearing in this figure are defined in Table 1.3.1.

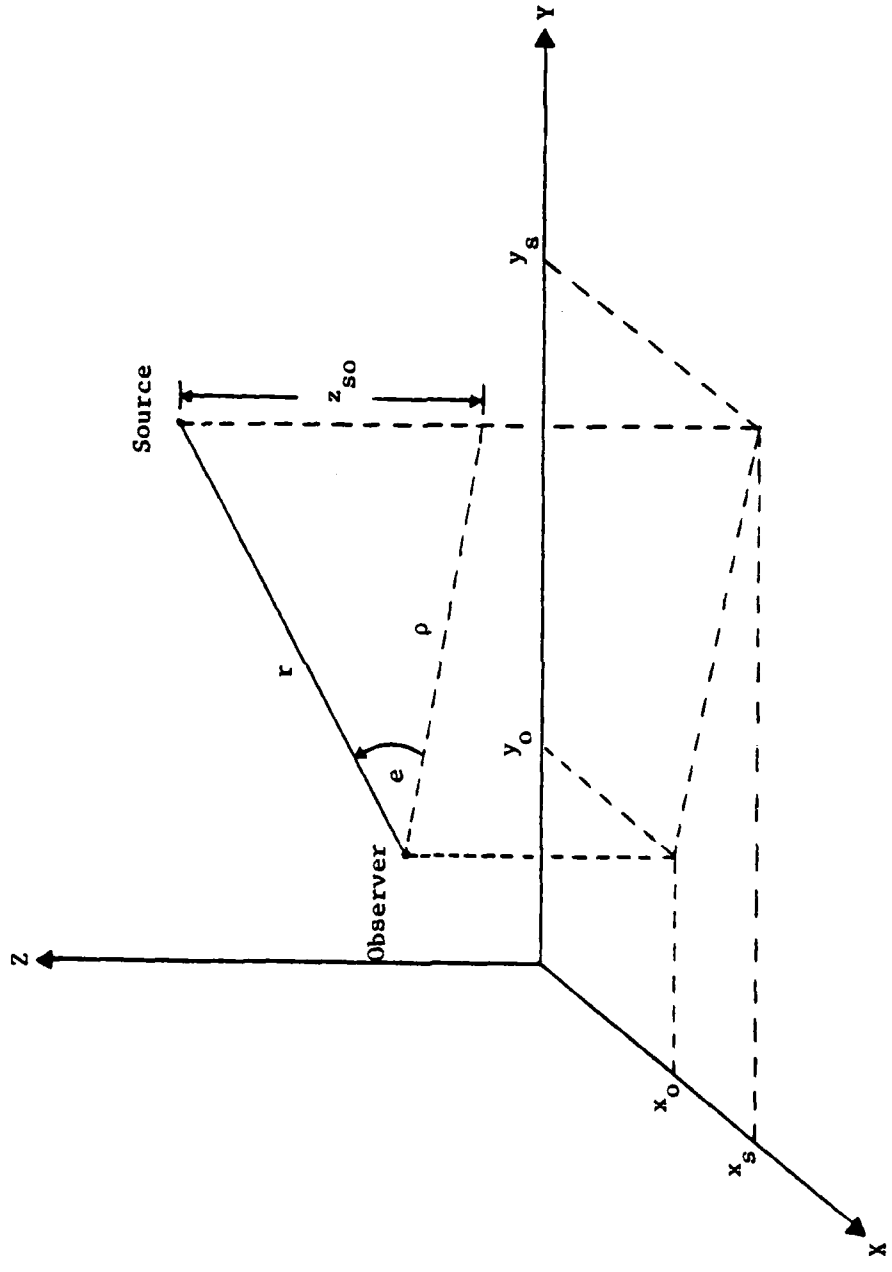


Figure 2.3.1 Geometry of the Observer-Source Scenario in Polar Coordinates

The linearized polar model is developed using a modified version of the approximate modeling technique of Reference (5) except that now, the origin of the coordinate system is moving.

o CHANNEL MODEL

σ_{k+1} calculation:

Referring to Figure 1.3.2

$$\begin{aligned} \sigma &= [(x_s - x_o)^2 + (y_s - y_o)^2]^{1/2} \\ \frac{\partial \sigma}{\partial x_s} &= \frac{(x_s - x_o)}{\sigma} & \frac{\partial \sigma}{\partial x_o} &= -\frac{(x_s - x_o)}{\sigma} \\ \frac{\partial \sigma}{\partial y_s} &= \frac{(y_s - y_o)}{\sigma} & \frac{\partial \sigma}{\partial y_o} &= -\frac{(y_s - y_o)}{\sigma} \end{aligned} \quad (2.3.1)$$

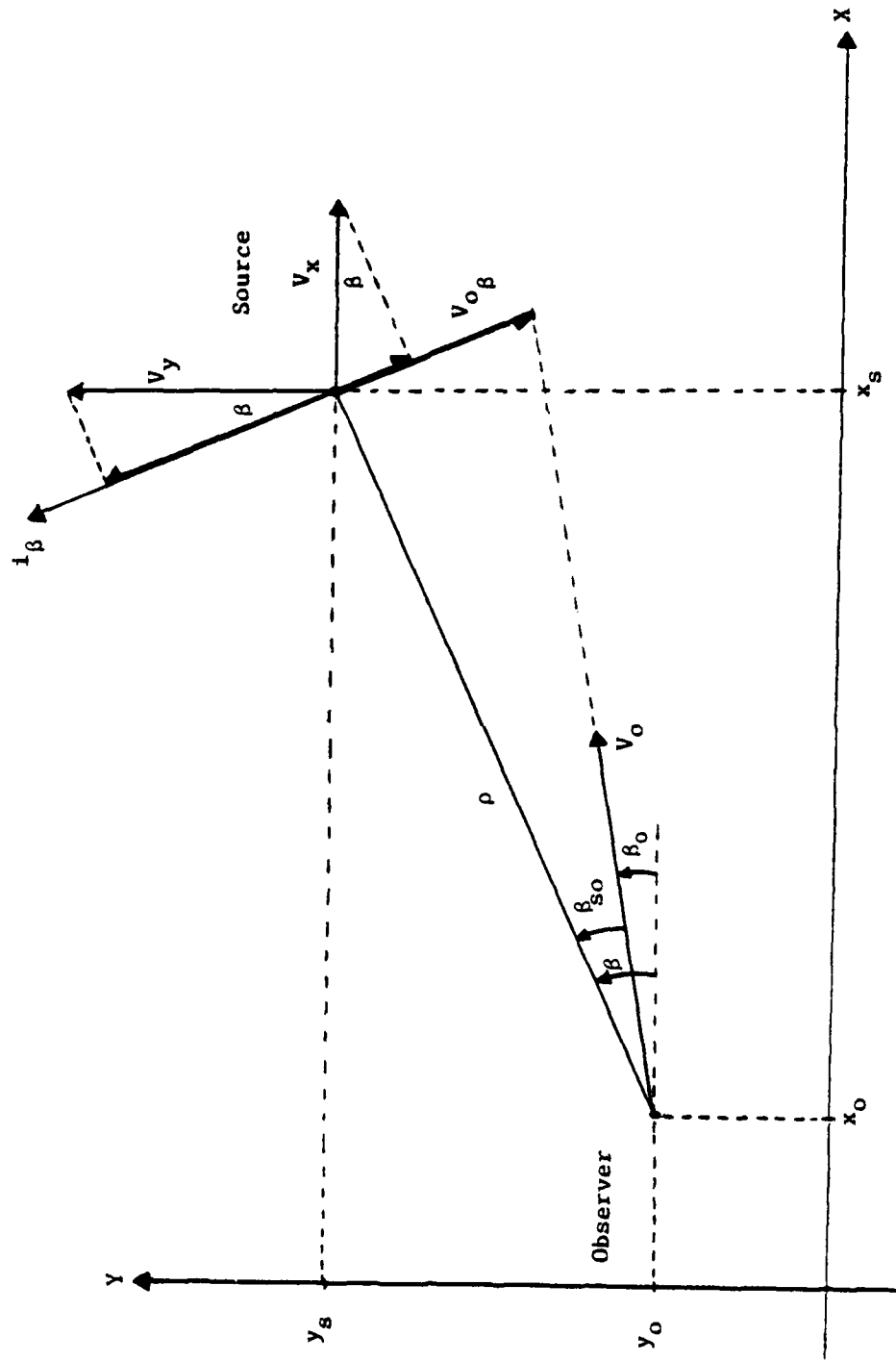


Figure 2.3.2 Geometry of the Observer-Source Scenario Projected Onto the X-Y Plane

Table 2.3.1
Explanation of Parameters Appearing in Figure 3.3.2

ρ	the polar radius
v_o	the velocity vector of the Observer
β	the angle between the polar radius ρ and the (fixed) X axis
β_o	angle between the X axis and the velocity vector of the Observer
β_{so}	the relative bearing of the Source with respect to the Observer
v_x	an x-directed vector, used for illustrative purposes
v_y	a y-directed vector, used for illustrative purposes
i_3	a unit vector in the direction of increasing angle β
$v_{o\beta}$	projection of the Observer velocity vector onto i_3
x_o, y_o, x_s, y_s	position coordinates of the Observer and Source, respectively, in the rectangular coordinate system

$$\dot{\rho} = \frac{(x_s - x_o)}{\rho} (\dot{x}_s - \dot{x}_o) + \frac{(y_s - y_o)}{\rho} (\dot{y}_s - \dot{y}_o) \quad (2.3.2)$$

ρ_{k+1} is expanded as follows keeping only the linear terms:

$$\begin{aligned} \rho_{k+1} &= \rho_k + \frac{\partial \rho}{\partial x_s} \Big|_k (x_{s_{k+1}} - x_{s_k}) + \frac{\partial \rho}{\partial y_s} \Big|_k (y_{s_{k+1}} - y_{s_k}) \\ &\quad + \frac{\partial \rho}{\partial x_o} \Big|_k (x_{o_{k+1}} - x_{o_k}) + \frac{\partial \rho}{\partial y_o} \Big|_k (y_{o_{k+1}} - y_{o_k}) \end{aligned} \quad (2.3.3)$$

Assuming a linear drag model for the Source as given in (1.3.1), upon substituting (2.3.1) into (2.3.3) for the Source connected terms, and we get

$$\begin{aligned} (x_{k+1} - x_k) &= Ax_k + Bw'_x + Cu_x x_k \\ \rho_{k+1} &= \rho_k + \frac{(x_s - x_o)}{\rho} \Big|_k [Ax_s + Bw'_{s_x} + Cu_{s_x} + Dw_{s_x}] \Big|_k \\ &\quad + \frac{(y_s - y_o)}{\rho} \Big|_k [Ay_s + Bw'_{s_y} + Cu_{s_y} + Dw_{s_y}] \Big|_k \\ &\quad - \frac{(x_s - x_o)}{\rho} \Big|_k [x_{o_{k+1}} - x_{o_k}] - \frac{(y_s - y_o)}{\rho} \Big|_k [y_{o_{k+1}} - y_{o_k}] \end{aligned} \quad (2.3.4)$$

In the above equation and in all subsequent analysis, subscripts s and o refer to the Source and the Observer, respectively.

Now

$$(x_{o_{k+1}} - x_{o_k}) = \dot{x}_{o_k}^T \quad \text{and} \quad (2.3.5)$$

$$(y_{o_{k+1}} - y_{o_k}) = \dot{y}_{o_k}^T$$

Combining terms with like coefficients in (2.3.4) and making use of (2.3.5),

$$\begin{aligned}
\phi_{k+1} = \phi_k + A & \left[\frac{(x_s - x_o)}{\rho} \dot{x}_s + \frac{(y_s - y_o)}{\rho} \dot{y}_s \right] \Big|_k \\
& + B \left[\frac{(x_s - x_o)}{\rho} w'_{s_x} + \frac{(y_s - y_o)}{\rho} w'_{s_y} \right] \Big|_k \\
& + C \left[\frac{(x_s - x_o)}{\rho} u_{s_x} + \frac{(y_s - y_o)}{\rho} u_{s_y} \right] \Big|_k \\
& + D \left[\frac{(x_s - x_o)}{\rho} w_{s_x} + \frac{(y_s - y_o)}{\rho} w_{s_y} \right] \Big|_k \\
& - T \left[\frac{(x_s - x_o)}{\rho} \dot{x}_o + \frac{(y_s - y_o)}{\rho} \dot{y}_o \right] \Big|_k
\end{aligned} \tag{2.3.6}$$

Consider the coefficient of B appearing in Equation (2.3.6). From Figure 2.3.2, $\frac{(x_s - x_o)}{\rho}$ and $\frac{(y_s - y_o)}{\rho}$ are the direction cosines between the X and Y axes, respectively, and the ϕ direction. Hence

$$\frac{(x_s - x_o)}{\rho} w'_{s_x} + \frac{(y_s - y_o)}{\rho} w'_{s_y} \equiv w'_{s_\phi} \tag{2.3.7}$$

is the sum of the projections of w'_{s_x} and w'_{s_y} onto the ϕ direction. This sum acting in the ϕ direction can be replaced by a single equivalent term denoted by w'_{s_ϕ} . In a similar manner the coefficients of C and D are called u_{s_ϕ} and w_{s_ϕ} , respectively. The coefficient of A in (2.3.6) represents the projection of the Source velocity onto the radial direction. This coefficient must be recast in a different formulation in order to complete the state model of (2.3.6). To this end Equation (2.3.2) is rewritten as follows:

$$\frac{(x_s - x_o)}{\rho} \dot{x}_s + \frac{(y_s - y_o)}{\rho} \dot{y}_s = \dot{\rho} + \frac{(x_s - x_o)}{\rho} \dot{x}_o + \frac{(y_s - y_o)}{\rho} \dot{y}_o \quad (2.3.8)$$

using $\frac{(x_s - x_o)}{\rho} \dot{x}_o + \frac{(y_s - y_o)}{\rho} \dot{y}_o \equiv v_o \cos \beta_{so}$ (2.3.9)

using 2.3.8 and 2.3.9 yields

$$\frac{(x_s - x_o)}{\rho} \dot{x}_s + \frac{(y_s - y_o)}{\rho} \dot{y}_s = \dot{\rho} + v_o \cos \beta_{so} \quad (2.3.10)$$

Substituting Equations (2.3.9) and (2.3.10) for the coefficients of T and A, respectively, in (2.3.6) and collecting like terms results in the following state variable model:

$$p_{k+1} = p_k + A\dot{p}_k + Bw'_{s\rho_k} + Cu_{s\rho_k} + Dw_{s\rho_k} + (A-T)(v_o \cos \beta_{so})^T_k \quad (2.3.11)$$

A similar approach is taken to develop a state model for \dot{p}_{k+1} . By assuming that the Observer maintains a constant velocity for long periods of time, and that $w'_{s\rho}$ is a zero mean correlated GAUSSIAN random process acting in the ρ direction the following state equations are easily obtained.

$$\begin{bmatrix} p \\ \dot{p} \\ w'_{s\rho} \\ \dot{w}'_{s\rho} \end{bmatrix}_{k+1} = \begin{bmatrix} 1 & A & B \\ 0 & E & F \\ 0 & 0 & e^{-aT} \end{bmatrix} \begin{bmatrix} p \\ \dot{p} \\ w'_{s\rho} \end{bmatrix}_k + \begin{bmatrix} C & (A-T) \\ A & (E-1) \\ 0 & 0 \end{bmatrix} \begin{bmatrix} u_{s\rho} \\ v_o \cos \beta_{so} \end{bmatrix}_k + \begin{bmatrix} D \\ G \\ J \end{bmatrix} w_{s\rho_k} \quad (2.3.12)$$

The underlying constraint for the state model (2.3.12) requires that the Observer adopt a constant velocity profile.

Z Channel

Using a discretized version of the basic linearized drag model of chapter 1, and letting z_{so} be the relative separation between Source and Observer the following state model is presented.

$$\begin{bmatrix} z_{so} \\ \dot{z}_{so} \\ w'_{sz} \end{bmatrix}_{k+1} = \begin{bmatrix} 1 & A & B \\ 0 & E & F \\ 0 & 0 & e^{-aT} \end{bmatrix} \begin{bmatrix} z_{so} \\ \dot{z}_{so} \\ w'_{sz} \end{bmatrix}_k + \begin{bmatrix} C & (A-I) \\ A & (E-1) \\ 0 & 0 \end{bmatrix} \begin{bmatrix} u_{sz} \\ \dot{z}_o \\ w_{sz} \end{bmatrix}_k + \begin{bmatrix} D \\ G \\ J \end{bmatrix} w_{sz}_k$$

(2.3.13)

The state model is also subject to the constraint of a constant velocity Observer.

It is interesting to observe that both state models (2.3.12) and (2.3.13) are identical although the types of manipulations involved in the derivations are quite different. For example, a Taylor series expansion is used to derive (2.3.12) whereas no such expansion is used in deriving (2.3.13).

Bearing Channel

From a similar development the resultant state equations are presented.

$$\begin{bmatrix} \dot{\beta}_{so} \\ \dot{\beta}_{so} \\ w'_{s_B} \end{bmatrix}_{k+1} = \begin{bmatrix} 1 & A & (B/\rho_k) \\ 0 & E & (F/\rho_k) \\ 0 & 0 & e^{-aT} \end{bmatrix} \begin{bmatrix} \dot{\beta}_{so} \\ \dot{\beta}_{so} \\ w'_{s_B} \end{bmatrix}_k + \begin{bmatrix} (C/\rho_k) & (A-T) \\ (A/\rho_k) & (E-1) \\ 0 & 0 \end{bmatrix} \begin{bmatrix} u_{s_B} \\ (\dot{\beta}_o - \frac{v_o \sin \beta_{so}}{\rho}) \end{bmatrix}_k \\
 + \begin{bmatrix} (D/\rho_k) \\ (G/\rho_k) \\ J \end{bmatrix} w'_{s_B} \quad (2.3.14)$$

This state model is subject to the constraint that

$$\dot{\beta}_{o_{k+1}} = \dot{\beta}_{o_k}$$

This completes the derivation of the linearized polar model in relative coordinates for the moving Observer-Source scenario. In the next chapter this model will be applied to passively track a maneuvering Source using sonar time delays.

2.4 Conclusion

Before closing, a comment needs to be made concerning the constraints which the preceding state variable models place on the Observer motion. While the state variable models are only valid for a non-maneuvering, i.e. constant velocity Observer, this does not mean that the Observer cannot execute any maneuvers. What is implied is that during the maneuver the state models are inaccurate and will not yield good estimates. Upon completion of the Observer maneuver, the model is

once again valid and will yield good estimates. Of course, during a maneuver transients are introduced and consequently any filter would inevitably yield poor estimates during this period.

Chapter 3

PASSIVE TRACKING USING SONAR TIME DELAYS. THE ADAPTIVE EXTENDED POLAR KALMAN FILTER.

3.1 Introduction

In this chapter the linear polar model which was developed in Chapter 2 will be employed to passively track a maneuvering Source using sonar time delays. Figure 3.1.1, which uses notation similar to that in Hassab [8], gives the two-dimensional geometry showing the paths traversed by the Source-emitted sonar signals in question. The "direct" signal traverses the path labeled r . The "surface reflected" signal traverses the path labeled $R_{2s} - R_{1s}$ and τ_1 is the difference in time of arrival between this signal and the "direct" signal, as measured at the Observer. The "bottom reflected" signal traverses the path labeled $R_{2b} - R_{1b}$, and τ_2 is the difference in time of arrival between this signal and the direct signal, as measured at the Observer.

From Hassab's work [8] the equations, which are repeated below for convenience, show that τ_1 and τ_2 are nonlinear functions of the system state variables ρ and z_{so} as given in Figure 3.1.1.

$$\tau_1 = [(\rho^2 + z_{so}^2 + 4H_{01}^2 - 4H_{01} z_{so})^{1/2} - (\rho^2 + z_{so}^2)^{1/2}] / c \quad (3.1.1)$$

$$\tau_2 = [(\rho^2 + z_{so}^2 + 4H_{02}^2 + 4H_{02} z_{so})^{1/2} - (\rho^2 + z_{so}^2)^{1/2}] / c \quad (3.1.2)$$

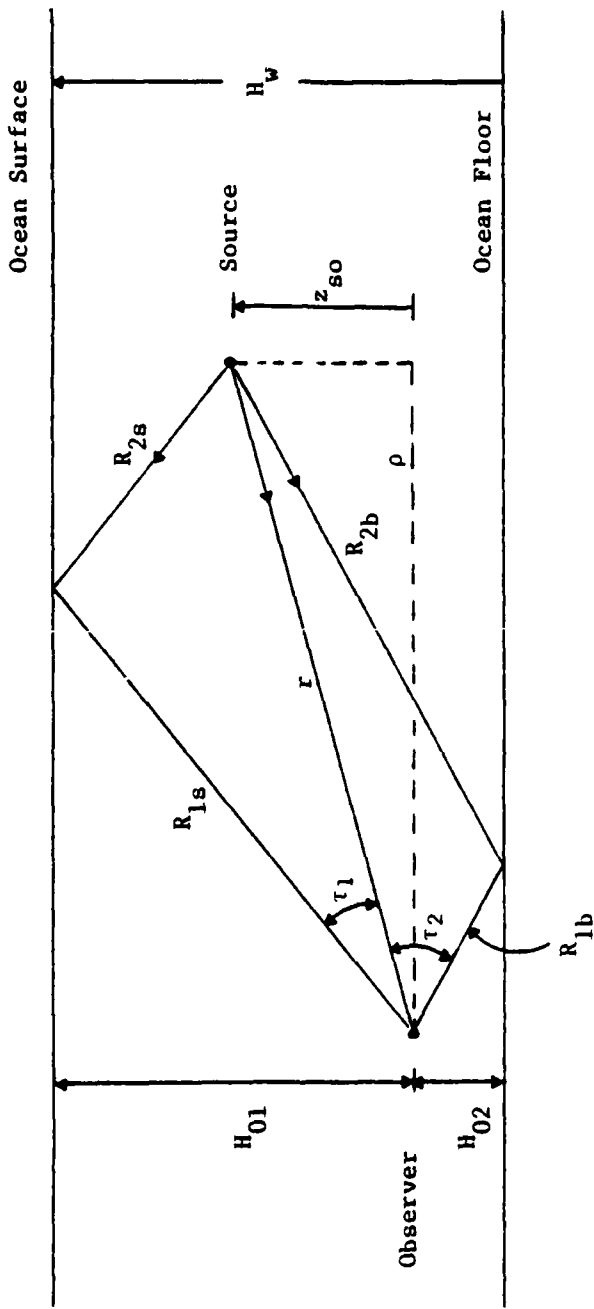


Figure 3.1.1 Paths Traversed by the Source-Emitted Sonar Signals in Reaching the Observer

Therefore the Extended Kalman Filter must be employed to provide optimal estimates in the presence of these nonlinear measurements.

The "adaptive filter approach developed in [5] was earlier applied with much success to tracking maneuvering air targets. This approach will now be applied in the underwater environment to passively track a maneuvering Source from a moving Observer using the measurements (3.1.1) and (3.1.2). Because of the coupling in (3.1.1) and (3.1.2) between the ρ and z_{so} state variables, the ρ and z channels cannot be filtered independently. Rather the two models developed separately in Chapter 2 must be combined in the manner described in Section 3.2.

A modified version of the conventional Extended Kalman Filter algorithm must be developed in order to accommodate nonlinear filtering using the adaptive filter approach. This will also be described in the next section.

3.2 Combined ρ/z Channel Filtering of Sonar Time Delays Using the Augmented Extended Polar Kalman Filter

Consider the following combined ρ/z state vector:

$$[\rho \quad \dot{\rho} \quad w'_{s\rho} \quad z \quad \dot{z} \quad w'_{sz}]^T$$

where the subscript so on z_{so} has been dropped for notational convenience. The linearized state variable model corresponding to this state vector is given in Equation (3.2.1). Defining

$$x_{k+1}^{(i)} = \phi x_k^{(i)} + \Gamma u_k^{(i)} + \psi w_k$$

where:

$$\begin{bmatrix} \dot{\rho} \\ \ddot{\rho} \\ \vdots \\ \dot{w_s}_\rho \\ \ddot{w_s}_\rho \\ \vdots \\ \dot{w_s}_z \\ \ddot{w_s}_z \end{bmatrix}_{k+1}^{(1)} = \begin{bmatrix} 1 & A & B & 0 & 0 & 0 \\ 0 & E & F & 0 & 0 & 0 \\ 0 & 0 & e^{-aT} & 0 & 0 & 0 \\ 0 & 0 & 0 & 1 & A & B \\ 0 & 0 & 0 & 0 & E & F \\ 0 & 0 & 0 & 0 & 0 & e^{-aT} \end{bmatrix} + \begin{bmatrix} \dot{\rho} \\ \ddot{\rho} \\ \vdots \\ \dot{w_s}_\rho \\ \ddot{w_s}_\rho \\ \vdots \\ \dot{w_s}_z \\ \ddot{w_s}_z \end{bmatrix}_k^{(1)}$$

$$(3.2.1)$$

$$\begin{bmatrix} C & (A-T) & 0 & 0 & 0 \\ A & (E-1) & 0 & 0 & 0 \\ 0 & 0 & 0 & 0 & 0 \\ 0 & 0 & 0 & C & (A-T) \\ 0 & 0 & 0 & A & (E-1) \\ 0 & 0 & 0 & 0 & 0 \end{bmatrix} + \begin{bmatrix} u_{s_\rho}^{(1)} \\ v_o \cos \beta_{so} \\ u_{s_z}^{(1)} \\ z_0 \\ z_0 \\ 0 \end{bmatrix} + \begin{bmatrix} p & 0 \\ g & 0 \\ j & 0 \\ 0 & D \\ 0 & G \\ 0 & J \end{bmatrix}$$

Consider the deterministic input vector (3.2.1). The first entry, namely $u_{s_p}^{(i)}$, refers to the mean value of the i th Gaussian curve in the series of N partially overlapping Gaussian curves now being used to model the Source p channel input. Likewise the superscript i on $u_{s_z}^{(i)}$ in (3.2.1) refers to the i th Gaussian curve which is being used to model the Source z channel input. The last entry, namely \dot{z}_o , is the (known) Observer velocity in the Z direction or vertical direction.

In general, the Source does not execute many maneuvers in the Z direction. Whenever such a maneuver does take place it lasts only for a brief period. This is true because the Source can move upward only as far as the ocean surface and downward to its maximum permissible depth, which is usually a relatively small distance compared to the ocean depth. Therefore the Source is quite constrained in its movement along the Z direction in Figure 3.1.1. The conclusion to be drawn from this is that the Source input u_{s_z} is generally zero with there being only brief periods of time when it is non-zero. Therefore in modeling the Source input in the Z direction, only one time correlated Gaussian curve with a mean value of zero is needed. However, since the measurements are nonlinear functions of the state variables the extended Kalamon filter is used.

3.3 Summary of the Extended Kalman Filter

The Extended Kalman filter is usually the first filter to be used when confronted with either system or measurement nonlinearities, or both. This filter is well documented [11] and is summarized in (3.2.2) - (3.2.7) for a linear system with nonlinear measurements.

$$\begin{aligned} P(k+1|k+1) &= [I - K\{\hat{X}(k+1|k)\}H\{\hat{X}(k+1|k)\}]P(k+1|k) \\ &\quad \times [I - K\{\hat{X}(k+1|k)\}H\{\hat{X}(k+1|k)\}]^T \\ &\quad + K\{\hat{X}(k+1|k)\}R(k+1)K\{\hat{X}(k+1|k)\}^T \end{aligned} \quad (3.2.2)$$

$$\begin{aligned} K\{\hat{X}(k+1|k)\} &= P(k+1|k)H^T\{\hat{X}(k+1|k)\}[H\{\hat{X}(k+1|k)\}P(k+1|k)H\{\hat{X}(k+1|k)\}]^T \\ &\quad + R(k+1)]^{-1} \end{aligned} \quad (3.2.3)$$

$$P(k+1|k) = \Phi P(k|k)\Phi^T + \Psi Q(k)\Psi^T + \Gamma Q u \Gamma^T \quad (3.2.4)$$

$$\hat{X}(k+1|k+1) = \hat{X}(k+1|k) + K\{\hat{X}(k+1|k)\}[z(k+1) - h\{\hat{X}(k+1|k)\}] \quad (3.2.5)$$

$$\hat{X}(k+1|k) = \Phi \hat{X}(k|k) + \Gamma u(k) \quad (3.2.6)$$

$$H\{\hat{X}(k+1|k)\} \equiv \left[\frac{\partial h_i(X)}{\partial x_j} \right] \Big|_{\hat{X}(k+1|k)} \quad (3.2.7)$$

Several comments need to be made concerning the above algorithm:

1. Equation (3.2.2) for the updated covariance involves more terms than are usually used, namely

$$P(k+1|k+1) = [I - K\{\hat{X}(k+1|k)\}H\{\hat{X}(k+1|k)\}]P(k+1|k) \quad (3.2.8)$$

The additional terms appearing in (3.2.2) which do not appear in (3.2.8) are necessary to guarantee that $P(k+1|k+1)$ is always symmetric. The loss of symmetry that may occur in using (3.2.8) in the Extended algorithm arises from the approximate nature of this filtering

algorithm, especially the approximate value for the Kalman Gain matrix which the algorithm is only capable of producing.

2. The Kalman Gain matrix is shown to be a function of the predicted estimate $\hat{X}(k+1|k)$ by explicitly including this term in its argument. This functional relationship arises from the presence in Equation (3.2.3) of the linearized measurement matrix $H\{\hat{X}(k+1|k)\}$. This linearized measurement matrix is defined by

$$H\{\hat{X}(k+1|k)\} \equiv [\frac{\partial h_i(X)}{\partial x_j}]|_{\hat{X}(k+1|k)}$$

3. The measurement residuals are formed by evaluating the *nonlinear* functional relationships in (3.2.5) using the predicted estimate.
4. The additional term PQu^T in (3.2.4) is used to account for the mismatch of $u(i)$ and the actual unknown u .

With the above comments complete, the adaptive Extended Kalman filter algorithm is now discussed.

3.4 The Adaptive Tracking Filter

The heart of the adaptive filter developed in this report is the forming of the estimate of the target states, in each channel, from a weighted sum of estimates conditioned on the N possible discrete input levels.

Consider the state model (3.2.1). This state model views the target input acting in the polar direction as being derived from a time correlated Gaussian density having a mean value u_p . Next consider a series of N such Gaussian curves with displaced mean values $u_p^{(i)}$, $i = 1, 2, \dots, N$ and partially overlapping "tails" as shown in

Figure 3.2.1. If a bank of N Kalman filters is formed, each filter based on the state equations of equation (3.2.1) with the deterministic

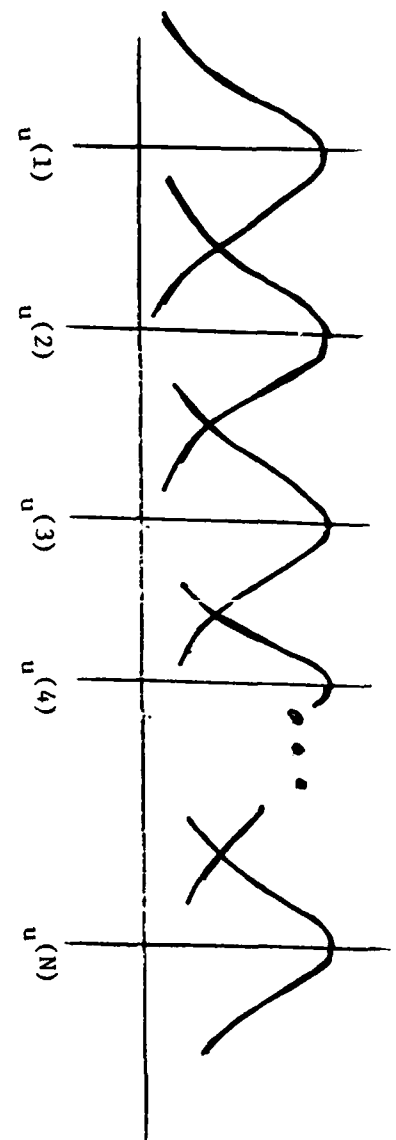


Figure 3.2.1 Series of N Partially Overlapping Gaussian Curves

input u_p being a different one of these N mean values, then a series of N estimates is obtained, each conditioned on a different Gaussian curve. Next a weighted sum of these estimates is obtained in a manner to be disclosed below, and this weighted sum is taken to be the unconditioned estimate of the target states.

Calculation of weighting coefficients: The general case

As previously discussed, the target input is now modeled as coming from a series of N overlapping Gaussian curves each of which has a predetermined mean value. As the target executes a series of evasive maneuvers in the polar channel, for example, the changing input to produce these maneuvers is viewed as randomly switching among these N curves. By applying the semi-Markov statistics to this switching process a series of N probabilities W_i , $i = 1, 2, \dots, N$ is generated [7] where

$$W_i \equiv \Pr \{ \text{target input is being derived from the Gaussian curve whose mean value is } u_p^{(i)} \}$$

These W_i are then used to form the weighted estimate.

We begin with the well-known relation that the optimal estimate can be written as a weighted sum of the input-conditioned estimates as shown in figure 3.2.2 [11]. Thus if $\hat{x}^{(i)}(k+1)$ represents the optimal estimate of $x(k+1)$ given that the i th input force $u^{(i)}$ is present (the i th-input force being one of the previously described mean values), then based on the data sequence

$$z(k+1) = \{z(1), z(2), \dots, z(k), z(k+1)\},$$

we define

$$\hat{x}(k+1) = \sum_{i=1}^N \hat{x}^{(i)}(k+1) W_i(k+1) \quad (3.2.9)$$

where

$$W_i(k+1) = \Pr \{u(k) = u^{(i)} | Z(k+1)\} \quad (3.2.10)$$

and

$$\hat{x}^{(i)}(k+1) = E\{x(k+1) | u(k) = u^{(i)}, Z(k+1)\}.$$

Equation (3.2.9) is a total probability expression developed from the basic relation that

$$\hat{x}(k+1) = E\{x(k+1) | Z(k+1)\}$$

is the optimal mean-squared estimate. It is well known that the optimal input-conditioned estimates are provided by suitably matched Kalman filters. In particular, for the i^{th} filter

$$\begin{aligned} \hat{x}^{(i)}(k+1) &= \Phi(k)\hat{x}^{(i)}(k) + \Gamma(k)u^{(i)} + K(k+1)[z(k+1) \\ &\quad - H\Phi(k)\hat{x}^{(i)}(k) - H\Gamma(k)u^{(i)}] \end{aligned}$$

where

$$K(k+1) = M(k+1) H^T [HM(k+1) H^T + R]^{-1},$$

$$M(k+1) = \Phi(k) P(k) \Phi^T(k) + \Psi(k) Q \Psi^T(k)$$

and

$$P(k+1) = [I - K(k+1)H] M(k+1).$$

The matrices Φ , Γ and Ψ are used to denote the respective coefficient matrices in (3.2.1).

The following is an outline of the analysis given in [5] to calculate the recursive weighting coefficients W_i , $i = 1, 2, \dots, N$. Defining $Z(k+1) = \{Z(k), z(k+1)\}$, apply Bayes Theorem to (3.2.10) and obtain

$$W_i(k+1) = \frac{\Pr \{u(k) = u^{(i)} | Z(k)\} p\{z(k+1) | u(k) = u^{(i)}, Z(k)\}}{p\{z(k+1) | Z(k)\}} \quad (3.2.11)$$

The denominator, which varies with time; is independent of i and is therefore common to each $W_i(k+1)$ as a normalizing constant. The first numerator factor is determined from the semi-Markov input process.

Expanding this factor in a total probability expression,

$$\Pr\{u(k) = u^{(i)} | Z(k)\} = \sum_{j=1}^N \Pr\{u(k) = u^{(i)} | u(k-1) = u^{(j)}, Z(k)\} W_j(k).$$

And since $Z(k)$ has no influence on the Markov state transitions,

$$\Pr\{u(k) = u^{(i)} | Z(k)\} = \sum_{j=1}^N \theta_{ji} W_j(k) \quad (3.2.12)$$

where the semi-Markov probability is

$$\theta_{ji} = \Pr\{u(k) = u^{(i)} | u(k-1) = u^{(j)}\}$$

Combining (3.2.11) and (3.2.12)

$$W_i(k+1) = C p\{z(k+1) | u(k) = u^{(i)}, Z(k)\} \sum_{j=1}^N \theta_{ji} W_j(k) \quad (3.2.13)$$

where C is a normalizing constant

is the desired recursive relation for W_i . The required density p is approximately normally distributed and has distribution

$$P\{z(k+1) | u(k) = u^{(i)}, Z(k)\} \sim N\{m_i(k+1), C_i(k+1)\}, \quad (3.2.14)$$

where

$$m_i(k+1) = H[\Phi(k) \hat{x}^{(i)}(k) + \Gamma(k) u^{(i)}(k)] \quad (3.2.15)$$

and

$$C_i(k+1) = [HM(k+1) H^T + R]$$

Consider the measurement density conditioned on the i th mean value as given in (3.2.14). This density has covariance given by (3.2.15). What characterizes the different target "states" is the set of N Gaussian curves used to model the switching input. However, the target dynamics remain the same for all the "states". Consequently, if the

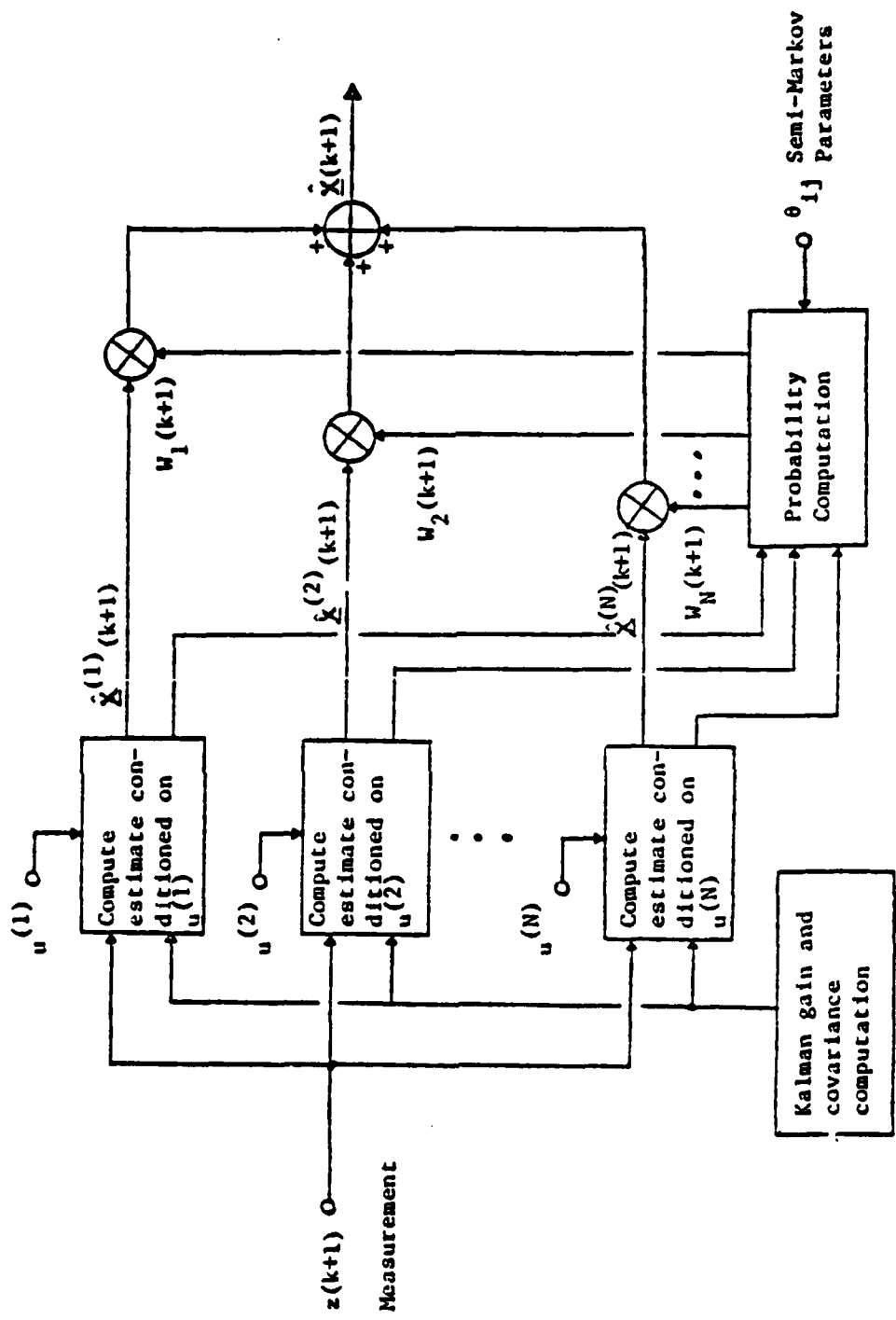


Figure 3.2.2 Typical Channel Block Diagram of the Adaptive Filter

process and measurement noise covariances $Q(k+1)$ and $R(k+1)$, respectively, are assumed to remain constant as the target switches from one "state" to another, then none of the quantities on the right is conditioned on i . Under these conditions, for a given value of $(k+1)$, $C_i(k+1)$ has the same value for all values of $i = 1, 2, \dots, n$. Indeed it is clear that for each value of $(k+1)$, the entire covariance analysis is identical for each filter in the previously mentioned filter "bank". Therefore, the bank of filters computationally is not much more than that of a single filter.

3.5 The Adaptive Extended Kalman Filter

In the one step ahead prediction by the adaptive filter, N predicted estimates $\hat{X}(k+1|k)^{(i)}$ are produced, each one conditioned on a different vector (3.2.9). In general, the weighted estimate

$$\hat{X}(k+1|k) \equiv \sum_{i=1}^N \hat{X}(k+1|k)^{(i)} W_i(k) \quad (3.3.1)$$

is closer to the true state vector than the individual conditioned estimates where the weights $W_i(k)$ are those which are computed at the end of the k th iteration. By computing the Gain matrix (3.2.3) using an H matrix linearized about (3.3.1) rather than N such Gain matrices linearized about the individual estimates $\hat{X}(k+1|k)^{(i)}$, a more accurate value is obtained. Since only one H matrix (and one Gain matrix) is now being used, the entire covariance analysis becomes the same for each mean value and a single filter suffices for this portion of the algorithm. This is how the conflicting requirements of the adaptive and Extended Kalman filter algorithms are reconciled. In summary, Equations (3.2.2), (3.2.3), and (3.2.4) describe the covariance portion of the Extended Kalman filter provided linearization takes place about $\hat{X}(k+1|k)$ as defined by (3.3.1).

The state predict and state update equations are now given with reference to the nonlinear measurements.

$$\tau_1 = h_1(X)$$

$$\tau_2 = h_2(X)$$

where h_1, h_2 are defined in (3.1) and (3.2), respectively and,

$$\hat{X}(k+1|k)^{(i)} = \Phi\hat{X}(k|k)^{(i)} + \Gamma_u^{(i)}.$$

The i th filter conditional measurement residual is defined as

$$\hat{z}^{(i)}(k+1) \equiv \begin{bmatrix} \hat{z}_1^{(i)}(k+1) \\ \hat{z}_2^{(i)}(k+1) \end{bmatrix} \equiv \begin{bmatrix} z_{\tau_1}(k+1) - h_1(\hat{X}(k+1|k)^{(i)}) \\ z_{\tau_2}(k+1) - h_2(\hat{X}(k+1|k)^{(i)}) \end{bmatrix} \quad (3.3.2)$$

where

$z_{\tau_1}(k+1)$ and $z_{\tau_2}(k+1)$ are the noisy measurements of τ_1 and τ_2 , respectively, at time $(k+1)$. N such conditional measurement residuals are computed corresponding to the N column vectors given by (3.2.1).

Then the i th updated state estimate is computed as follows:

$$\hat{X}^{(i)}(k+1|k+1) = \hat{X}^{(i)}(k+1|k) = K\{\hat{X}(k+1|k)\}[\hat{z}^{(i)}(k+1)] \quad (3.3.3)$$

for each value of $i = 1, 2, \dots, N$.

In order to complete the adaptive Extended Kalman filter algorithm, the linearized H matrix is now developed. Referring to Equation (3.2.7), H has the form

$$H(k+1) = \begin{bmatrix} \frac{\partial \tau_1}{\partial \rho} & 0 & 0 & \frac{\partial \tau_1}{\partial z} & 0 & 0 \\ \frac{\partial \tau_2}{\partial \rho} & 0 & 0 & \frac{\partial \tau_2}{\partial z} & 0 & 0 \end{bmatrix} \quad (3.3.4)$$

$X(k+1|k)$

Note that z is the relative vertical separation, i.e. z_{so} in Figure 3.1.1. From (3.1) and (3.2) we get

$$\begin{aligned}\frac{\partial \tau_1}{\partial \rho} &= [\frac{1}{D_1} - \frac{1}{D_2}] (\frac{\rho}{C}) \\ \frac{\partial \tau_1}{\partial z} &= [\frac{(z - 2H_{01})}{D_1} - \frac{z}{D_2}] / C\end{aligned}\tag{3.3.5}$$

$$\begin{aligned}\frac{\partial \tau_2}{\partial \rho} &= [\frac{1}{D_3} - \frac{1}{D_2}] (\frac{\rho}{C}) \\ \frac{\partial \tau_2}{\partial z} &= [\frac{(z + 2H_{02})}{D_3} - \frac{z}{D_2}] / C\end{aligned}$$

where

$$\begin{aligned}D_1 &= (\rho^2 + z^2 + 4H_{01}^2 - 4H_{01}z)^{1/2} \\ D_2 &= (\rho^2 + z^2)^{1/2} \\ D_3 &= (\rho^2 + z^2 + 4H_{02}^2 + 4H_{02}z)^{1/2}\end{aligned}$$

Note that Equations (3.3.5) are evaluated using the one step ahead predicted states; implicit in this, too, is that the predicted values for H_{01} and H_{02} are also calculated and used in (3.3.5). Equations (3.2.2), (3.2.3), (3.2.4) and (3.3.1) - (3.3.3) constitute the adaptive Extended Kalman filter algorithm.

A weighted estimate of the updated conditional estimates is next formed using the weights given by (3.2.11). It should be pointed out that because the measurements now form a vector, namely

$$\underline{z}(k+1) = \begin{bmatrix} \tau_1(k+1) & + & v_1(k+1) \\ \tau_2(k+1) & + & v_2(k+1) \end{bmatrix}$$

where v_1 , v_2 are additive zero mean white Gaussian measurement noise, the multivariate Gaussian distribution must be used to compute the

above weights. This distribution has the mean value vector

$$\begin{bmatrix} \hat{h}_1(\hat{X}(k+1|k))^{(i)} \\ \hat{h}_2(\hat{X}(k+1|k))^{(i)} \end{bmatrix}$$

and covariance matrix

$$C(k+1) = [H\{\hat{X}(k+1|k)\}P(k+1|k)H\{\hat{X}(k+1|k)\}^T + R(k+1)]$$

This completes the discussion of the Adaptive Extended Kalman filtering algorithm. In the next section specific design values will be discussed and the resulting filter performance evaluated.

3.6 Specific Filter Designs and the Resulting Filter Performance Using Synthetic Data

The numerical values used for submarine velocities, depths, etc. in the remainder of this report should not be taken as being representative of actual values for modern submarines, but are used exclusively for reference purposes.

The parameter selection process concerns itself with the following parameter set

$$\{a, \sigma_c, N, V_{\max}, a, Q_u\}$$

where

a is the assumed drag coefficient

σ_c is the standard deviation of the correlated process

N is the number of levels (mean values)

V_{\max} is the assumed maximum possible speed of the target set to be tracked

$$a = 1/\tau_c$$

where τ_c is the correlation time constant of the correlated process, and $Q_u = E(u - u^{(i)})(+u - u^{(i)})^T$ is the mismatch term in the covariance calculation.

The set of parameter values is summarized below:

$$T = 10.0 \text{ secs}$$

$$a = 0.05$$

$$\sigma_{c_p} = 0.18$$

$$\sigma_{c_z} = 0.03$$

$$N = 7$$

$$V_{\max} = \pm 24 \text{ ft/sec}$$

$$a = 0.25$$

$$u_{s_p}^{(i)} : -1.2, -0.8, -0.4, 0.0, 0.4, 0.8, 1.2$$

$$u_{s_z}^{(i)} : 0.0, 0.0, 0.0, 0.0, 0.0, 0.0, 0.0$$

$$Q_u : \begin{bmatrix} 0.01 & 0 & 0 & 0 \\ 0 & 0.06 & 0 & 0 \\ 0 & 0 & 0 & 0 \\ 0 & 0 & 0 & 0 \end{bmatrix}$$

The following initial conditions are used:

$$H_{02} = 2000'$$

$$z_{so} = 400'$$

$$H_w = 6000'$$

With a water depth H_w of 6000', these initial conditions place the Observer and Source at depths (below the water surface) of 1000' and 600', respectively, with the Source 400' above the Observer. These depths are more realistic than those used before. Because of temperature gradients and a variety of other reasons, the velocity of sound in water is not a constant but varies with position. In an attempt to take this into account, the velocity is modeled as a Gaussian random process with a mean value $C = 4950$ (ft/sec). This is the modeling technique which is used in [8]. The above conditions, which provide for a much more realistic environment in which to test the filter, yield the following range of time delays:

$$\tau_1 : 26 \text{ m.sec.} - 11 \text{ m.sec.}$$

$$\tau_2 : 951 \text{ m.sec.} - 471 \text{ m.sec.}$$

With additive measurement noise of 5 m.sec. standard deviation, the SNR for the τ_1 measurements gets lower as time progresses due to the

decreasing value of τ_1 . This decrease in τ_1 (and to a lesser degree τ_2) is caused by the decrease in the difference between the lengths of the direct and surface reflected paths as the separation of Observer and Source increases. In addition, since these time delays are generated using a random velocity of sound in water, the SNR of τ_1 is effectively decreased even further.

Figure 3.6.1 shows the relative positions of the Source and Observer. V_s is the Source velocity with respect to the fixed X axis and V_o is the Observer velocity, also with respect to the fixed X axis.

In Figures 3.6.2 - 3.6.4, the Source has a horizontal velocity V_s of 20 (ft/sec) and the Observer a horizontal velocity V_o of 4 (ft/sec). This yields a 16 (ft/sec) relative horizontal velocity of the Source with respect to the moving Observer, at a time unknown to the Observer the target makes a major speed change as shown in Figure 3.6.3. The percent error in radial position is generally well within $\pm 3\%$ in Figure 3.6.2. The radial velocity estimates in Figure 3.6.3 continue to oscillate, but with smaller excursions than with $N = 3$ levels. In Figure 3.6.4, the excursions in the z_{so} estimates are on the average in error by 50 feet.

It appears, therefore, that increasing the number of mean values from 3 to 7 just about maintains the same filter performance in the face of reduced SNR on τ_1 and the modeling of the velocity of sound in water as a random process to generate the sonar time delay data. The oscillations in radial rate $\dot{\rho}$ are still present and a slight decrease has occurred in the quality of the vertical separation estimate.

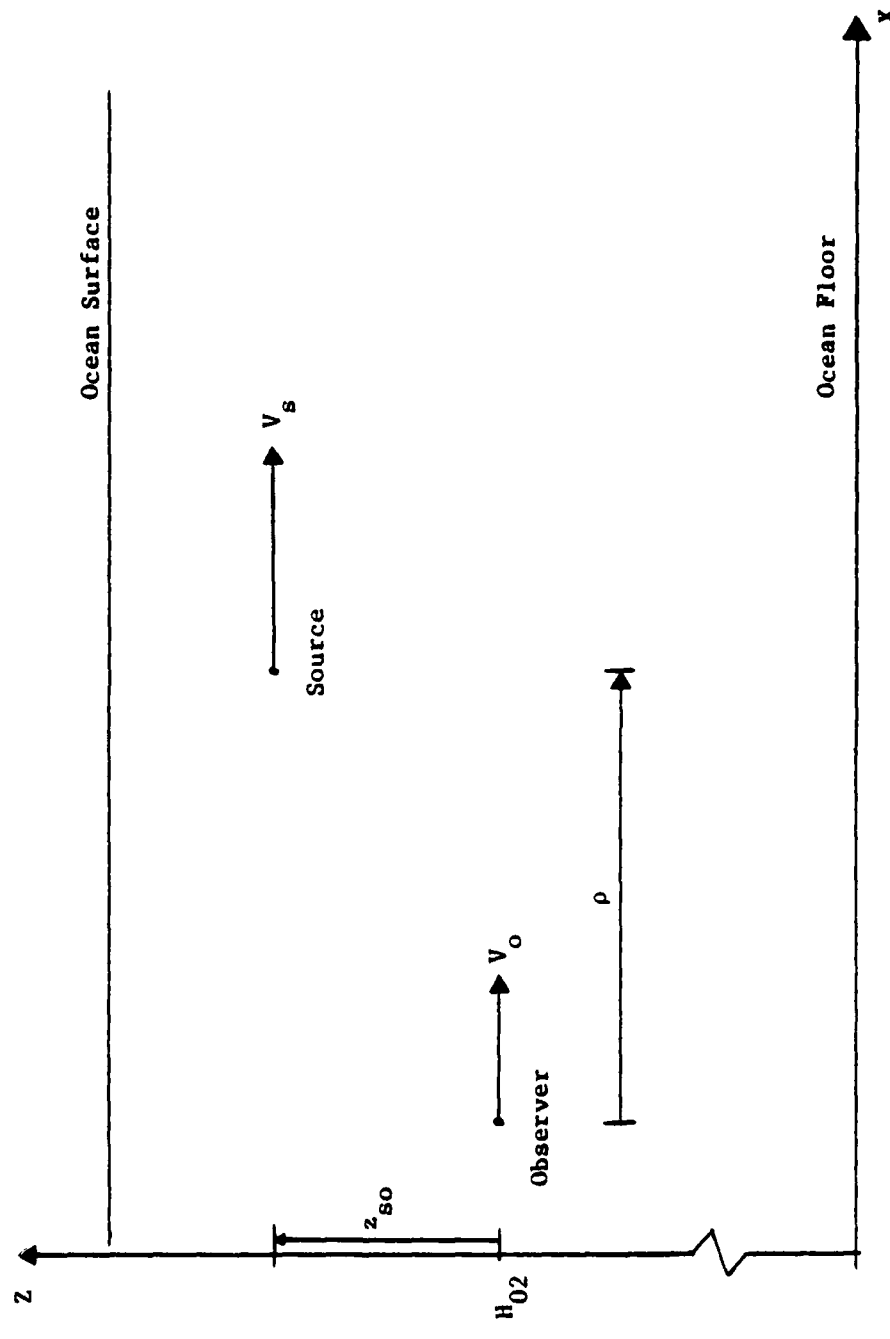


Figure 3.6.1 Relative Positions of Source and Observer

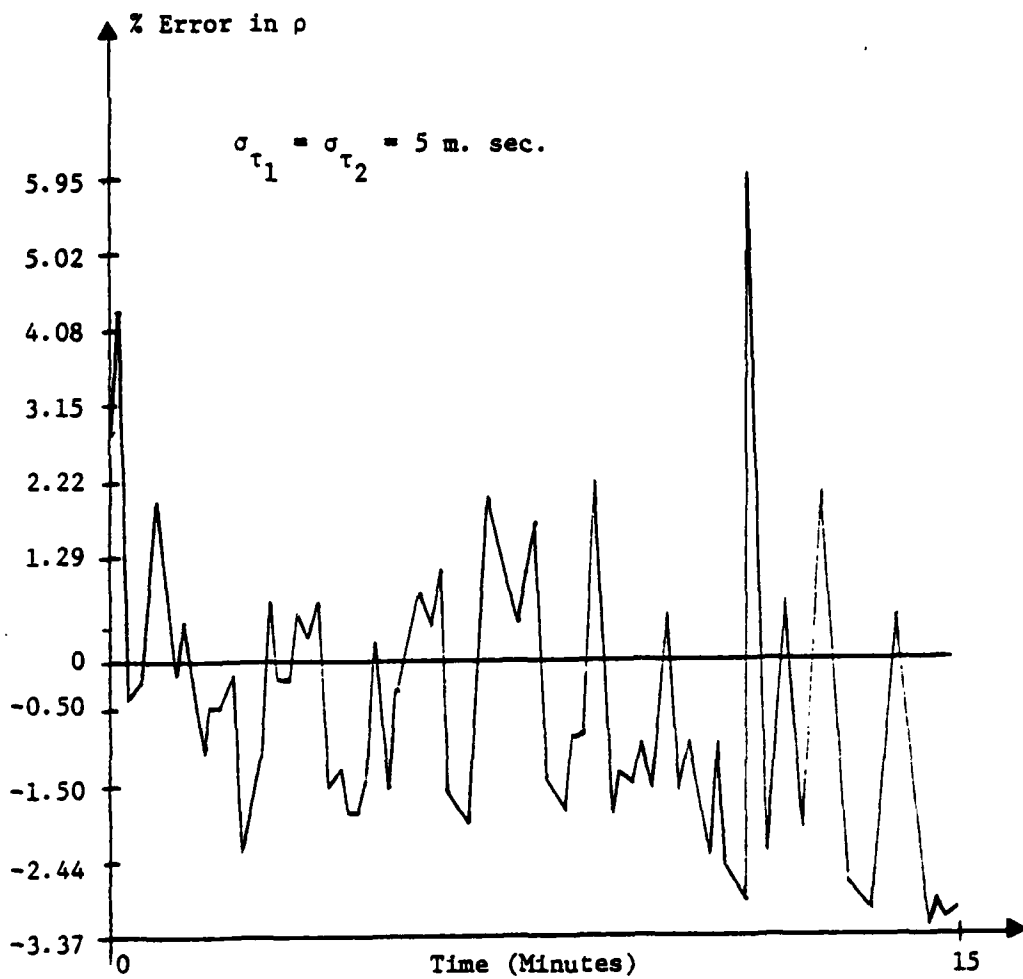


Figure 3.6.2 Percent Error in Source Relative Radial Position

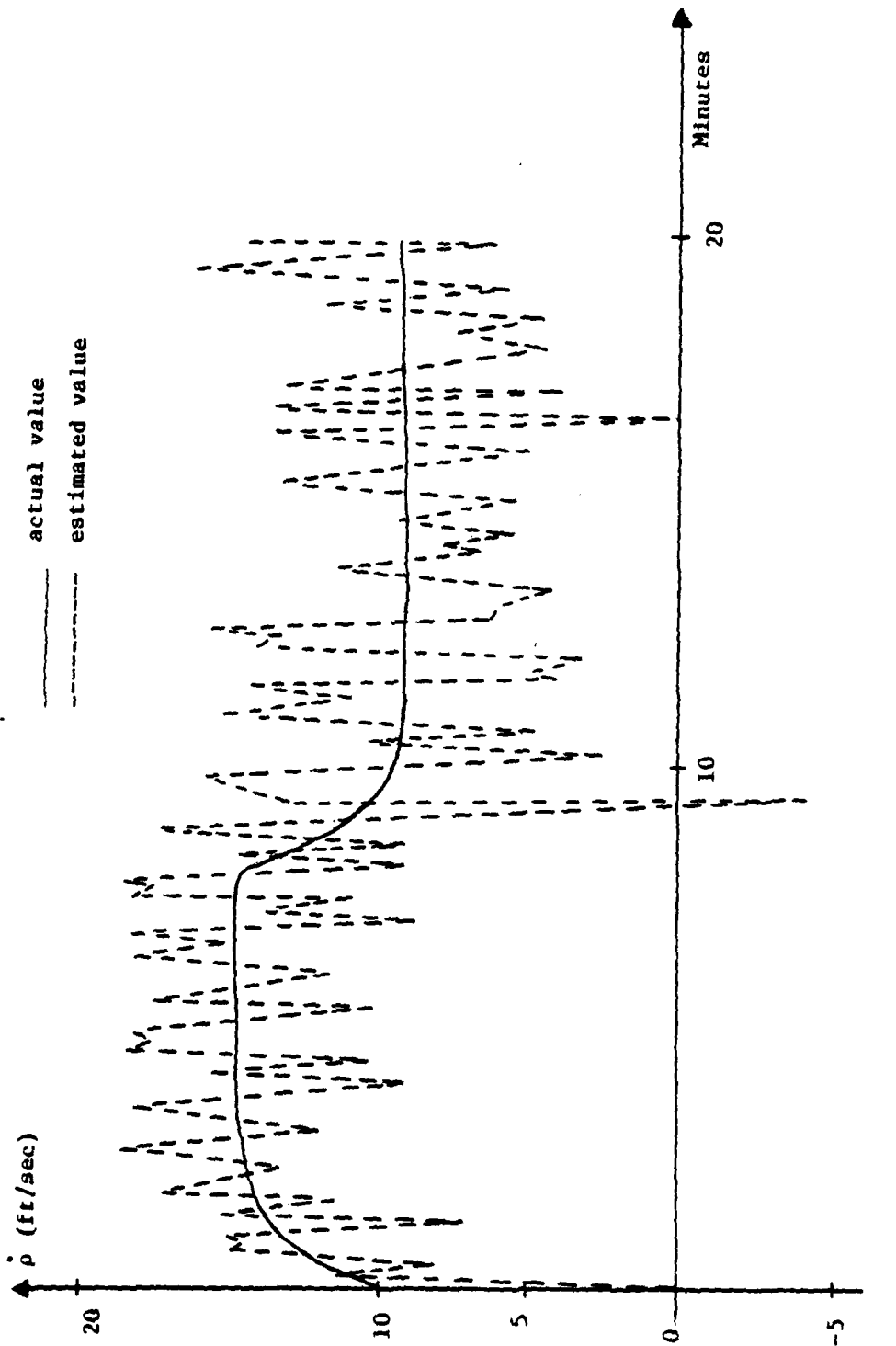


Figure 3.6.3 Actual and Estimated Source Relative Radial Velocity (3 levels)

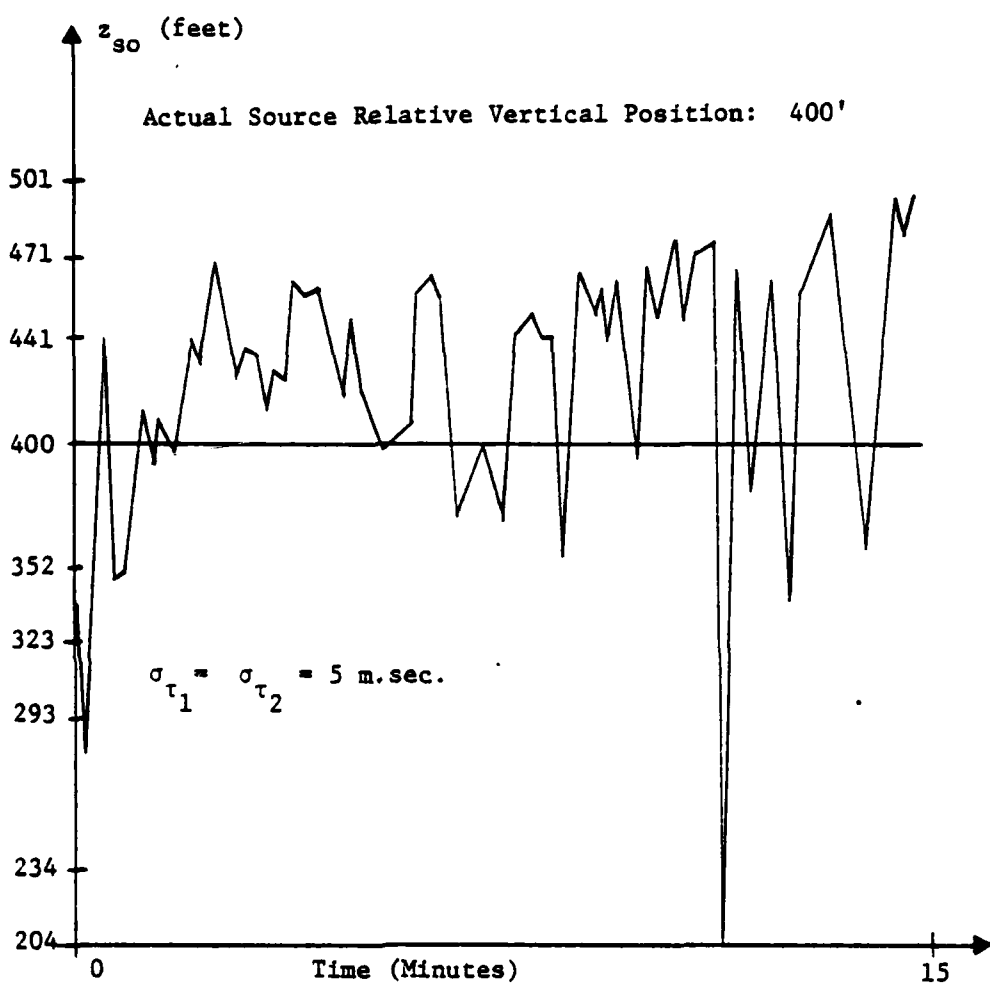


Figure 3.6.4 Estimate of Source Relative Vertical Position

3.7 Conclusion

Depending on the horizontal distance separating the Observer and Source, the ray paths in Figure 3.1.1 may undergo multiple reflections before arriving at the Source. By this is meant that the surface-reflected wave may be reflected back to the ocean floor and then back to the surface before arriving at the Observer. A similar situation exists for the bottom-reflected wave. Another problem which the sonar time delay tracker may have to contend with is the problem of intermittently available time delays. For example, the analysis in this chapter presupposes that the two time delays are available simultaneously. Under certain conditions, this fortuitous situation may not occur and the time delays may be individually available only at random times, or one or both of them may not be available at all for certain periods.

Thus the sonar time delay tracker is susceptible to a variety of debilitating influences. The decoupling of the bearing tracker from the processing of the time delays, which the Adaptive Polar Kalman filter developed in this chapter permits, enables bearing measurements to be processed even if the sonar time delays develop poor quality or are interrupted. With the rectangular filters, the processing of the bearing measurements is coupled to the processing of the sonar time delays, and any interruption of the latter brings the bearing estimation to a halt as well. Thus filtering in polar coordinates not only reduces the order of the measurement linearization matrix, but also localizes to the ρ - z plane the deleterious effects of poor quality sonar time delay measurement data.

The decoupling of the bearing channel as a result of filtering in polar coordinates has two important results: namely, that the order of the linearized measurement matrix H is reduced by one and the effects of poor or intermittently available sonar time delays are confined to the p-z plane. The estimates of the Source radial velocity become very poor under low SNR conditions on the sonar time delays.

Therefore a search for an i-dependent method of estimating the Source radial velocity is worthwhile. This method should function reliably and accurately regardless of the quality of the sonar time delay measurements. The remaining part of this report is devoted to developing an independent method which precisely satisfies these requirements.

Chapter 4

PASSIVE TRACKING OF SOURCE RELATIVE RADIAL VELOCITY PROFILE USING THE DOPPLER EFFECT AND KNOWN CONSTANT CENTER FREQUENCY

4.1 Introduction

It is shown at the end of Chapter 3 that passive tracking using sonar time delays yields acceptable results only when these measurements are characterized by high signal-to-noise ratios. However, even under such favorable conditions, oscillations occur in the estimates of the Source relative radial velocity; these oscillations increase as the SNR ratio decreases. This, in turn, causes the percent error in the Source relative radial position to increase and also leads to much poorer estimates of the Source relative vertical position. While it is true that the performance of any filter will suffer under adverse SNR conditions, the effect is particularly pronounced with both the Extended and Adaptive Extended Kalman filters, because of the approximate nature of these filters.

There exists another and to a considerable extent an independent method of determining estimates of the Source radial velocity (note that the term "relative" is dropped; from this point onward, and unless stated otherwise, whenever Source position or velocity is mentioned, it is implied that they are relative to the Observer). This method uses what is commonly known as the Doppler effect. The next section serves as a brief introduction to the Doppler effect. The remainder of this chapter is then devoted to using this

effect (assuming the "center frequency" f_0 is known) to passively track the radial velocity profile of a maneuvering source. The next chapter will address this problem assuming the center frequency is not known, but rather a random process.

4.2 The Doppler Effect for Sound Waves

Consider Figure 4.2.1(a). In this figure the stationary sound source A is transmitting a sound wave of frequency f_0 (also called the "center frequency"). Because of his motion, the frequency of the sound heard by the listener B is not the center frequency f_0 but some other frequency f_t to be determined. Before proceeding further, it should first be pointed out that r in Figure 4.2.1 refers to the separation of the source and listener in three-dimensional space--the spherical radius. For example, in (a) the listener might be a submarine and the source a floating sonar buoy providing navigation information by means of the Doppler effect. Thus r need not be horizontal as drawn. In addition, \dot{r} is the component of the listener's velocity vector acting along the radial direction r --the spherical radius rate. With the meaning of r and \dot{r} firmly established, refer again to Figure 4.2.1(a), where the listener is moving away from the stationary source with a radial velocity \dot{r} . This radial velocity imparts a shift [12]

$$\Delta f = - f_0 \dot{r} / C \quad (4.2.1)$$

to the center frequency, where C is the velocity of sound in the surrounding medium. This frequency shift is then added to the center

$$f_t = f_o \left[1 - \frac{r}{c} \right]$$

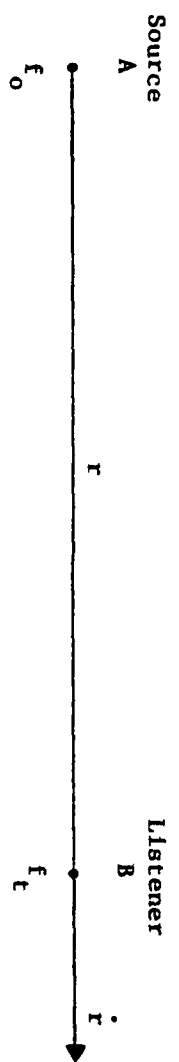


Figure 4.2.1(a) Stationary Source A and Moving Listener B

$$f_t \approx f_o \left[1 - \frac{r}{c} \right]$$

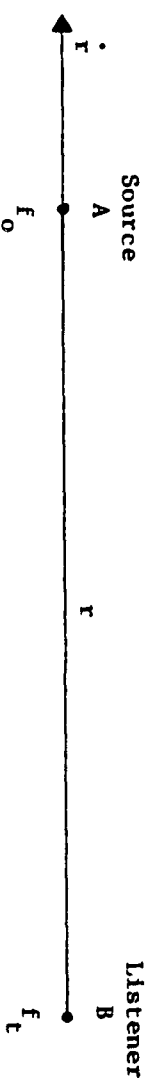


Figure 4.2.1(b) Moving Source A and Stationary Listener B

frequency and it is the sum of these two frequencies which the listener hears

$$f_t = f_o + \left(-\frac{v_o \dot{r}}{c} \right) = f_o [1 - \frac{\dot{r}}{c}] \quad (4.2.2)$$

Equation (4.2.1) implies that for a positive (negative) \dot{r} , the received frequency f_t in (4.2.2) is less (greater) than the center frequency f_o .

Now consider Figure 4.2.1(b) where the source is moving and the listener is stationary. The exact expression for the shift in this case is different from that given by (4.2.1). However, if the speed of the source is small compared to the speed of sound in the surrounding medium, then the shift imparted to f_o in case (b) simplifies to that given in (4.2.1) [12]. This implies that f_t in case (b) is also given by (4.2.2).

Now the typical underwater scenario where both the Source and Observer (Listener) are moving does not fall into either case (a) or (b) in Figure 4.2.1. To determine the formulas for the Doppler shift in this situation, Equation (20-11) in reference [12] states that for a moving Observer and Source

$$f_t = f_o \frac{(1 \pm \frac{v_o}{c})}{(1 \mp \frac{v_s}{c})}$$

where "the upper signs correspond to the Source and Observer moving along the line joining the two in the direction toward the other, and the lower signs in the direction away from the other." These two cases are now considered individually.

Case I Source and Observer moving toward each other with speeds v_s and v_o , respectively.

$$f_t = f_o \frac{\left(1 + \frac{v_o}{c}\right)}{\left(1 - \frac{v_s}{c}\right)} \approx f_o \left(1 + \frac{v_o}{c}\right) \left(1 + \frac{v_s}{c}\right)$$

if $\frac{v_s}{c} \ll 1$. Therefore

$$f_t \approx f_o \left(1 + \frac{v_o}{c} + \frac{v_s}{c}\right) = f_o \left(1 + \frac{v_o + v_s}{c}\right) \quad (4.2.3)$$

Let \dot{r} be defined as the rate of *increase* in the distance r separating the Observer and Source. Then since v_o and v_s are positive numbers (speeds)

$$\dot{r} = -(v_o + v_s)$$

is the relative radial velocity of the Source with respect to the moving Observer and is negative. Substituting this into (4.2.3)

$$f_t \approx f_o \left(1 - \frac{\dot{r}}{c}\right) \quad (4.2.4)$$

for $\dot{r} < 0$.

Case II Source and Observer moving away from each other with speeds v_s and v_o , respectively.

$$f_t = f_o \frac{\left(1 - \frac{v_o}{c}\right)}{\left(1 + \frac{v_s}{c}\right)} \approx f_o \left(1 - \frac{v_o}{c}\right) \left(1 - \frac{v_s}{c}\right)$$

if $\frac{v_s}{c} \ll 1$. Therefore

$$f_t \approx f_o \left(1 - \frac{v_o}{c} - \frac{v_s}{c}\right) = f_o \left(1 - \frac{v_o + v_s}{c}\right) \quad (4.2.5)$$

Defining \dot{r} as the rate of increase in r , then

$$\dot{r} = (v_o + v_s)$$

and \dot{r} is, once again, the relative radial velocity of the Source with respect to the moving Observer and is now positive. Substituting this into (4.2.5)

$$f_t \approx f_o (1 - \dot{r}/c) \quad (4.2.6)$$

for $\dot{r} > 0$.

Equations (4.2.4) and (4.2.6) are valid for $\dot{r} < 0$ and $\dot{r} > 0$, respectively. However, these two equations are identical and the conclusion is that either of these is the expression for the received frequency as measured at the moving Observer when \dot{r} is interpreted as the relative radial velocity of the moving Source with respect to the moving Observer. Therefore the situations in Figure 4.2.1 which lead to Equation (4.2.2) are both special cases of the more general case involving motion by both the Observer and Source. In summary, the Doppler shift Δf is given by (4.2.1) where \dot{r} is interpreted as the relative radial velocity of the Source with respect to the moving Observer and the received frequency measured at the Observer is given by Equation (4.2.6). Having discussed the Doppler effect in the presence of a moving Observer and Source, the use of this effect in passive tracking is now discussed.

4.3 Velocity Tracking Using the Doppler Effect

Consider the Observer-Source situation shown in Figure 3.6.1.

The distance r is given by

$$r = (\rho^2 + z_{so}^2)^{1/2}$$

and

$$\dot{r} = \dot{\rho} \left(\frac{\rho}{r} \right) + \dot{z}_{so} \left(\frac{z_{so}}{r} \right) \quad (4.3.1)$$

For the reasons cited in Chapter 3, there are only relatively short periods when $\dot{z}_{so} \neq 0$. Also for large values of r ,

$$\left(\frac{z_{so}}{r} \right) \approx 0$$

and

$$(4.3.2)$$

$$\left(\frac{\rho}{r} \right) \approx 1$$

The approximations in (4.3.2) have good physical justifications. The Source and Observer are, because of pressure buildup, very restricted in how far below the ocean surface they can safely penetrate. This restriction on vertical movement in turn places limitations on the extent of their vertical separation, z_{so} . There is no such restriction, however, on the horizontal distance separating them. Therefore, while the vertical separation z_{so} is measured in, say, hundreds of feet, the horizontal distance ρ is measured in miles or tens of miles.

In view of Equation (4.3.2), Equation (4.3.1) can be approximated as

$$\dot{r} \approx \dot{\rho} \quad (4.3.3)$$

and

$$\Delta f \approx - \frac{f_o \dot{\rho}}{C} = \left(\frac{-f_o}{C} \right) \dot{\rho} \quad (4.3.4)$$

where C is the velocity of sound in water.

This simplification of Equation (4.3.1) to (4.3.3) has, through Equation (4.3.4), shown that the Doppler shift is a linear function of the radial rate $\dot{\rho}$. Consequently the radial channel model for the maneuvering Observer-Source dynamics developed in Chapter 2

can now be used to passively track the Source radial velocity using (4.3.4). This model is repeated below for convenience.

$$\begin{bmatrix} \rho \\ \dot{\rho} \\ w_s' \\ s_p \end{bmatrix}_{k+1} = \begin{bmatrix} 1 & A & B \\ 0 & E & F \\ 0 & 0 & e^{-AT} \end{bmatrix} \begin{bmatrix} \rho \\ \dot{\rho} \\ w_s' \\ s_p \end{bmatrix}_k + \begin{bmatrix} C & (A-T) \\ A & (E-1) \\ 0 & 0 \end{bmatrix} \begin{bmatrix} u_{s_p} \\ v_o \cos \theta_{so} \end{bmatrix}_k + \begin{bmatrix} D \\ G \\ J \end{bmatrix} w_{s_p k}$$

Equation (4.3.4) shows that the radial velocity information is contained in the Doppler shift. However, the measured frequency f_m_{k+1} is not the shift, but rather the sum of the shift, center frequency f_o and measurement noise:

$$f_m_{k+1} = f_o + \Delta f_{k+1} + v_{k+1} \quad (4.3.5)$$

where

$$\Delta f_{k+1} = \left(\frac{-f_o}{C} \right) \dot{\rho}_{k+1} \quad (4.3.6)$$

If the known center frequency f_o appearing in (4.3.5) is looked upon as a fixed measurement bias added onto the shift Δf_{k+1} , then the bias can be directly removed since f_o is known in this chapter. Therefore, by prefiltering the measured frequency f_m_{k+1} , the resulting prefiltered measurement $\Delta f_{k+1} + v_{k+1}$

is a linear function of the state variable $\dot{\rho}$ as given by (4.3.6).

Using the state vector

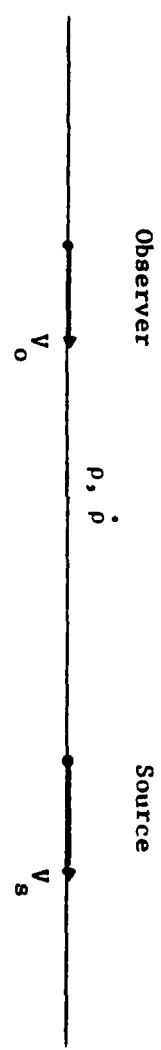
$$z_{k+1} = \Delta f_{k+1} + v_{k+1} = [0 \quad \left(\frac{v_0}{c}\right) \quad 0] \begin{bmatrix} \rho \\ \dot{\rho} \\ \ddot{\rho} \\ w_s \\ \rho \end{bmatrix}_{k+1} + v_{k+1}$$

$$z_{k+1} = Hx_{k+1} + v_{k+1} \quad (4.3.7)$$

and the adaptive Kalman filter algorithm can be applied to these noisy measurements (4.3.7) using the earlier parameter values of Chapter 3.

Consider now Figure 4.3.1 where the Source and Observer are moving horizontally, the latter at a constant velocity $v_o = 2$ ft/sec. The Source makes several abrupt changes in its velocity as shown by the solid line in Figure 4.3.2. The dotted line in this figure gives the weighted estimate produced by the adaptive Kalman filter using the noisy frequency measurements given by (4.3.5). This weighted estimate is seen to closely track the abruptly changing velocity profile of the Source with relatively small lag time. These good velocity estimates provide a reassuring test of the accuracy of the state equation for $\dot{\rho}$ in compensating for Observer motion. To appreciate this point, first note that $\dot{\rho}$ is the relative radial velocity of the Source with respect to the moving Observer. Consequently, any significant error in compensating for the component of the Observer's own velocity acting in the radial direction will ultimately result in a bias on the estimate of the Source radial velocity. This bias is clearly absent in Figure 4.3.2.

Figure 4.3.1 Relative Position of Observer and Source in Obtaining the Results in Figures 4.3.2 and 4.3.3



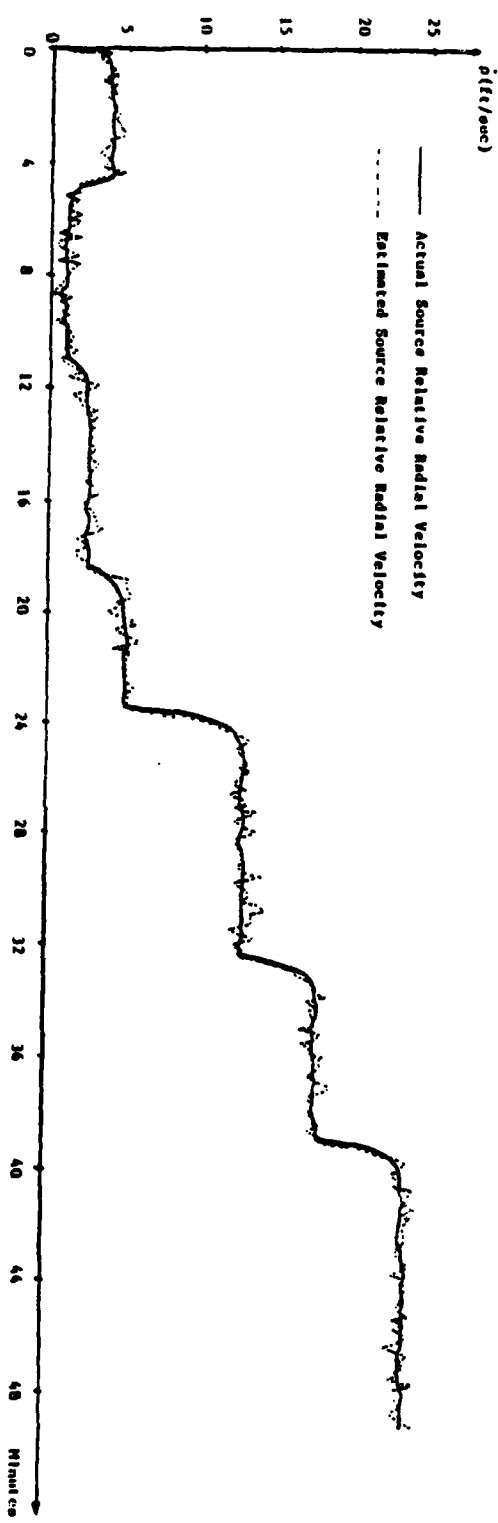


Figure 4.3.2 Relative Radial Velocity of Maneuvering Source with Respect to the Moving Observer Using Doppler Frequency Measurements and Known Center Frequency

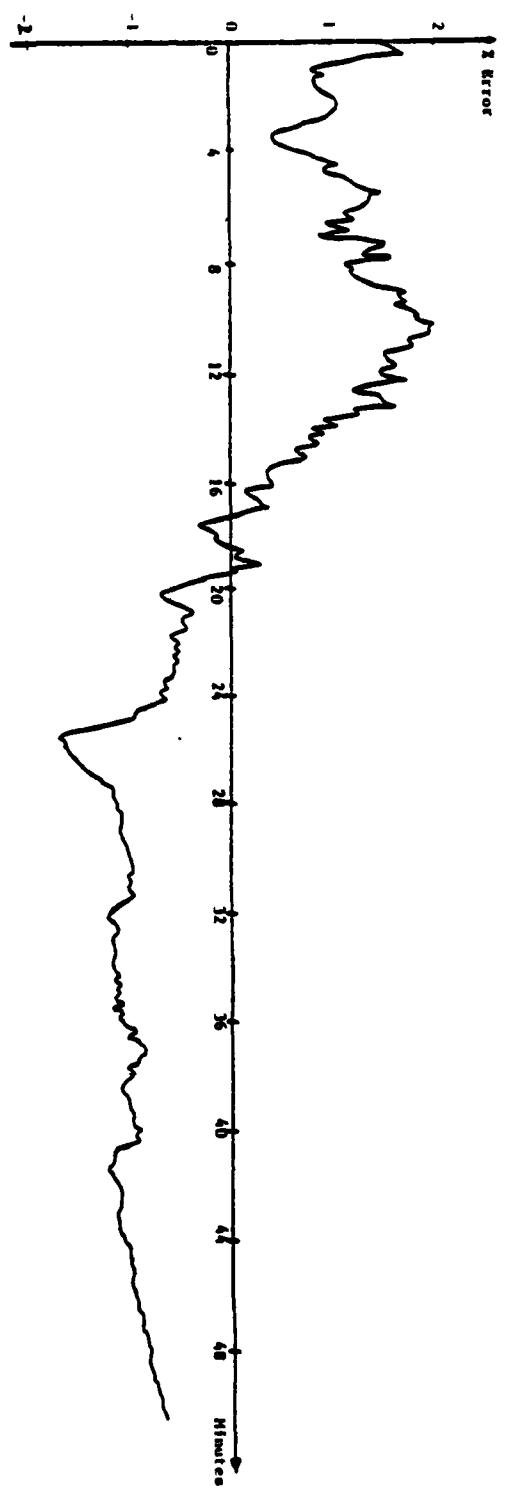


Figure 4.3.3 Percent Error in Source Relative Radial Position Using Doppler Frequency Measurements and Known Center Frequency

The trajectory in Figure 4.3.2 also provides a check on the "integrating effect" of the state model in the following manner. A very good initial estimate of the Source radial position is assumed at $t = 0$ in Figure 4.3.3. Then the state equation for ρ_{k+1} "integrates" the combined effect of the Source radial velocity estimate and the Observer radial velocity to arrive at the Source radial position estimate $\hat{\rho}$ at each time step. The percent error in Source radial position at each step is then calculated and the results are plotted in Figure 4.3.3. It is seen that over a period of 50 minutes the percent error in Source radial position never exceeds $\pm 2\%$. These results attest to the accuracy of the state equation for ρ , particularly in its compensation for Observer motion.

4.4 Conclusion

The tracking of a maneuvering Source velocity profile using the Doppler effect and known center frequency f_0 is a relatively straightforward filtering problem in polar coordinates. The adaptive polar filter developed in Chapter 2 performs well in responding to abrupt changes in Source radial velocity. Assuming a good initial estimate of Source radial position, the adaptive filter "integrates out" the velocity estimates to yield good position estimates. These radial position estimates remain within $\pm 2\%$ of the true radial position in the presence of several velocity changes by the Source. These results indirectly attest to the accuracy of the linearized polar state variable model for the maneuvering Observer-Source scenario, particularly in its compensation for Observer velocity.

Chapter 5

PASSIVE TRACKING OF SOURCE RADIAL VELOCITY USING THE DOPPLER EFFECT IN THE PRESENCE OF A RANDOMLY VARYING CENTER FREQUENCY

5.1 Introduction

In Chapter 4, the Doppler effect is used to passively track the Source radial velocity assuming the center frequency f_o is known. Typically, a submarine emits a broad sound spectrum having several discrete line spectra. These line spectra are often generated by machinery on board the Source. As previously discussed any of these frequencies can serve as the center frequency f_o emitted by the Source. However, under realistic tactical situations, this center frequency f_o is either *unknown* or a slowly varying random process. From previous work we know that the Doppler information is contained in the shift Δf . Unfortunately it is not the shift, but rather the sum of the shift and center frequency which is measured by the Observer, as indicated in Chapter 4. Therefore the measured frequency f_m is virtually useless for estimating the Source radial velocity unless the center frequency is known or estimated. The received frequency f_t (ignoring measurement noise) as measured by the Observer is given by

$$f_t = f_o + \Delta f = f_o - \frac{f_o p}{C} \quad (5.1.1)$$

where the parameters f_o , p and C have been described in detail in the previous chapter. Since f_o is unknown, then for any given value for f_t , there exists an infinity of possible combinations of values for f_o and Δf which sum together to give f_t . Any algorithm, therefore, designed to

process f_t must be cognizant of this fact and take steps to select the correct pair of values. Another important point to note is that in order to estimate f_0 , it must be defined as a state variable. The full implication of this can be realized by referring to

$$\Delta f = - \frac{f_0 \dot{p}}{c}$$

This equation shows that the shift Δf now involves the product of the state variables \dot{p} and f_0 and consequently a nonlinear estimation problem must be solved in order to process the Doppler measurement. In short, the assumption that f_0 is unknown or random has the following two results:

1. It increases the number of state variables (and hence the order of the system) by one and
2. it increases the complexity of the problem by transforming the linear estimation problem of Chapter 4 into a nonlinear estimation problem involving the product of state variables.

It was stated in Section 2.2 that "the Extended Kalman filter is usually the first filter to be used when confronted with either system or measurement nonlinearities." Rather than using the Extended Kalman filter, an entirely different approach is used. This new approach consists of performing a "transformation" on the problem which shifts the nonlinearity in such a manner that it can be "disposed of" in a relatively easy manner. Then a "pseudo-linear" filter is developed to process the nonlinear measurements (5.1.1), using essentially basic linear filtering theory. The details will become clear as the development proceeds.

5.2 State Variable Model for Doppler Measurements of a Random Center Frequency

The received frequency $f_{t_{K+1}}$ neglecting noise at time t_{K+1} , and

random center frequency $f'_{o_{k+1}}$ becomes

$$f'_{t_{k+1}} = f'_{o_{k+1}} + \left(\frac{-f'_{o_k}}{C} \right) p_{k+1} \quad (5.2.1)$$

Now, by using equation (2.3.12) for Range rate (\dot{p}_{k+1}) we can rewrite (5.2.1) when the substitution

$$\begin{aligned} \dot{p}_k &= \frac{f'_{t_k} - f'_{o_k}}{-f'_{o_k}/C} \quad \text{is made.} \\ &= \end{aligned}$$

After making several cancellations

$$f'_{t_{k+1}} = f'_{o_{k+1}} + \left(\frac{f'_{o_{k+1}}}{f'_{o_k}} \right) E(f'_{t_k} - f'_{o_k}) + \left(\frac{-f'_{o_{k+1}}}{C} \right) \left[\frac{Fw'_s}{p_k} + \dots \right].$$

Letting the center frequency at time $(k+1)T$ be

$$f'_{o_{k+1}} = f'_{o_k} + \delta f'_{o_k}$$

where $\delta f'_{o_k}$ is the purely random variation which f'_{o_k} undergoes to produce $f'_{o_{k+1}}$. Note that $\delta f'_{o_k}$ is entirely unrelated to the Doppler effect.

Now for a small variance on $\delta f'_{o_k}$, the ratio $\frac{f'_{o_{k+1}}}{f'_{o_k}}$ on the average is near unity.

Thus by making this approximation in (5.2.2), and bringing $f'_{o_{k+1}}$ over to the left side then defining

$$\Delta f_{k+1} \equiv f'_{t_{k+1}} - f'_{o_{k+1}}$$

$$\Delta f_k \equiv f'_{t_k} - f'_{o_k}$$

we get for the first Doppler state equation

$$\Delta f_{k+1} = E \Delta f_k + \left(\frac{-f'_{o_k}}{C} \right) \left[\frac{Fw'_s}{p_k} + \frac{Au'_s}{p_k} + (E-1) (V_o \cos \beta_{do})_k + \frac{Gw_s}{p_k} \right] \quad (5.2.3)$$

Note that the approximation $(\frac{-f'_o}{C})_k$ was substituted for $(\frac{-f'_o}{C})_{k+1}$ on the right side in (5.2.3). In order to make the problem tractable, the assumption that f'_o is Gaussian with a mean value f_o is made. Let f'_o be described by the following autocorrelation function

$$R_{f'_o}(\tau) = f_o^2 + o_{f'_o}^2 e^{-a_{f'_o} |\tau|} \quad (5.2.4)$$

where

$$f_o = E\{f'_o(t)\}$$

By converting to discrete time kT , $(k+1)T$, ... the random process $w_{f'_o}(t_{k+1})$ becomes

$$w'_{f'_o}_{k+1} = e^{-a_{f'_o} T} w'_{f'_o}_k + \frac{1}{a_{f'_o}} (1 - e^{-a_{f'_o} T}) w_{f'_o}_k \quad (5.2.5)$$

and letting $J \equiv \frac{1}{a_{f'_o}} (1 - e^{-a_{f'_o} T})$ as before

equation 5.2.5 becomes

$$f'_{o_{k+1}} = f_o + e^{-a_{f'_o} T} w'_{f'_o}_k + J w_{f'_o}_k \quad (5.2.6)$$

The expression (5.2.6) is not yet in proper state variable form because of the presence of the unknown mean value f_o . This mean value can be eliminated by subtracting

$$f_o = (f'_{o_k} - w'_{f'_{o_k}})$$

and substituting this expression into (5.2.6) for f_o yielding

$$f'_{o_{k+1}} = f'_{o_k} - w'_{f'_{o_k}} + e^{-a_f T} w'_{f'_{o_k}} + J w'_{f'_{o_k}}$$

Collecting like terms, the following discrete time state equation for the randomly varying center frequency f' becomes

$$f'_{o_{k+1}} = f'_{o_k} + (e^{-a_f T} - 1) w'_{f'_{o_k}} + J w'_{f'_{o_k}} \quad (5.2.7)$$

The state equations (5.2.3), (5.2.5) and (5.2.7) collectively form the Doppler frequency state variable model (5.2.8) with measurement model given by (5.2.9), and are summarized on the following page.

The following observations are now in order. The auto-correlation function (5.2.4) was chosen with the following properties in mind:

1. It represents a random process having a mean value f_o .
2. The exponential correlation is versatile in that it provides a tractable yet realistic model for actual random phenomena. In addition, the parameter a_f can be adjusted to model processes having bandwidths varying from wide to very narrow.

The added complexity of a random center frequency f'_o has increased the order of the state variable model by one. Note that the state equation for f'_o (second row in (5.2.8)) has the term J in the Ψ matrix. This term provides a means of setting a lower bound on the magnitude of the error covariance for the conditional estimate $\hat{f}'_o^{(1)}$. No such term exists in the unknown constant center frequency case. This is an added

DOPPLER FREQUENCY STATE VARIABLE MODEL.

$$(1) \quad \begin{bmatrix} \Delta f \\ f'_o \\ w'_{f_o} \end{bmatrix}_{k+1} = \begin{bmatrix} E & -[Rw'_s]^{(1)}_p + Au_s^{(1)}_p + (E-1)(v_o \cos \beta_{so})_k / c \\ 0 & 1 \\ 0 & 0 \end{bmatrix} \begin{bmatrix} \Delta f \\ f'_o \\ w'_{f_o} \end{bmatrix}_k +$$

$$\begin{bmatrix} -f'_o G \\ C \\ 0 \\ 0 \end{bmatrix} \begin{bmatrix} 0 \\ w'_s \\ w'_{f_o} \\ J \end{bmatrix}_k$$

$$\text{or } x_{k+1}^{(1)} = \phi x_k^{(1)} + \psi w_k$$

MEASUREMENT MODEL

$$f_m_{k+1} = \left[\Delta f_{k+1} + f'_{o_{k+1}} + v_{k+1} \right] = \begin{bmatrix} 1 & 1 & 0 \end{bmatrix} \begin{bmatrix} \Delta f \\ f'_o \\ w'_{f_o} \end{bmatrix}_{k+1} + v_{k+1} \quad (5.2.9)$$

"benefit" of the random center frequency assumption.

Like the previous Doppler frequency models, (5.2.8) is not a linear state variable model because of the presence of the state variable f'_o in the Ψ matrix. However, since f'_o is a random process, initialization using the first noisy frequency measurement can be applied to (5.2.8) to make it a pseudo-linear time-varying state variable model.

The presence of w'_{s_p} in (5.2.8) indicates that this Doppler frequency state model also requires interaction with the reduced order radial channel model given in Chapter 2 by

$$\begin{bmatrix} \dot{p} \\ w'_{s_p} \end{bmatrix}_{k+1}^{(i)} = \begin{bmatrix} E & F \\ 0 & e^{-aT} \end{bmatrix} \begin{bmatrix} \dot{p} \\ w'_{s_p} \end{bmatrix}_k^{(i)} + \begin{bmatrix} A & (E-1) \\ 0 & 0 \end{bmatrix} \begin{bmatrix} u_{s_p} \\ v_o \cos \beta_{so} \end{bmatrix}_k + \begin{bmatrix} G \\ J \end{bmatrix} w_{s_p}^{(i)k}$$

This will allow $w'_{s_p}(tk)$ to be estimated and then used in the Doppler filter dynamics matrix ϕ equation (5.2.8). In addition, $(e^{-a_f o T} - 1)$ and

$\frac{1}{a_f o} (1 - e^{-a_f o T})$ appearing in the Doppler frequency equation (5.2.7) are functions only of the correlation time constant

$$\tau_{f_o} = \frac{1}{a_f o}$$

in the autocorrelation function.

5.3 Performance Analysis of the Doppler Frequency State Variable Model for the Randomly Varying Center Frequency Case

Figure (5.3.1) shows the structure of the filter to be analyzed in this chapter. Each block consists of a Kalman Filter, either Doppler frequency to the left, or polar range estimator to the right. The inputs are the N discrete levels $U_{s_p}^{(i)}$, and each filter is now separately computed since the state matrices are functions of (i). Thus N sets of frequency and

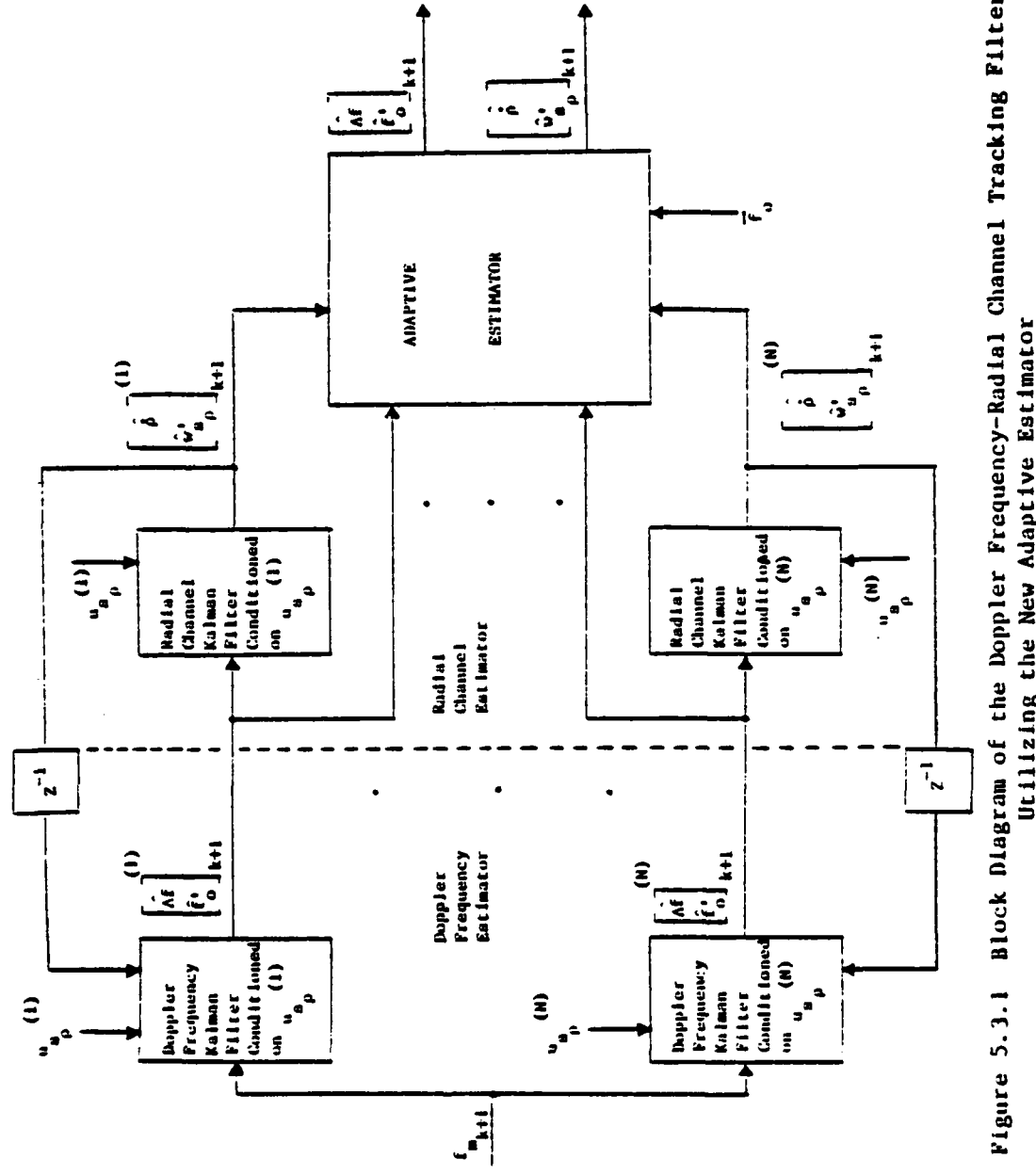


Figure 5.3.1 Block Diagram of the Doppler Frequency-Radial Channel Tracking Filter Utilizing the New Adaptive Estimator

radial channel estimates are produced, each set being conditioned on a different mean value $u_{sp}^{(i)}$, $i = 1, 2, \dots, N$. The reason why this particular filter structure is chosen will become clear later when the block labeled "Adaptive Estimator" is discussed. For the present the operation of the filter without the adaptive portion is examined. This will serve to gain an appreciation for the filter's operating characteristics which will then set the framework for developing the adaptive section.

Figure (5.3.2) is a block diagram of the model used to generate the noisy frequency measurement data. The quantity \dot{r} appearing there is the Course spherical radius rate and is essentially a random process having an unknown distribution. This rate then multiplies the random center frequency f'_o and this product is divided by the velocity of sound in water. In the first series of results to be discussed below, this velocity is assumed to be a constant C (switch open in Figure (5.3.2)). The switch will then be closed for the later results when the velocity of sound in water is modeled as a white Gaussian random process having a mean value C. The zero mean white Gaussian curves on the extreme left and right of the figure represent the distributions of w_{fok} and v_{k+1} in Equations (5.2.5) and (5.2.9), respectively. Thus the noisy measurement $f_{m_{k+1}}$ in Figure (5.3.2) is a relatively complex combination of products, quotients and sums of random processes, most of whose distributions (f'_o , \dot{r} , Δf , f_t) are unknown.

The following results are obtained using the scenario in Figure (3.6.1) whereby the observer trails the source with velocity

$$V_o = 2 \text{ ft/sec, and } V_s = 20 \text{ ft/sec.}$$

The filter parameters and mean values are given in Chapter 3. The following additional parameters have the indicated values:

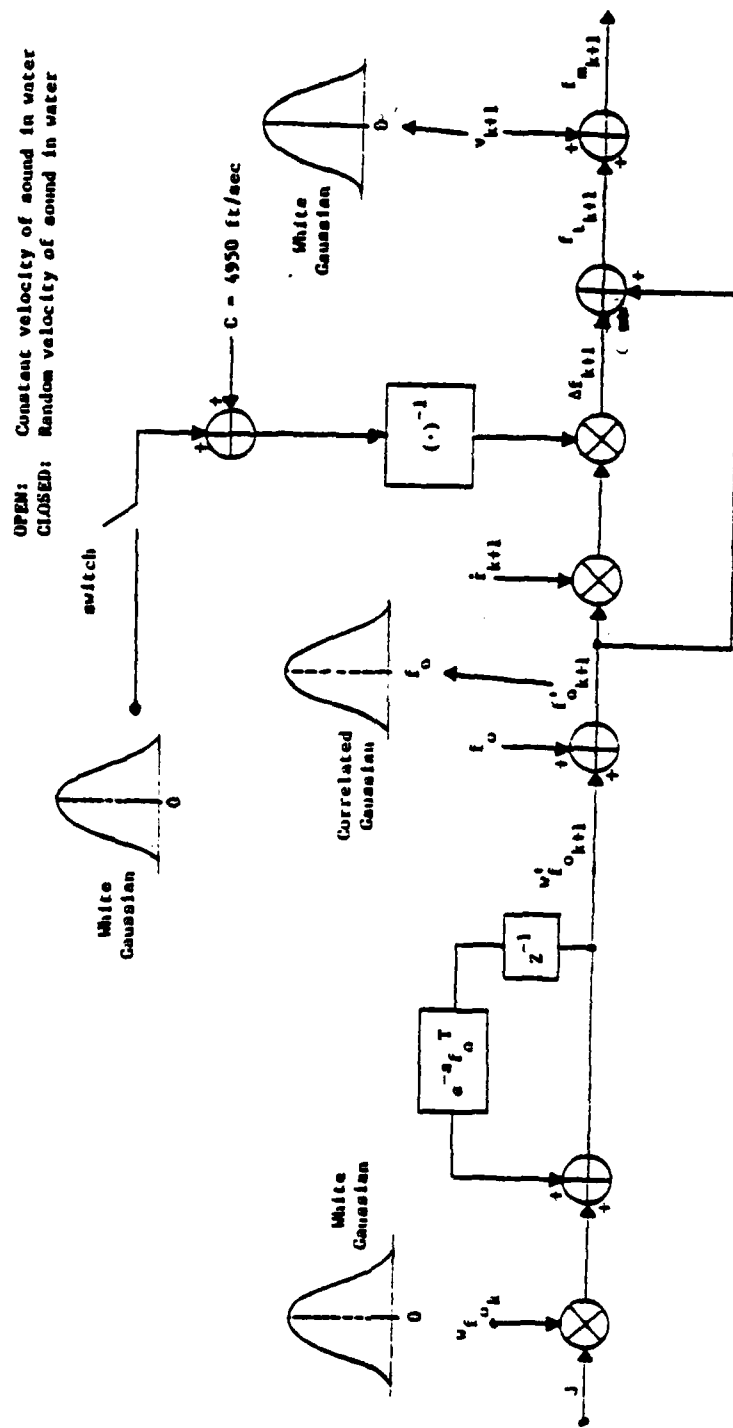


Figure 5.3.2 Block Diagram of the Model Used to Generate the Noisy Doppler Frequency Measurement Data

$$\sigma_{f_o} = 0.3 \text{ Hertz}$$

$$\tau_{f_o} = 17 \text{ seconds}$$

$$f_o = 500 \text{ Hertz (mean value of Random Center Frequency } f'_o)$$

$$C = 4950 \text{ ft/sec}$$

Frequency measurement noise standard deviation is the same as before.

This latter set of values is selected to produce a random center frequency having significant excursions about the mean value of 500 Hertz; the correlation time constant being less than two sampling intervals ensures that the random variation in frequency is quite rapid.

The Source velocity of 20 ft/sec corresponds to a Source control input

$$u_{s_p} = \alpha v_s = (0.05)(20) = 1.0$$

This Source input lies midway between the sixth and seventh filter mean values $u_{s_p}^{(6)} = 0.8$ and $u_{s_p}^{(7)} = 1.2$, respectively.

Figure (5.3.3) shows the seventh ($\hat{f}'_o^{(7)}$), sixth ($\hat{f}'_o^{(6)}$) and fifth ($\hat{f}'_o^{(5)}$), virtual center frequencies (VCF) versus the actual random center frequency f'_o . The remaining four VCFs, which lie progressively further below $\hat{f}'_o^{(5)}$ in the figure, are not shown for reasons of clarity. Note how each VCF closely follows the random variations of f'_o . Throughout the entire time period of 18 minutes, the actual center frequency is generally bracketed midway between the seventh and sixth VCFs. This is particularly satisfying since the Source input is likewise bracketed between the sixth and seventh mean values.

When either the Observer or Source changes its radial velocity, an immediate jump occurs in the measured frequency f_m . Consequently it is im-

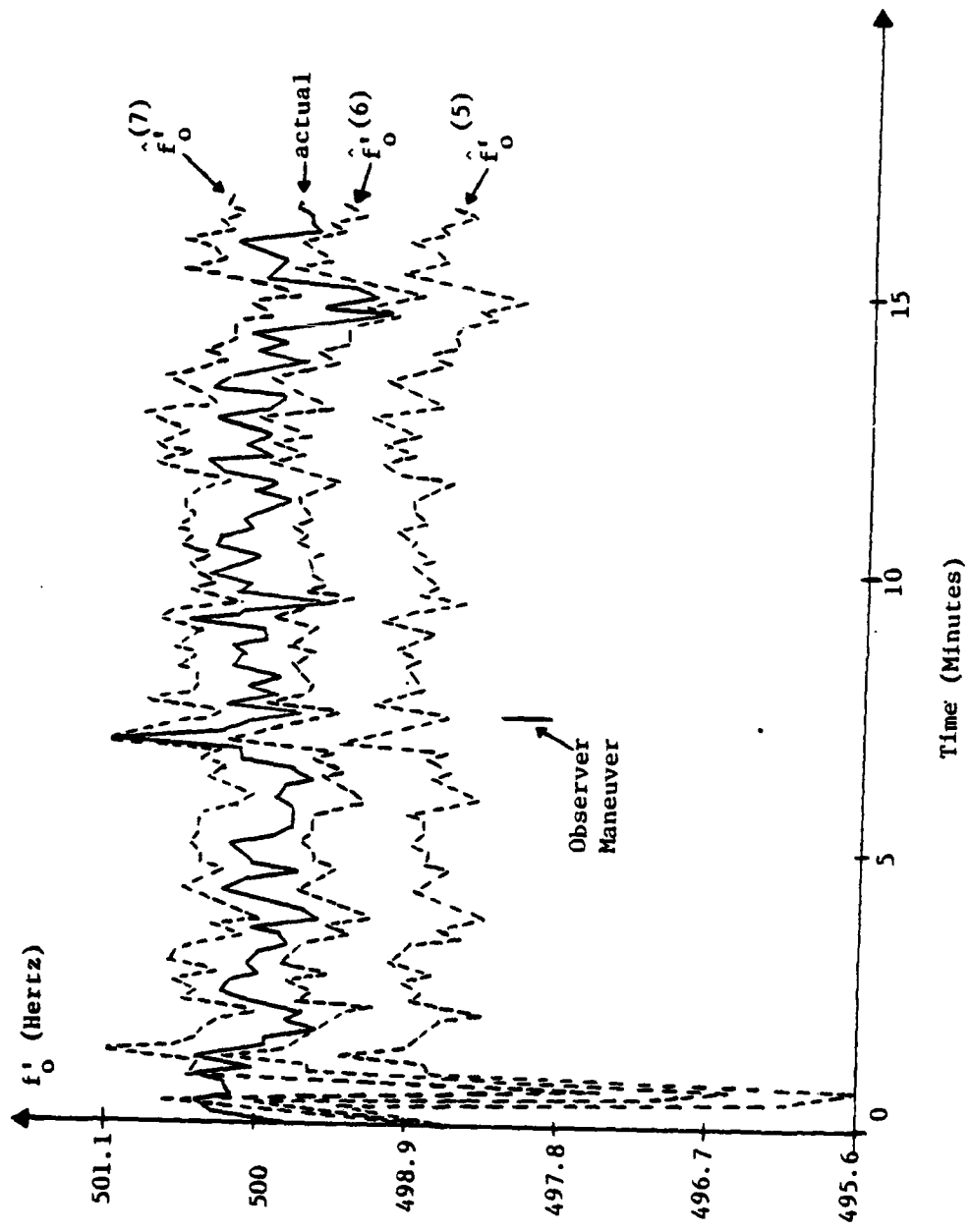


Figure 5.3.3 Actual versus Virtual Center Frequencies in
the Presence of an Observer Maneuver

portant that the filter be able to discriminate between a jump in the measured frequency caused by an Observer maneuver on the one hand and a Source maneuver on the other. To investigate this, the Observer speed v_o is increased from 2 ft/sec to 8 ft/sec beginning at $t = 7.5$ minutes. First note that since this is an Observer maneuver only, the Source input has not changed and continues to be bracketed between the two mean values as before.

From Figure (5.3.3) this Observer maneuver is not reflected in the estimates and the actual center frequency continues to be bracketed between the sixth and seventh VCFs as before. This is to be expected as this shows that the filter recognized the jump in measured frequency as having been caused by an Observer maneuver.

Consider now Figure (5.3.4) which shows the three virtual Doppler shifts $\hat{\Delta f}^{(5)}$, $\hat{\Delta f}^{(6)}$ and $\hat{\Delta f}^{(7)}$ versus the actual Doppler shift. Here, the actual shift is bracketed between $\hat{\Delta f}^{(6)}$ and $\hat{\Delta f}^{(7)}$ as required by $u_{sp}^{(7)} < u_{sp}^{(6)} < u_{sp}^{(5)}$. Note that the Observer maneuver is reflected in the virtual Doppler shifts. To understand why this is necessary, first note that a sudden change in the Observer velocity v_o causes a sudden change in the Source relative radial velocity $\dot{\rho}$. This sudden change in $\dot{\rho}$ in turn causes a sudden change in the actual Doppler shift Δf . However, since the Source input has not changed, the virtual shifts (VS) must change in such a way that Δf remains bracketed midway between $\hat{\Delta f}^{(6)}$ and $\hat{\Delta f}^{(7)}$.

Figures (5.3.3) and (5.3.4) together illustrate how the filter exploits its degree of freedom by satisfying the required inequalities. For example, note how the VCFs in Figure (5.3.3) satisfy

$$\hat{f}_o^{(5)} < \hat{f}_o^{(6)} < \hat{f}_o^{(7)}$$

while the VS's in Figure (5.3.4) satisfy

$$\hat{\Delta f}^{(5)} < \hat{\Delta f}^{(6)} < \hat{\Delta f}^{(7)}$$

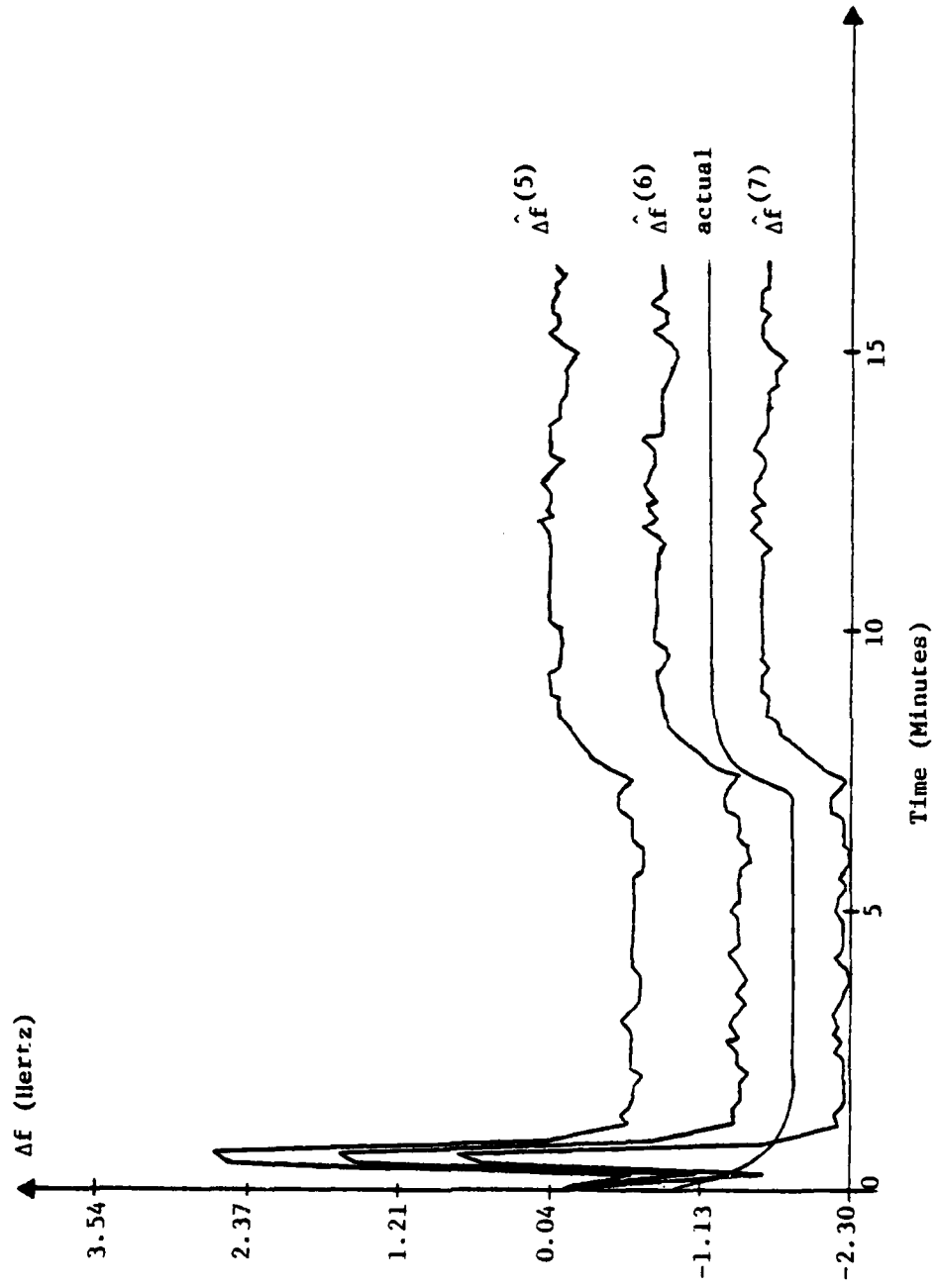


Figure 5.3.4 Actual versus Virtual Doppler Shifts in the Presence of an Observer Maneuver

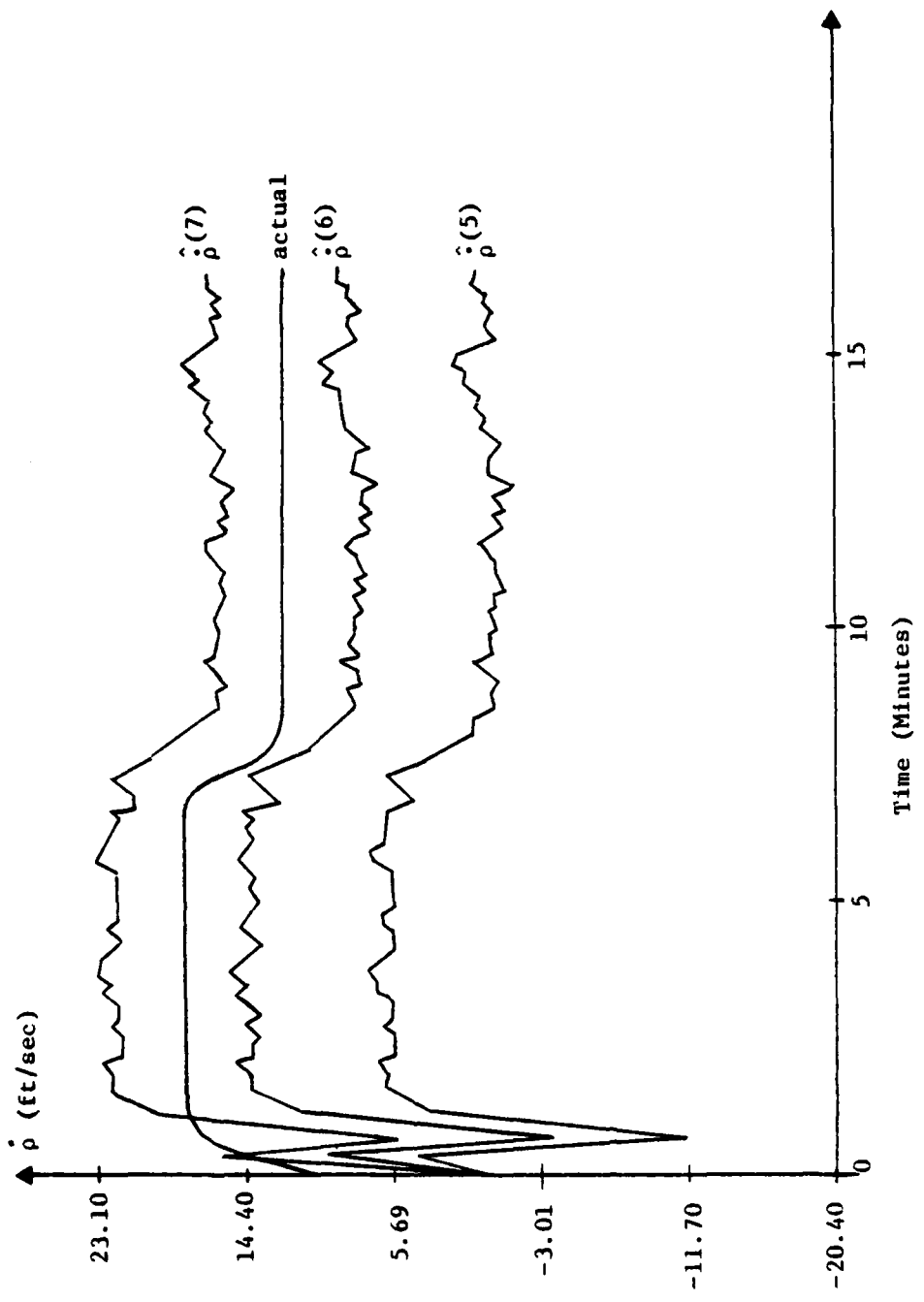


Figure 5.3.5 Actual versus Virtual Radial Velocities in the Presence of an Observer Maneuver

The actual Source radial velocity $\dot{\rho}$ in Figure (5.3.5) remains bracketed between the virtual radial velocities (VRV) $\hat{\dot{\rho}}^{(6)}$ and $\hat{\dot{\rho}}^{(6)}$ and $\hat{\dot{\rho}}^{(7)}$ in the presence of the Observer maneuver. Here again, since the Source input has not changed, the filter responds by changing the VRVs to maintain the actual value midway between the sixth and seventh VRVs.

The behavior of this filter in the presence of a Source maneuver is examined in the next three figures. With the same set of parameters and initial conditions as in the preceding figures, the Source velocity \dot{v}_s changes from 20 to 12 ft/sec beginning at $t = 7.5$ minutes. The new Source input $u_s = 0.6$ is midway between $u_{s_p}^{(5)}$ and $u_{s_p}^{(6)}$.

The response to this Source maneuver is radically different from that for the Observer maneuver. Consider for example Figure (5.3.6) where we see that after the Source maneuver at $t = 7.5$ minutes, the VCFs all shift upward by an amount sufficient to have the actual center frequency f'_o bracketed midway between the fifth and sixth VCFs. The response time of the filter is quite good as this upward shift by the estimates is immediately perceptible at the initiation of the maneuver. Note how the VCFs continue to follow the random variations of f'_o both before and after the maneuver.

In Figure (5.3.7) the actual shift which is initially bracketed between the sixth and seventh VS's before the maneuver ends up midway between the fifth and sixth VS's after the maneuver. This same situation applies to the radial velocity $\dot{\rho}$ in Figure (5.3.8). Note how the degree of freedom continues to be exploited by the filter in Figures (5.3.6) and (5.3.7).

To summarize, the filter bank in Figure (5.3.1) is shown to be capable of tracking the Doppler shift, random center frequency and radial velocity fluctuations in the presence of either an Observer or a Source

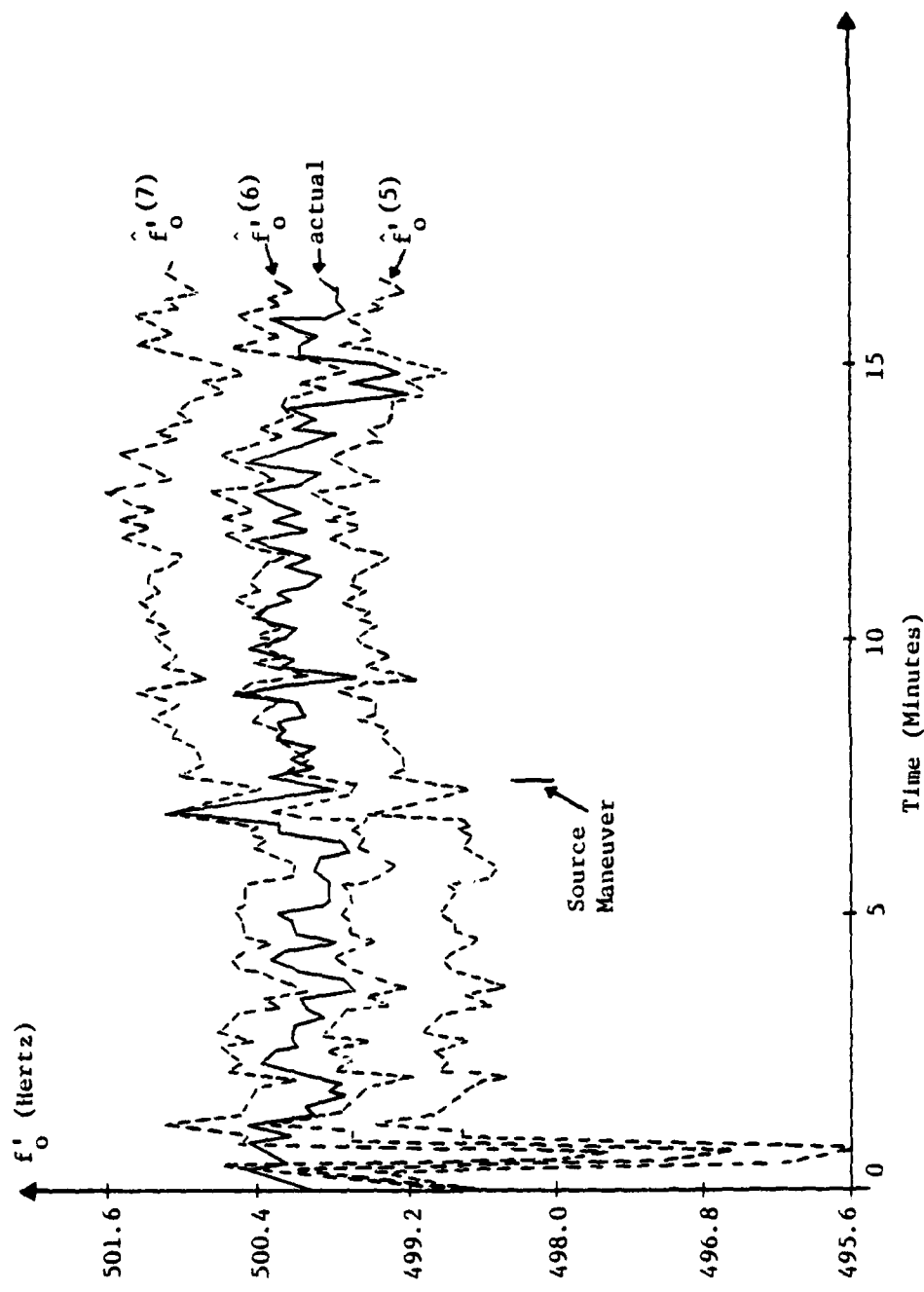


Figure 5.3.6 Actual versus Virtual Center Frequencies in the Presence of a Source Maneuver

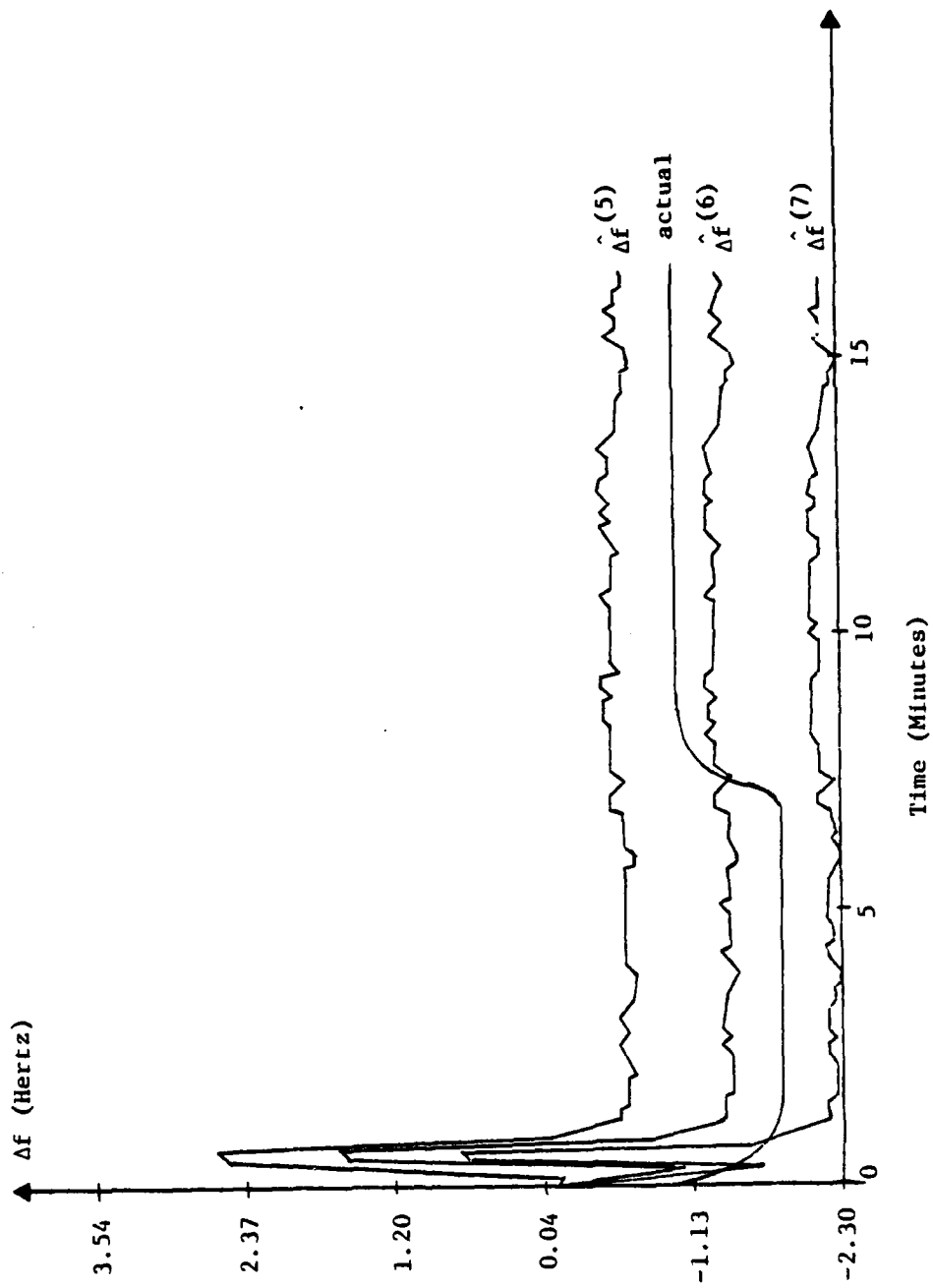


Figure 5.3.7 Actual versus Virtual Doppler Shifts in the Presence of a Source Maneuver

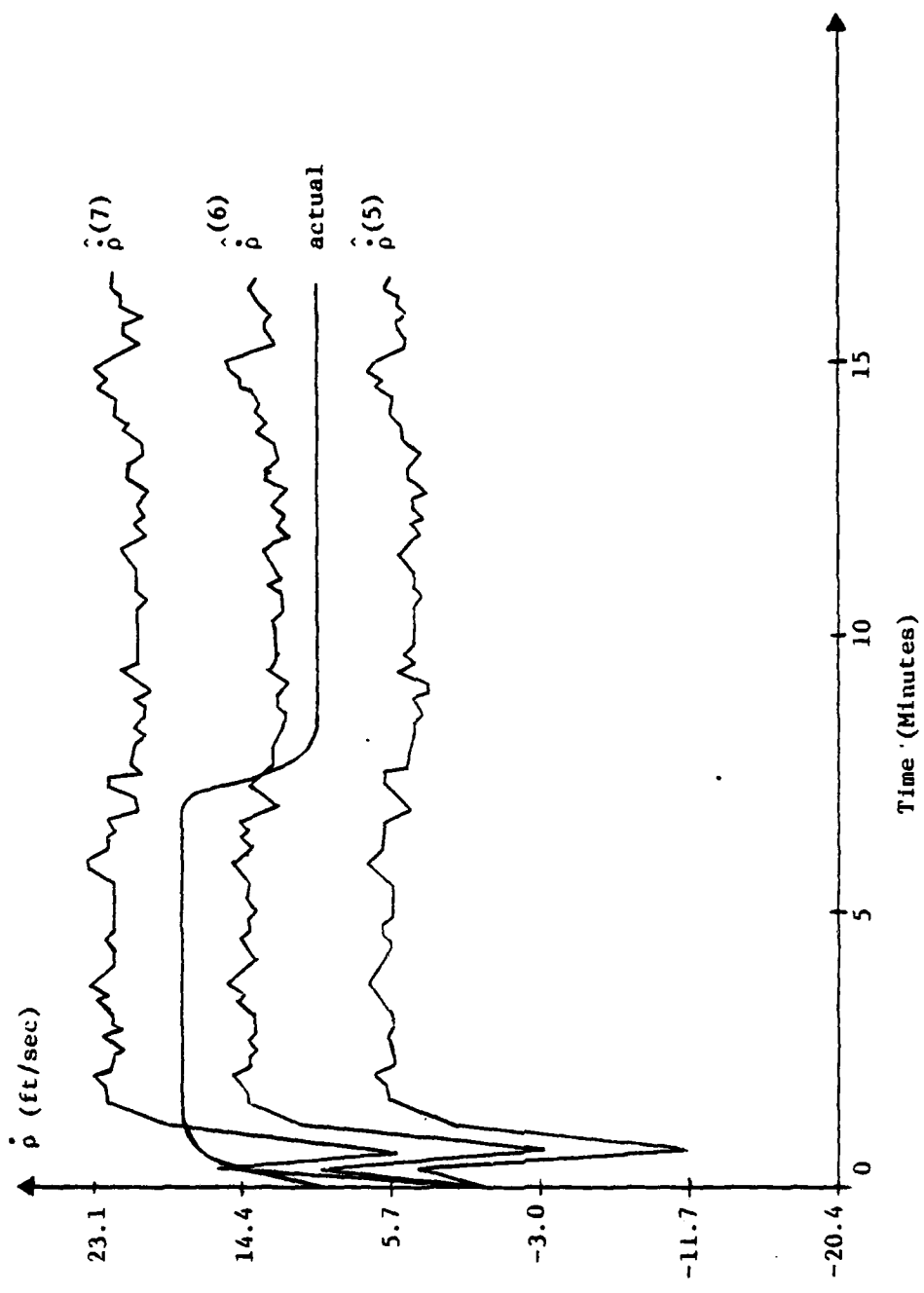


Figure 5.3.8 Actual versus Virtual Radial Velocities in the Presence of a Source Maneuver

maneuver. It has been determined that the filter bank can discriminate between a sudden change in received frequency caused by a sudden maneuver on the part of either the Source or Observer. For an Observer maneuver, the estimates adjust themselves to maintain the previously existing relative positions of the actual values versus the estimated values. For a Source maneuver, the estimates are adjusted to reflect the new position of the Source input with respect to the filter mean values.

The preceding results look at the filter's behavior from the point of view of the individual conditional estimates. Of course, in reality one does not know between which of the levels the actual Source input lies and consequently an adaptive technique must be developed before the filter can hope to be of any practical utility. However, in order to develop this adaptive technique, the mean value of the Source center frequently must first be known. The following section discusses how to obtain this information.

5.4 Determination of the Mean Value of the Source Randomly Varying Center Center Frequency

The determination of the Source center frequency mean value is of crucial importance to the problem at hand. Since the VCFs are separated by less than two Hertz, it is imperative that the method chosen yield a very accurate value for f_o .

The technique consists of using the Adaptive Extended Polar filter developed in Chapter 3. If the weighted estimate \hat{p} produced by this adaptive state estimator is averaged to yield an average value for the steady state radial velocity, then this information can be used to achieve a very accurate numerical value for $E\{f'_o\}$. To see how this works, consider

$$\bar{f}_m = \bar{f}_o [1 - \frac{\hat{p}}{C}] + \bar{v}$$

where $\bar{\rho}$ is the averaged steady state radial velocity. Substituting

$$\bar{\rho} = \frac{1}{L} \sum_{i=1}^L \hat{\rho}_i$$

for $\bar{\rho}$ and solving for \bar{f}_o we get

$$\bar{f}_o = \frac{\bar{f}_m}{\left(1 - \frac{\bar{\rho}}{C}\right)} \quad (5.4.1)$$

where it has been assumed in (5.4.1) that $\bar{v} = 0$ where \bar{v} is the average of the zero mean frequency measurement noise. This method of obtaining \bar{f}_o is very robust, and is illustrated in the next section.

5.5 The Adaptive Doppler Frequency-Radial Channel Tracking Filter for the Randomly Varying Center Frequency Case

With a method to determine a numerical value \bar{f}_o for the Source center frequency mean value now available, the last remaining problem is the development of the block labeled *Adaptive Estimator* in Figure (5.3.1). The key to this new adaptive technique is the implicit assumption that the mean value of the Source random center frequency does not change with time, or very slowly over long periods of time.

The following analysis presupposes that this mean value has already been determined by the method presented in Section (5.4.4). Consider the set of conditional estimates appearing at the output of each Doppler frequency Kalman filter in Figure (5.3.1). If each of the virtual center frequencies

$$\hat{f}_{o_k}^{(i)}, i = 1, 2, \dots, N$$

is averaged using a sliding window of length L, then the following set of average VCFs is obtained:

$$\bar{f}_{o_k}^{(i)} \equiv \frac{1}{L} \sum_{\gamma=1}^L \hat{f}_{o_{k-\gamma+1}}^{(i)}, \quad i = 1, 2, \dots, N \quad (5.5.1)$$

where k is the current iteration of the filter bank and L is the sliding window length. Now because each of these VCFs faithfully reproduces the fluctuations of f'_o during any averaging period, the average value of f'_o is bracketed between some pair of (5.5.1). This conclusion is simply a necessary result of the inequalities if

$$u_p^{(i)} < u_p < u_p^{(j)} \quad \text{then}$$

$$\bar{f}_{o_k}^{(j)} < \bar{f}_o < \hat{f}_{o_k}^{(i)} \quad (5.5.2)$$

for some set of consecutive integers (i, j) drawn from the set $(1, 2, \dots, N)$.

With the numerical value \bar{f}_o for the Source mean value f_o in hand, it is a relatively easy matter to determine the pair (i, j) after each filter iteration. This information is then used to form the following weighted estimates of the Source center frequency, Doppler shift and Source radial velocity:

$$\hat{f}_{o_k} = \frac{\hat{f}_{o_k}^{(j)} (\bar{f}_{o_k}^{(i)} - \bar{f}_o) + \hat{f}_{o_k}^{(i)} (\bar{f}_o - \bar{f}_{o_k}^{(j)})}{(\bar{f}_{o_k}^{(i)} - \bar{f}_{o_k}^{(j)})} \quad (5.5.3)$$

$$\hat{\Delta f}_k = \frac{\hat{\Delta f}_k^{(j)} (\bar{f}_{o_k}^{(i)} - \bar{f}_o) + \hat{\Delta f}_k^{(i)} (\bar{f}_o - \bar{f}_{o_k}^{(j)})}{(\bar{f}_{o_k}^{(i)} - \bar{f}_{o_k}^{(j)})} \quad (5.5.4)$$

$$\hat{s}_k = \frac{\hat{s}_k^{(j)} (\bar{f}_{o_k}^{(i)} - \bar{f}_o) + \hat{s}_k^{(i)} (\bar{f}_o - \bar{f}_{o_k}^{(j)})}{(\bar{f}_{o_k}^{(i)} - \bar{f}_{o_k}^{(j)})} \quad (5.5.5)$$

Note that $\hat{f}'_{o_k}(j)$, $\hat{f}'_{o_k}(i)$, ..., $\hat{f}'_{o_k}(i)$ are the instantaneous estimates produced by the filter in Figure (5.3.1) as distinct from the averaged estimates $\bar{\hat{f}}'_{o_k}(i)$, etc. Figure (5.5.1) gives a block diagram of this Adaptive Estimator.

To gain a further appreciation of how the Estimator works, let the Source input initially be bracketed midway between $u_s^{(j)}$ and $u_s^{(i)}$. Next let the Source input switch to a value very close to $u_s^{(j)}$. After an initial transient, the VCF $\hat{f}'_{o_k}(j)$. After an initial transient, the VCF $\hat{f}'_{o_k}(j)$ approaches in value the actual Source center frequency f'_{o_k} . This in turn means that the averaged VCF $\bar{\hat{f}}'_{o_k}(j)$ approaches the value \bar{f}_{o_k}

which implies that

$$\bar{f}_o - \bar{\hat{f}}'_{o_k}(j) \rightarrow 0$$

and

$$\hat{f}'_{o_k}(i) - \hat{f}'_{o_k}(j) + (\bar{\hat{f}}'_{o_k}(i) - \bar{f}_o)$$

The result is that the coefficient of $\hat{f}'_{o_k}(i)$ in the numerator of (5.5.3) approaches zero, and the denominator approaches in value the coefficient of $\hat{f}'_{o_k}(j)$ in the numerator.

Therefore as

$$u_{s_p} \rightarrow u_{s_p}^{(j)}$$

then the weighted estimate

$$\hat{f}'_{o_k} \rightarrow \hat{f}'_{o_k}(j) \rightarrow f'_{o_k} .$$

This same conclusion applies to the weighted shift and radial velocity estimates given in (5.5.4) and (5.5.5), respectively. Note that the Source input u_s was switched close to a mean value merely for illustrative purposes. The Source input can in reality switch anywhere within its continuum of possible values and the Adaptive Estimator will respond appropriately.

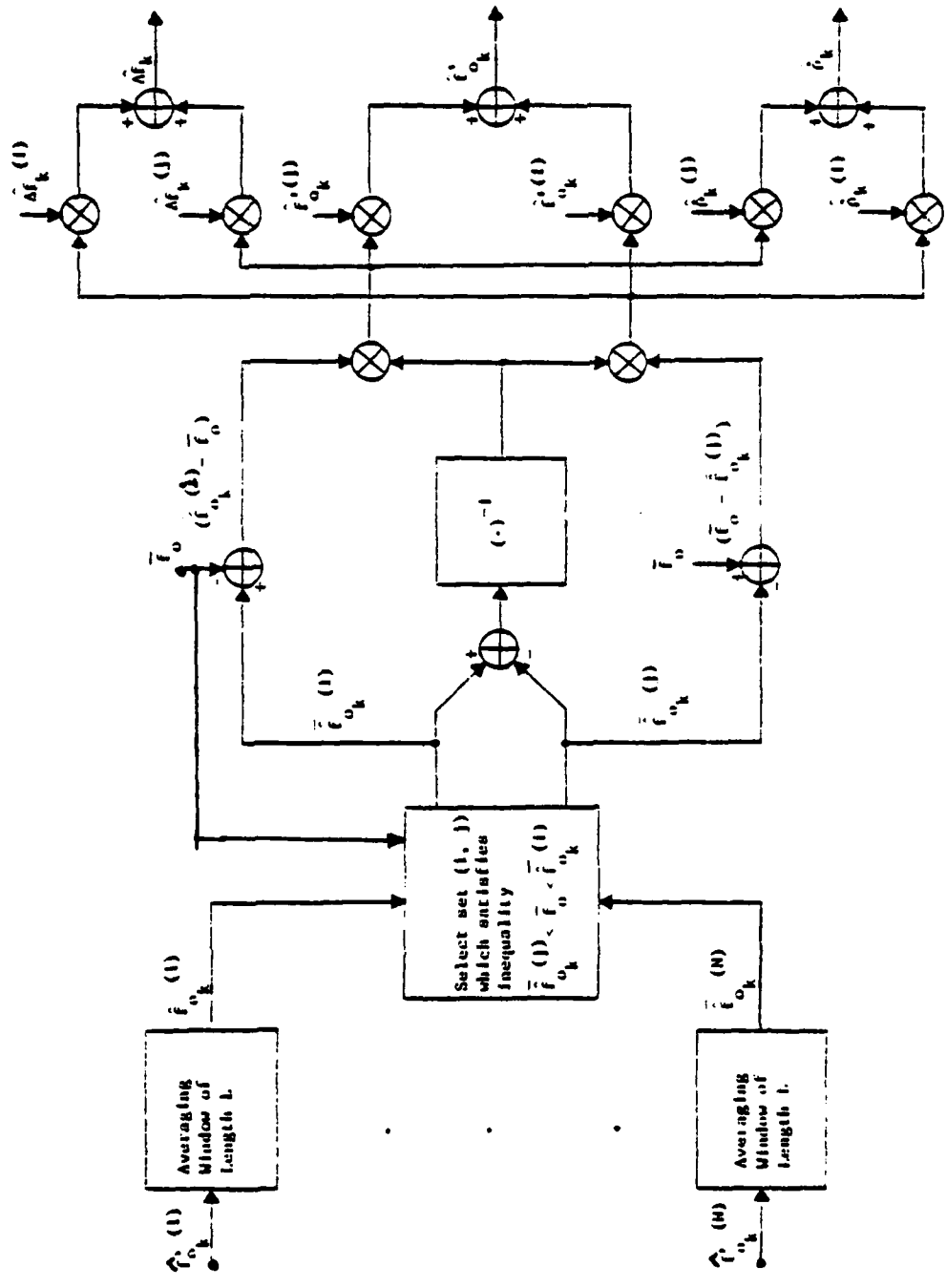


Figure 5.5.1 Block Diagram of the Adaptive Estimator for the Doppler Frequency-Radial Channel Tracking Filter

The results in the next series of figures are obtained using the scenario in Chapter 3. The quantities appearing have the values

$$z_{so} = 400 \text{ feet vertical separation}$$

$$v_o = 4 \text{ ft/sec}$$

$$v_s = 20 \text{ ft/sec}$$

$$u_{sp} = 1.0$$

The filter parameters are the same as section 3.6 and the following additional parameters have the indicated values:

$$\sigma_{f_o} = 0.1 \text{ Hertz}$$

$$\tau_{f_o} = 17 \text{ secs}$$

$$f_o = 500 \text{ Hertz}$$

C = white Gaussian random process with a mean value 4950 ft/sec

Frequency measurement noise standard deviation is the same as before.

The switch in Figure (5.3.2) is closed in order to generate the noisy frequency measurements using a random velocity of sound in water. Therefore this situation involving a non-zero vertical separation between the Observer and Source is a much more realistic scenario which when coupled with the random center frequency and random velocity of sound in water, collectively provide a realistic environment in which to test the Adaptive Estimator.

In Figure (5.5.3) the seventh, sixth and fifth VCFs are shown together with the weighted estimate produced by the Adaptive Estimator. Beginning at $t = 13.5$ minutes, the Source velocity changes to $v_s = 14 \text{ ft/sec}$ corresponding to

$$u_{sp} = (0.05)(14) = 0.7$$

which is slightly less than $u_s^{(6)}$. With the Source input initially midway between $u_s^{(6)}$ and $u_s^{(7)}$, the actual center frequency f'_o is seen to be bracketed midway between the sixth and seventh VCFs. At $t = 13.5$ minutes, the VCFs respond and by $t = 15$ minutes the sixth VCF has shifted up close to f'_o .

To understand the weighted estimate plot, first remember that the mean value of the Source center frequency must first be determined as in Section 5.4. This process is taking place in a brief time interval preceding $t = 9$ minutes (but not lasting the full 9 minutes). Consequently during this period the weighted estimate is initialized to the first measurement, like all the initial \hat{f}_o' estimates. The quantities in Equation (5.4.1) have the following computed average values:

$$\bar{f}_m = 498.396 \text{ Hertz}$$

$$\dot{\rho} = 16.134 \text{ ft/sec (obtained from averaging the Augmented Extended Polar filter estimate)}$$

Substituting these values into (5.4.1), the numerical value

$$\bar{f}_o = 500.0254 \text{ Hertz}$$

is computed for f_o . Note that while there is a slight error in $\dot{\rho} = 16.134$ -- the actual Source relative radial velocity is 16 ft/sec-- the computed mean value of $\bar{f}_o = 500.0254$ Hertz is nevertheless extremely accurate. To see how robust this method is, consider for example if the average radial velocity estimate produced by the filter of Chapter 3 were 15.0 instead of 16.134; the computed mean value in this case is

$$\bar{f}_o = 499.911$$

which is still quite good. It should be borne in mind that the sonar time delay measurements used by the Adaptive Extended Polar Filter to produce $\dot{\rho}$ are also generated using a random velocity of sound in water.

In Figure (5.5.3), the Adaptive Estimator (7.5.3) is activated at $t = 9$ minutes with the learning period completed. The weighted estimate \hat{f}_{o_k}' rises immediately to the actual center frequency and thereafter tracks f_o' very closely, even in the presence of the Source maneuver at $t = 13.5$ minutes. Note how the weighted estimate is almost identical in value to the actual f_o'

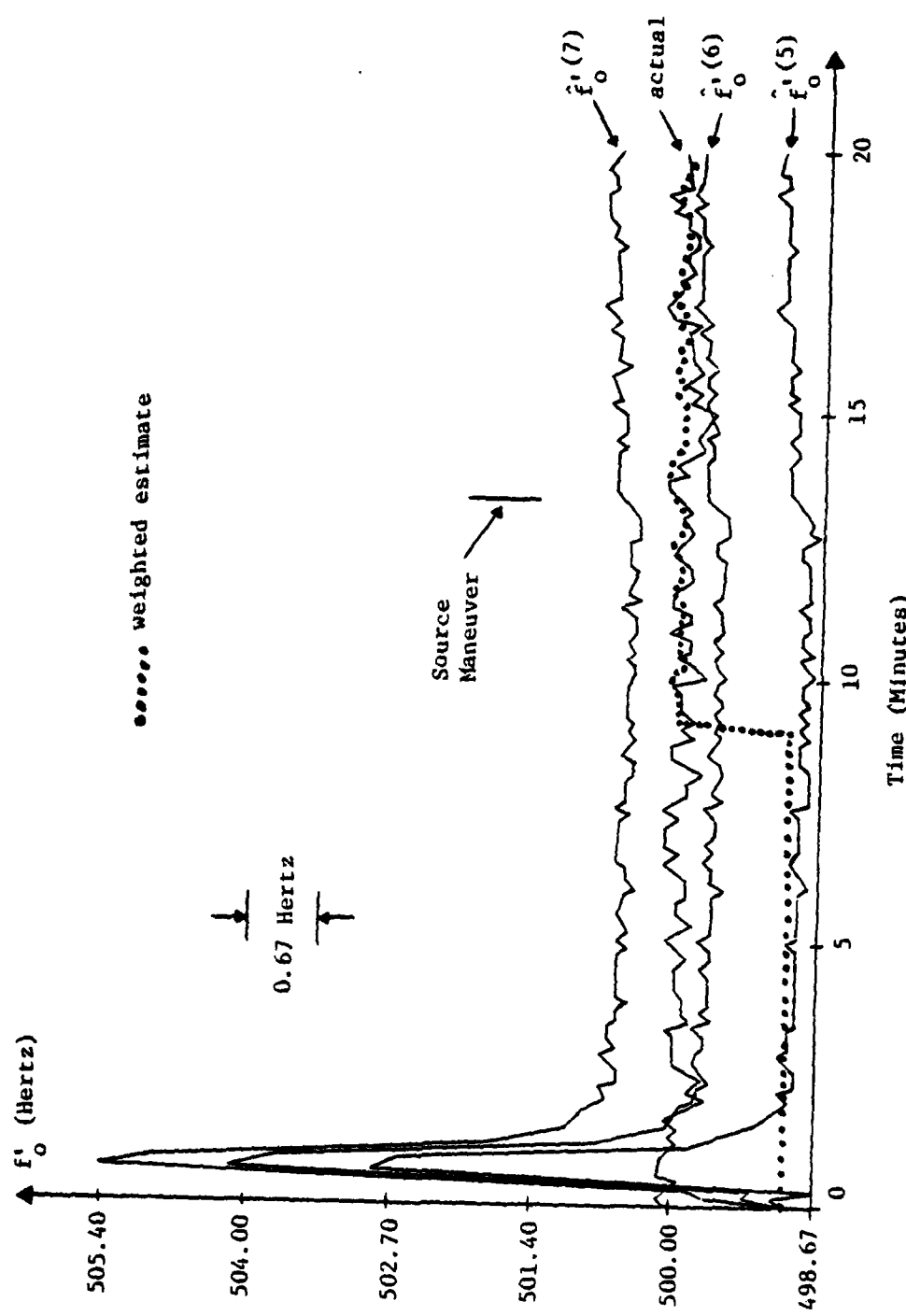


Figure 5.5.3 Actual versus Weighted Virtual Center Frequencies
in the Presence of a Source Maneuver

after the Source maneuver is completed.

In Figure (5.5.4), the Adaptive Estimator likewise produces a weighted estimate of the Doppler shift which is practically identical in value to the actual Doppler shift. The response time of this weighted estimate to the Source maneuver at $t = 13.5$ is relatively brief with only a minimum transient in the weighted estimate before learning the new Doppler shift.

The radial velocity weighted estimate \hat{p} in Figure (5.5.5) displays all the desirable qualities of the two preceding figures. The response time to the Source maneuver is excellent. Note how \hat{p} both before and after the maneuver is extremely close to the true radial velocity. The vertical scale in each figure provides a convenient gauge of the accuracy of the weighted estimates.

The Adaptive Estimator in Figure (5.5.1) can also provide weighted estimates both of the Source control input u_s and Source correlated acceleration term w_p' using the same weighting technique applied to the other state variables. For example, in the above figures the actual Source control inputs before and after the maneuver are 1.0 and 0.7 respectively. The Adaptive Estimator produces corresponding weighted estimates having the following range of values:

Before: 0.988 - 1.07

After: 0.64 - 0.81

Note that these radial velocity, control input and correlated acceleration weighted estimates would be of considerable utility in a combined sonar time delay-Doppler frequency tracking filter. Such a combination would exploit the best advantages of both filter types. For example, with the Doppler-radial channel filter providing the above weighted estimates, the order of the time delay tracker could be reduced by two from that in Chapter 3. This reduction

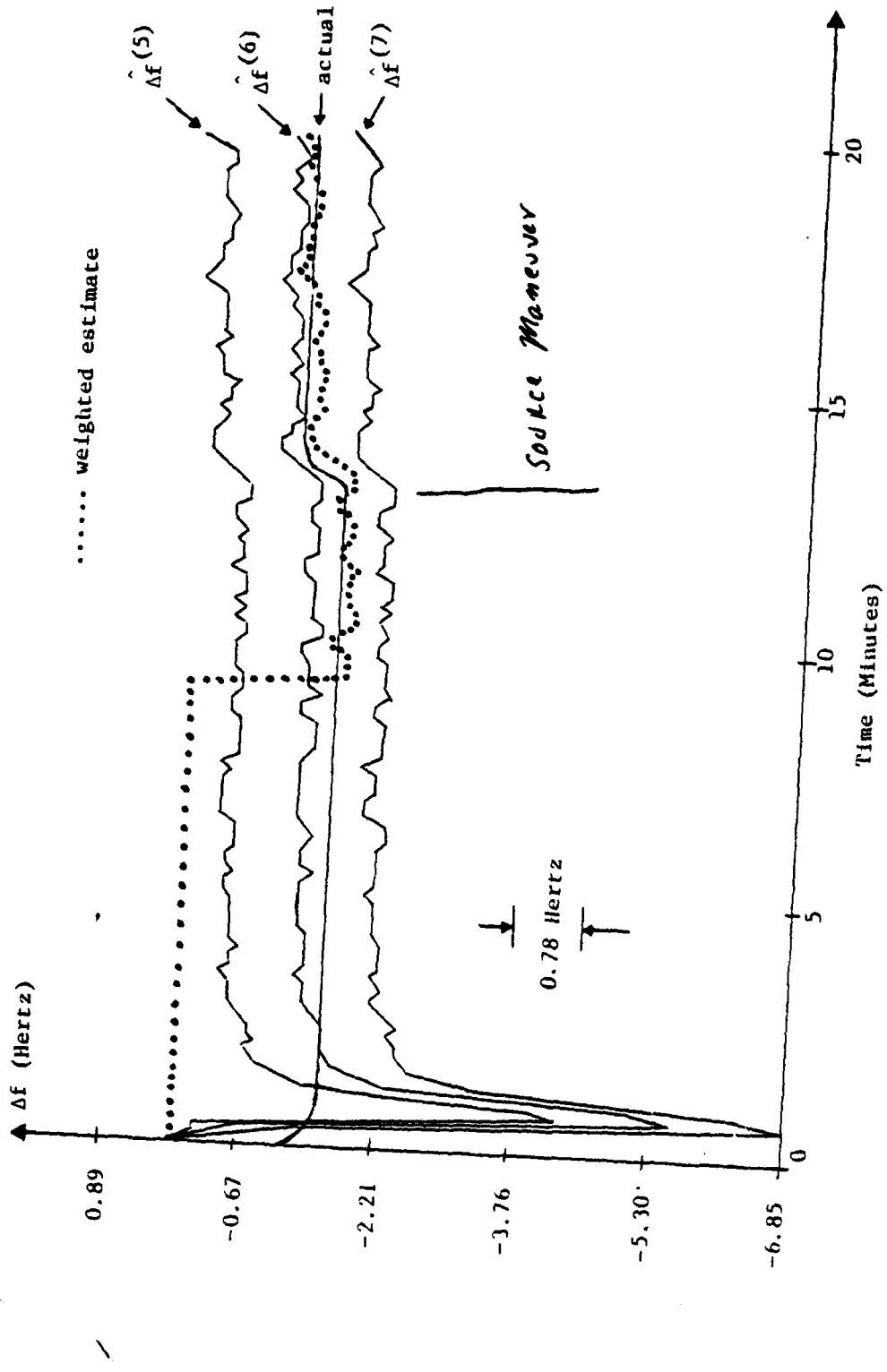


Figure 5.5.4 Actual versus Weighted Virtual Doppler Shifts in the Presence of a Source Maneuver

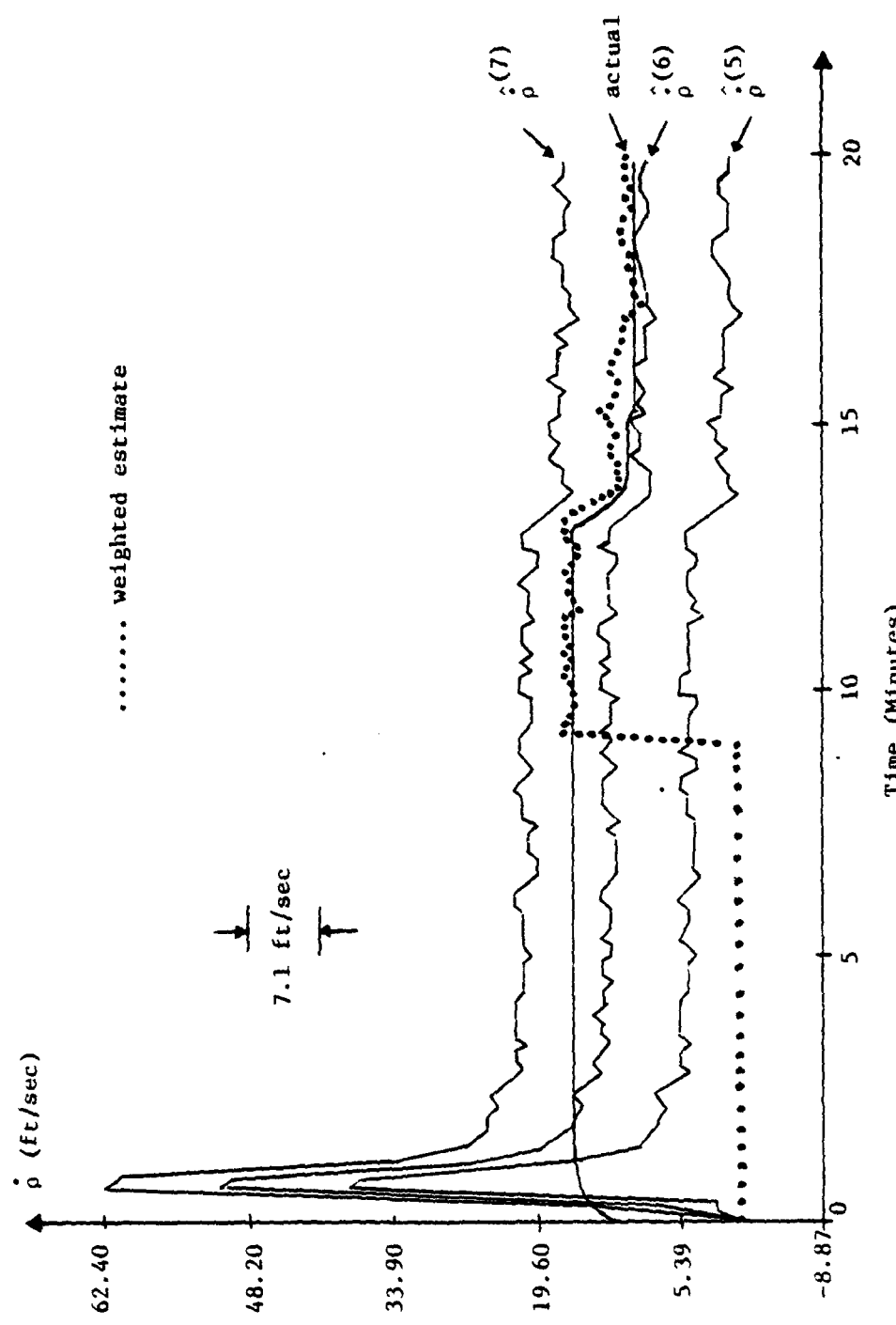


Figure 5.5.5 Actual versus Weighted Radial Velocity in the Presence of a Source Maneuver

AD-A081 253

VIRGINIA POLYTECHNIC INST AND STATE UNIV BLACKSBURG D--ETC F/8 17/1
ADAPTIVE TARGET TRACKING FOR UNDERWATER MANEUVERING TARGETS. (U)
DEC 79 R L MOOSE

N00014-77-C-0164

NL

UNCLASSIFIED

2 OF 2
AG
5001263

END
DATE
JAN 80
DEC

in order is possible because the two state variables $\dot{\rho}$, w'_{s_ρ} appearing in (3.2.1) are now estimated by the Doppler tracker. Thus the state vector for the time delay tracker would now consist of the following four state variables:

$$[\rho \quad z_{so} \quad \dot{z}_{so} \quad w'_{s_z}]^T \quad (5.5.6)$$

The high quality estimates of $\dot{\rho}$, w'_{s_ρ} and u'_{s_ρ} produced by the Doppler filter should in turn improve the performance of the time delay tracker. In addition, by embedding the adaptive feature of the combined filter in the Doppler section, the need for the semi-Markov-based weights would be eliminated. This in turn means that the oscillations in the weighted estimates experienced in Chapter 3 and which are caused by the weights switching back and forth would also be eliminated. Note that the simplified time delay tracker involves much more than a mere reduction in the size of the state vector. It also implies an elimination of all but one of the mean values in each channel. For example, the Source input would not be modeled as a single Gaussian curve in each of the ρ and Z channels. The mean values of these curves would be the Doppler provided weighted estimate of the Source input and zero, respectively. Thus the augmented approach using several levels could also be dispensed with.

Before concluding this section, the following additional comments need to be made. If it is known that the Source center frequency is a single constant tone, the modeling of this center frequency as a narrowband process is nevertheless advised in order to prevent the error covariance and Gains from becoming too small and causing divergence. The constant tone could be accurately modeled as a highly correlated random process by selecting an appropriately large (small) value for τ_{f_0} (a_{f_0}).

In obtaining the results discussed in this section, the pre-filtered measurement for the i th Radial Channel Kalman Filter in Figure (5.3.1) is obtained by subtracting the i th VCF from the received noisy frequency measurement.

Prefiltered Measurements: $(f_{m_{k+1}} - \hat{f}_{o_{k+1}}^{(i)})$, $i = 1, 2, \dots, N$

An interesting variation on this would be to use the i th virtual Doppler shift as the prefiltered measurement

Prefiltered Measurements: $\hat{\Delta f}^{(i)}$, $i = 1, 2, \dots, N$

This conceivably might improve the filter performance under high measurement noise conditions.

When the learning period is over and \bar{f}_o has been calculated, a considerable savings in computation can be achieved by cycling only the two (i, j) filters where the set (i, j) (was previously defined). When a maneuver occurs, the entire bank could be activated until the new set (i, j) has been determined, at which point $(N-2)$ filters could again be deactivated. Note that detecting Source maneuvers for activating the filter bank is a relatively simple matter because a Source maneuver is immediately heralded by a sudden shift in the measured frequency f_n as well as in the estimates produced by the two activated filters.

5.6 Conclusion

This chapter presents possibly the first attempt to solve the problem of passively tracking the radial velocity of a maneuvering Source using the Doppler effect in the presence of a randomly varying center frequency.

This problem in general is highly nonlinear, particularly if one is not careful in selecting the polar coordinate system in which to filter.

An Adaptive Estimator based on the mean values of the virtual center frequencies was developed. This Adaptive Estimator was rigorously tested under realistic environmental conditions which include a rapidly varying center frequency and velocity of sound in water modeled as a white Gaussian random process. The structure of this Adaptive Estimator is made possible by conditioning both the Doppler filter bank and radial channel filter bank estimates on the individual mean values $u_{s_p}^{(i)}$, $i = 1, 2, \dots, N$.

It is believed that the adaptive filter developed in this chapter represents the first significant attempt to deal with the random center frequency case in all of its complexities. The results obtained for a scenario involving a maneuvering Source are very encouraging and it is felt that the filter merits further study. One feature worth looking at is varying the window length in the Adaptive Estimator. The window length used here is $L = 8$, but a shorter window length might yield a still faster response. Of course, a shorter window length would also compound the oscillation problem encountered for large σ_{f_o} , so some tradeoff is called for. These small oscillations could conceivably be eliminated by averaging the output of the Adaptive Estimator using a window having a length equal to a few correlation time constants τ_{f_o} .

Another avenue of exploration is to see if some connection exists between the mean value of the center frequency and the Source dynamics. If such a relationship actually exists in practice, then proper modeling dictates that at least an approximate relationship be incorporated into the filter. Note that in this case the degree of freedom is no longer at the disposal of each filter, and consequently the semi-Markov weights can be used to compute the weighted estimates.

The characteristics of a combined Doppler frequency-sonar time delay tracking filter are investigated in the next chapter.

Chapter 6

THE INTEGRATED ADAPTIVE DOPPLER FREQUENCY-REDUCED ORDER SONAR TIME DELAY TRACKING FILTER

6.1 Introduction

In Chapter 3 the Adaptive Extended Polar Kalman Filter is developed to process sonar time delays. This filter suffers from large oscillations in the radial velocity estimates even under high signal-to-noise ratios. These oscillations prompted a search for an independent method to estimate the Source radial velocity, culminating in the Adaptive Doppler frequency tracking filter just presented. Since the Doppler measurements contain no information on the Source radial position, the Adaptive filter in Chapter 5 can provide estimates only of the Source radial velocity. Therefore, a hybrid filter formed by integrating the Adaptive Doppler and sonar time delay tracking filters offers the chance to exploit the best features of both filter types. Thus, for example, the good radial velocity estimates produced by the Adaptive Doppler filter can be used by the sonar time delay filter to produce improved estimates of both the Source radial position and Source vertical separation. To combine the two estimators the standard N level Adaptive time delay filter is initially run. Then $\hat{\rho}$ is smoothed, and used to compute \bar{f}_o in the Doppler filter. Once this period of initialization is over the standard N level filter is replaced by the reduced order state variable model where now $N = 1$ and \hat{u}_{s_p} is available. The time delay filter is derived in the next section.

6.2 State Variable Model for the Reduced Order Sonar Time Delay Tracking Filter

The Adaptive Doppler tracking filter developed in Chapter 5 provides estimates of the following quantities from the noisy frequency measurements f_m :

$$\hat{\rho}, \hat{w}'_{s\rho} \text{ and } \hat{u}_{s\rho} \quad (6.2.1)$$

Therefore the reduced order state variable vector for the sonar time delay tracker previously given is repeated here for convenience.

$$[\rho \ z_{so} \ \dot{z}_{so} \ w'_{s_z}]^T$$

Returning to the state model (3.2.1) for the time delay tracking filter, the following state equations are obtained (the subscript s_o on z_{s_o} is dropped for convenience):

$$\rho_{k+1} = \rho_k + A\dot{\rho}_k + Bw'_{s\rho_k} + Cu_{s\rho_k} + (A-T)(V_o \cos\beta_{so})_k + Dw_{s\rho_k} \quad (6.2.2)$$

$$z_{k+1} = z_k + A\dot{z}_k + Bw'_{s_z_k} + Cu_{s_z_k} + (A-T)\dot{z}_{o_k} + Dw_{s_z_k} \quad (6.2.3)$$

$$\dot{z}_{k+1} = Ez_k + Fw'_{s_z_k} + Au_{s_z_k} + (E-1)\dot{z}_{o_k} + Gw_{s_z_k} \quad (6.2.4)$$

$$w'_{s_z_{k+1}} = e^{-aT}w'_{s_z_k} + Jw_{s_z_k} \quad (6.2.5)$$

Since the quantities appearing in (6.2.1) are estimated by the Doppler tracking filter, they can be considered as "deterministic inputs" for

the reduced order sonar time delay filter. Combining these quantities with the deterministic inputs of (3.2.1) the following expanded deterministic input vector is obtained:

$$\begin{bmatrix} \vdots \\ p \\ \hat{w}_{s_p} \\ \hat{u}_{s_p} \\ v_o \cos \theta_{so} \\ u_s \\ \vdots \\ z_o \end{bmatrix} \quad (6.2.6)$$

Using this expanded input vector, the state variable model (6.2.7) (next page) emerges from the state equations (6.2.2) - (6.2.5). The corresponding linearized measurement matrix H is given in Equation 6.2.8).

$$H = \begin{bmatrix} \frac{\partial \tau_1}{\partial p} & \frac{\partial \tau_1}{\partial z_{so}} & 0 & 0 \\ \frac{\partial \tau_2}{\partial p} & \frac{\partial \tau_2}{\partial z_{so}} & 0 & 0 \end{bmatrix} \quad (6.2.8)$$

where the partial derivatives

$$\frac{\partial \tau_1}{\partial p}, \dots, \frac{\partial \tau_2}{\partial z_{so}}$$

are defined in Equations (3.3.5).

REDUCED ORDER STATE VARIABLE MODEL FOR THE SONAR TIME DELAY TRACKING FILTER

$$\begin{bmatrix} \rho \\ z_{so} \\ \dot{z}_{so} \\ w_{s_z} \end{bmatrix}_{k+1} = \begin{bmatrix} 1 & 0 & 0 & 0 \\ 0 & 1 & A & B \\ 0 & 0 & E & F \\ 0 & 0 & 0 & e^{-\alpha T} \end{bmatrix} + \begin{bmatrix} \rho \\ z_{so} \\ \dot{z}_{so} \\ w_{s_z} \end{bmatrix}_k$$

$$\begin{bmatrix} A & B & C & (A-T) & 0 & 0 \\ 0 & 0 & 0 & 0 & C & (A-T) \\ 0 & 0 & 0 & 0 & A & (E-1) \\ 0 & 0 & 0 & 0 & 0 & 0 \end{bmatrix}$$

$$+ \begin{bmatrix} \dot{\hat{\rho}} \\ \hat{w}_{s_p} \\ \hat{u}_{s_p} \\ v_0 \cos \beta_{so} \\ u_{s_z} \\ z_0 \end{bmatrix}_k$$

$$\begin{bmatrix} D \\ 0 \\ 0 \\ 0 \\ 0 \\ 0 \end{bmatrix} \begin{bmatrix} w_{s_p} \\ w_{s_z} \end{bmatrix}_k$$

(2.7)

Note that in the vector (6.2.6), u_{s_z} is no longer one of the preselected mean values $u_{s_z}^{(i)}$, $i = 1, 2, \dots, N$ but rather is the weighted estimate of the Source input produced by the Adaptive Doppler tracking filter. In addition, and for the reasons given in Section 3.2, the input u_{s_z} has the constant value

$$u_{s_z} = 0.$$

Thus neither the vector (6.2.6) nor the state model (6.2.7) is conditioned on i , and consequently only a *single* Extended Kalman filter rather than a bank of N such filters need be executed to process the noisy time delay measurements z_{τ_1} and z_{τ_2} , after the initialization or learning period is over.

6.3 Performance Analysis of the Integrated Adaptive Doppler Frequency-Reduced Order Sonar Time Delay Tracking Filter

Figure 6.3.1 gives a block diagram of the integrated Adaptive Doppler frequency-reduced order sonar time delay tracking filter. In this figure, the weighted estimates (6.2.1) produced by the Adaptive Doppler filter are fed to the reduced order sonar time delay filter where they are used in processing the noisy time delay measurements z_{τ_1} and z_{τ_2} .

The results presented in the remainder of this chapter consist of side by side comparisons between the integrated Adaptive Doppler frequency-reduced order sonar time delay filter (hereafter referred to as the hybrid filter) and the pure time delay Adaptive Extended Polar filter developed in Chapter 3. These results take the form of a series of graphs, each graph containing superimposed plots of the corresponding estimates produced by the two different filters. Thus, a very effective comparison can be made.

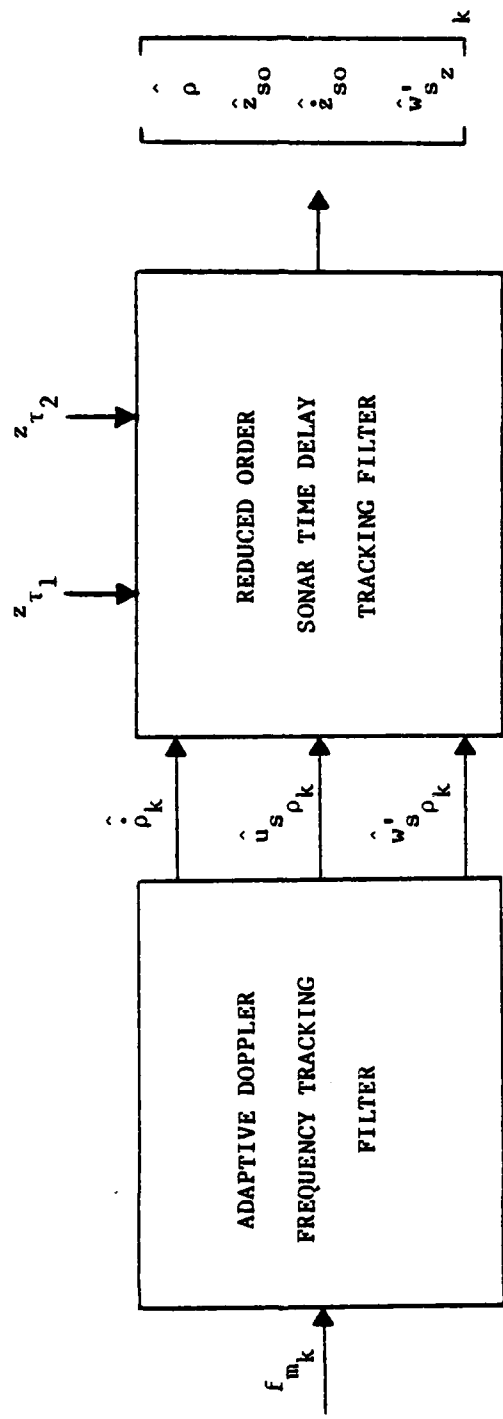


Figure 6.3.1 Block Diagram of the Integrated Adaptive Doppler Frequency-Reduced Order Sonar Time Delay Tracking Filter

Figures 6.3.2 - 6.3.4 are obtained using the filter parameters of Chapter 3, $z_{s_0} = 400$ feet, $v_o = 4$ ft/sec, $v_s = 20$ ft/sec, $b_c = 3$ ft/sec $u_{s,p} = 1.0$, $b_{f_0} = .1$ hz, $\tau_{f_0} = 17$ sec and $f_0 = 500$ hz. In addition, the random velocity of sound in water is used to generate both the noisy frequency and time delay measurement data. It should also be pointed out that the time $t = 0$ in these figures corresponds to the instant when the learning period of the Adaptive Doppler frequency tracking filter has just been completed.

In Figure 6.3.2 the percent error in Source radial position ρ produced by the pure time delay filter is larger by several orders of magnitude than that produced by the hybrid filter. Indeed, whereas the hybrid filter's errors are well within $\pm 1\%$ of the true value, the errors produced by the other filter are larger than 4% for values of $t \geq 15$ minutes.

In Figure 6.3.3 the estimates of the Source radial velocity produced by the hybrid filter are far superior to those produced by the pure time delay filter. While the hybrid estimates are generally within ± 1.5 ft/sec of the actual value (16 ft/sec), the other filter's estimates are in error by as much as ± 5 ft/sec. Note that with the adaptive feature embedded in the Doppler tracker, the hybrid filter estimates are much smoother than the wildly oscillating estimates of the pure time delay tracker, which are caused by the switching of the semi-Markov weights.

The superior performance of the hybrid filter is again evident in Figure 6.3.4 where its estimates of the Source vertical position are always within 30 feet of the actual value (400 feet). Since this error

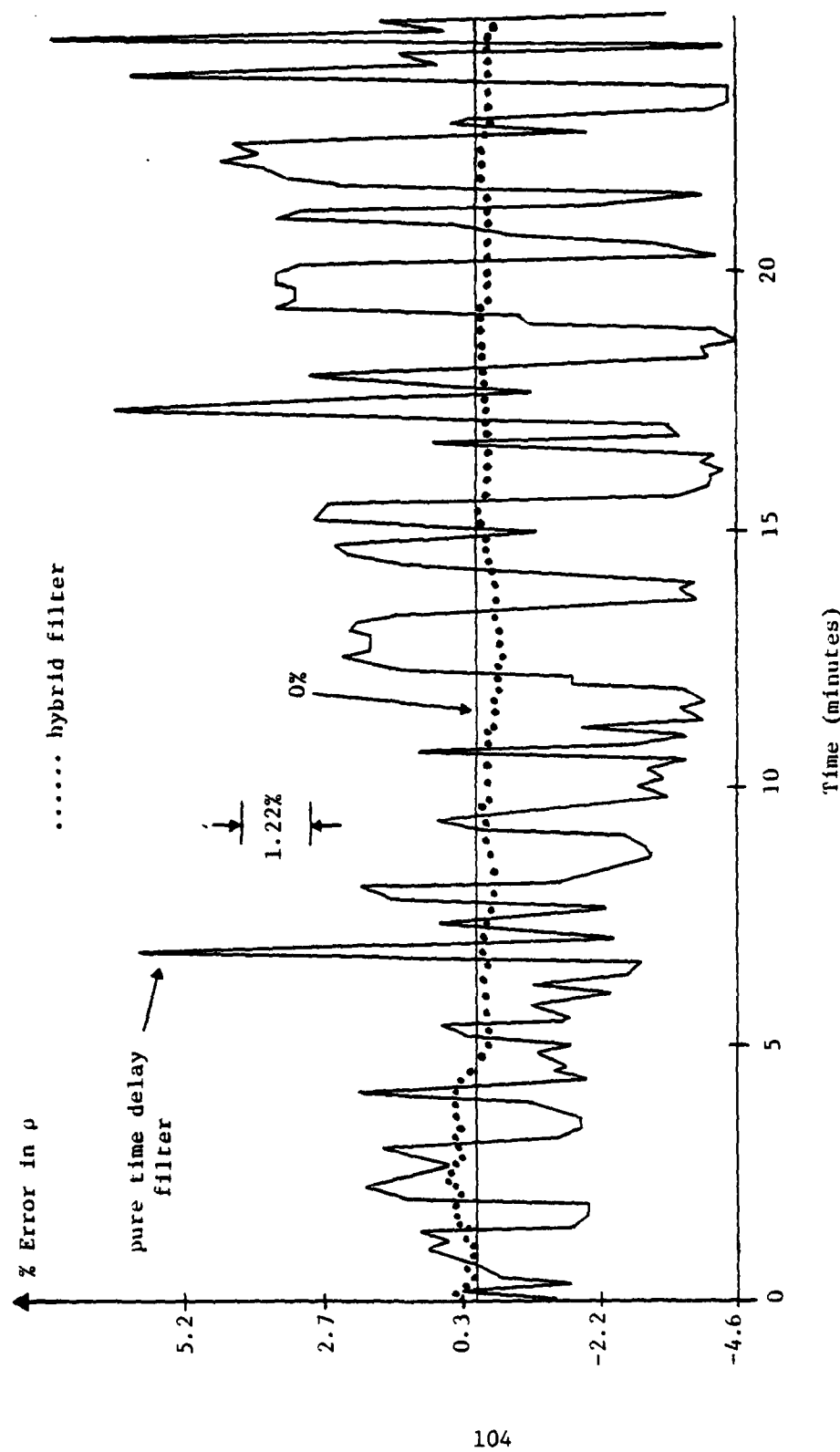


Figure 6.3.2 Percent Error in Estimates of Source Radial Position
Produced by Both Filters

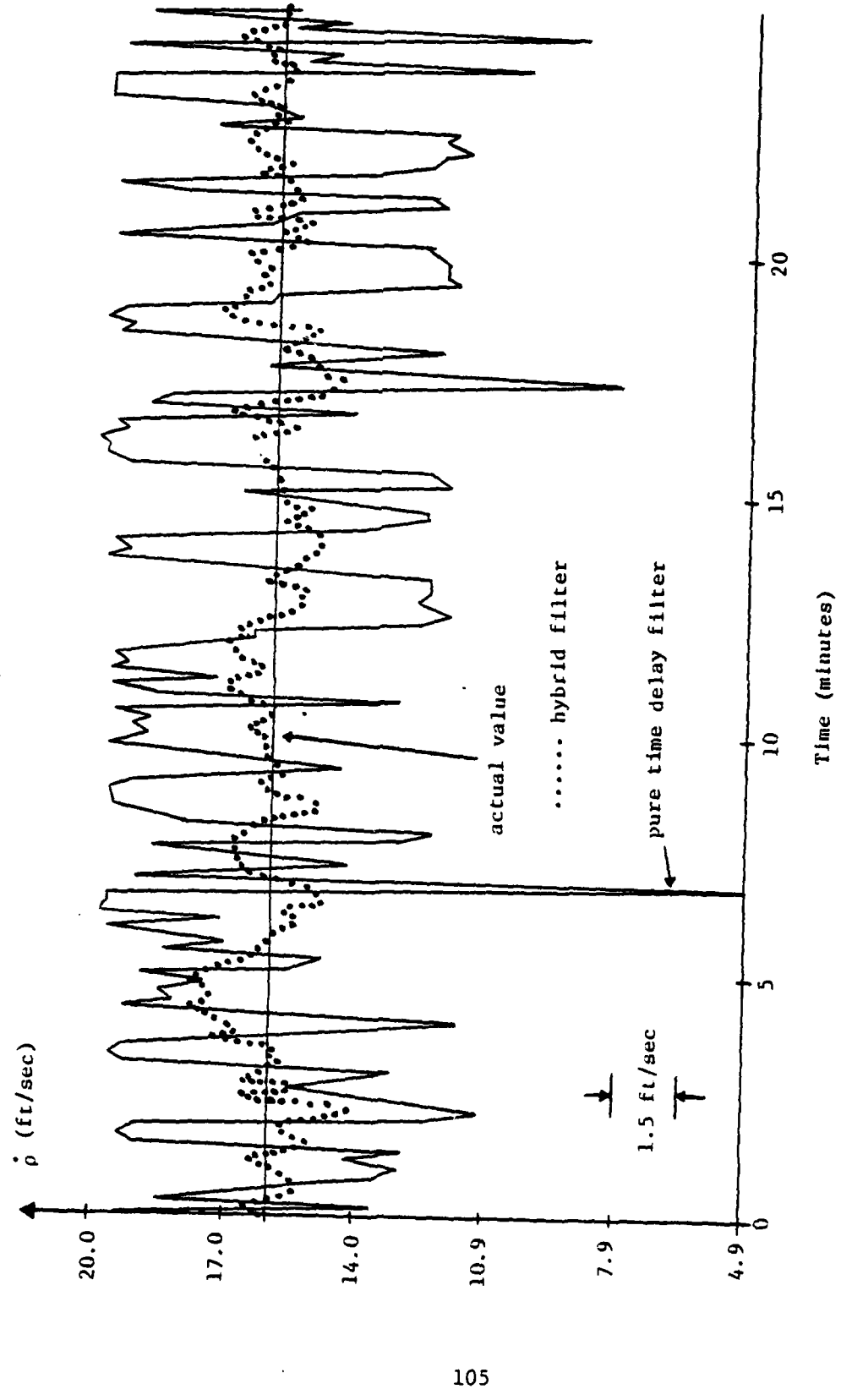


Figure 4.3.3 Estimates of Source Radial Velocity Produced by Both Filters

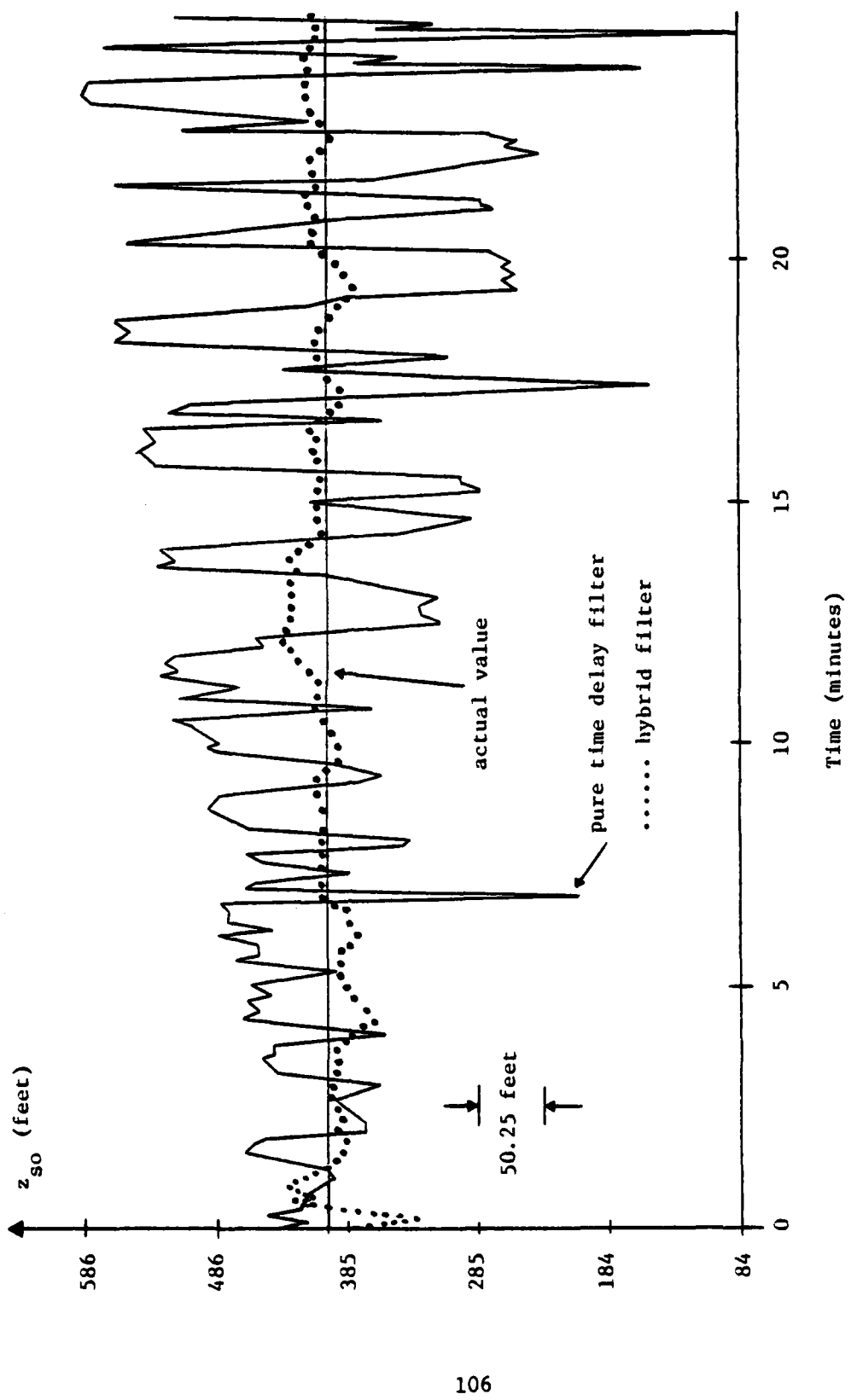


Figure 6.3.4 Estimates of Source Vertical Position Produced by Both Filters

of 30 feet is comparable to the physical height of a submarine, the error is entirely acceptable. Contrasting with this small error are the relatively large errors produced by the pure time delay filter, which for values of $t > 15$ minutes are in excess of 100 feet.

Note how in Figures 6.3.2 and 6.3.4 (and to a lesser extent in Figure 6.3.3) the estimates provided by the pure time delay filter are progressively getting poorer and poorer. For example, as time increases, the amplitude with which these estimates oscillate is getting steadily larger; near $t = 0$, the estimates are relatively close to the true values but with each iteration the estimates diverge more and more. The underlying cause of this divergence is that the signal-to-noise ratio on τ_1 is rapidly deteriorating to the point where the noisy τ_1 measurements, z_{τ_1} , are virtually useless. For example, over the period $t = 0$ to $t = 25$ minutes, τ_1 decreases from an initial value of 18 m.sec to a final value of 6 m.sec. With additive white Gaussian measurement noise having a 5 m.sec standard deviation, an initially marginal quality for τ_1 rapidly deteriorates to the point where the additive measurement noise is of the order of the quantity being measured. The following specific examples taken from the computer simulations used to produce Figures 6.3.2 - 6.3.4 serve to illustrate this point.

τ_1 (Actual Value in m.sec)	z_{τ_1} (Measured Value in m.sec)
16.3	23.3
13.7	19.6
10.7	16.6
7.0	0.1

The hybrid filter, on the other hand, performs remarkably well when confronted with these same measurements. The progressive deterioration in

the quality of the estimates encountered with the pure time delay filter is noticeably absent from the hybrid filter's estimates. In fact, the high quality of the estimates produced by the hybrid filter at the beginning of these plots when the z_{τ_1} measurements are of marginal quality, is maintained throughout the remainder of the plots even when z_{τ_1} becomes virtually useless.

The reason for the superior performance of the hybrid filter is obvious; the high quality of the estimates (6.2.1) produced by the Adaptive Doppler tracking filter (which is immune to the debilitating effects of poor quality SNR on the time delay measurement data) is sufficient to arrest the deterioration caused by the decreasing SNR on τ_1 . Thus the initial high quality of the estimates produced by the reduced order sonar time delay filter is maintained throughout the entire time period.

A factor which aids both filters in the above tests is the high SNR of the τ_2 measurements. The ocean depth of 6000' produces values of τ_2 in the range 721 m.sec - 286 m.sec.

In the next series of tests the ocean depth is reduced to 3000' with all initial conditions and filter parameters remaining unchanged. This reduction in the depth of the ocean reduces the values of τ_2 to one-fifth of their previous values. The values of τ_1 remain the same as before. Thus, coupled with an already very low SNR on τ_1 is a relatively low SNR on τ_2 . In addition, the Source executes a maneuver which causes its radial velocity (with respect to the moving Observer) to change from an initial 16 ft/sec to a final 10 ft/sec. These conditions collectively provide a much more rigorous test of both filters.

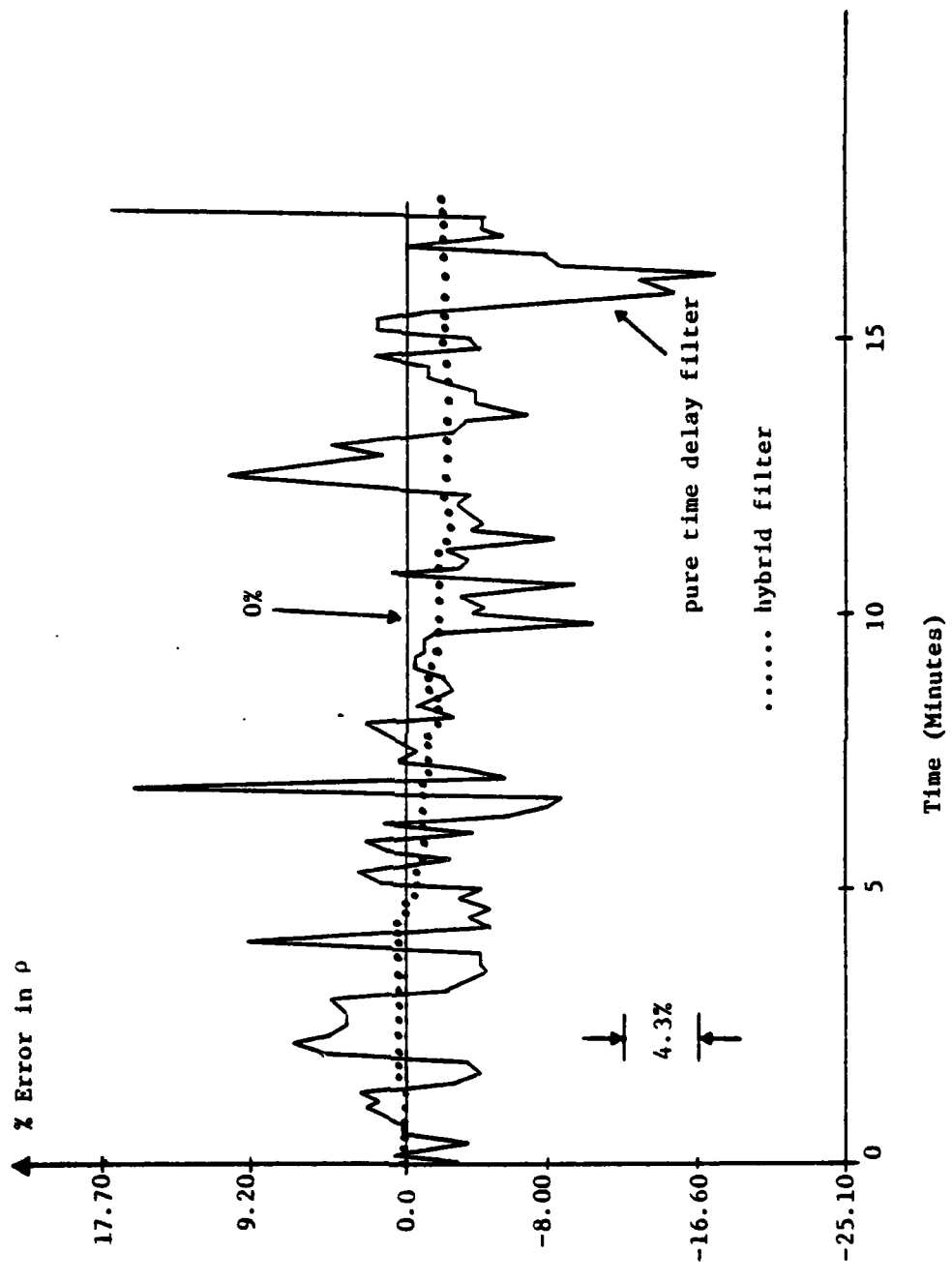


Figure 6.3.5 Percent Error in Estimates of Source Radial Position Produced by Both Filters with Very Low SNR on τ_1 and τ_2

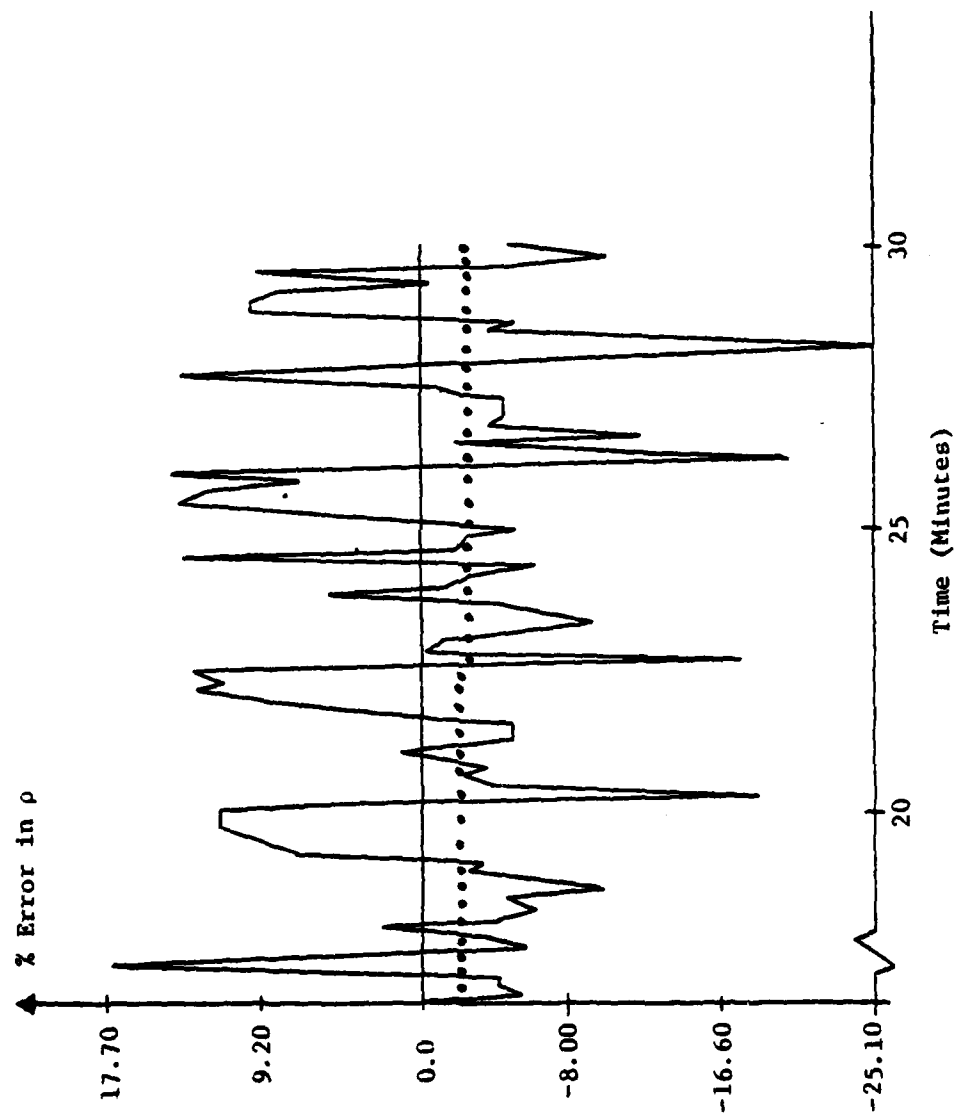


Figure 6.3.6 Continuation of Figure 6.3.5

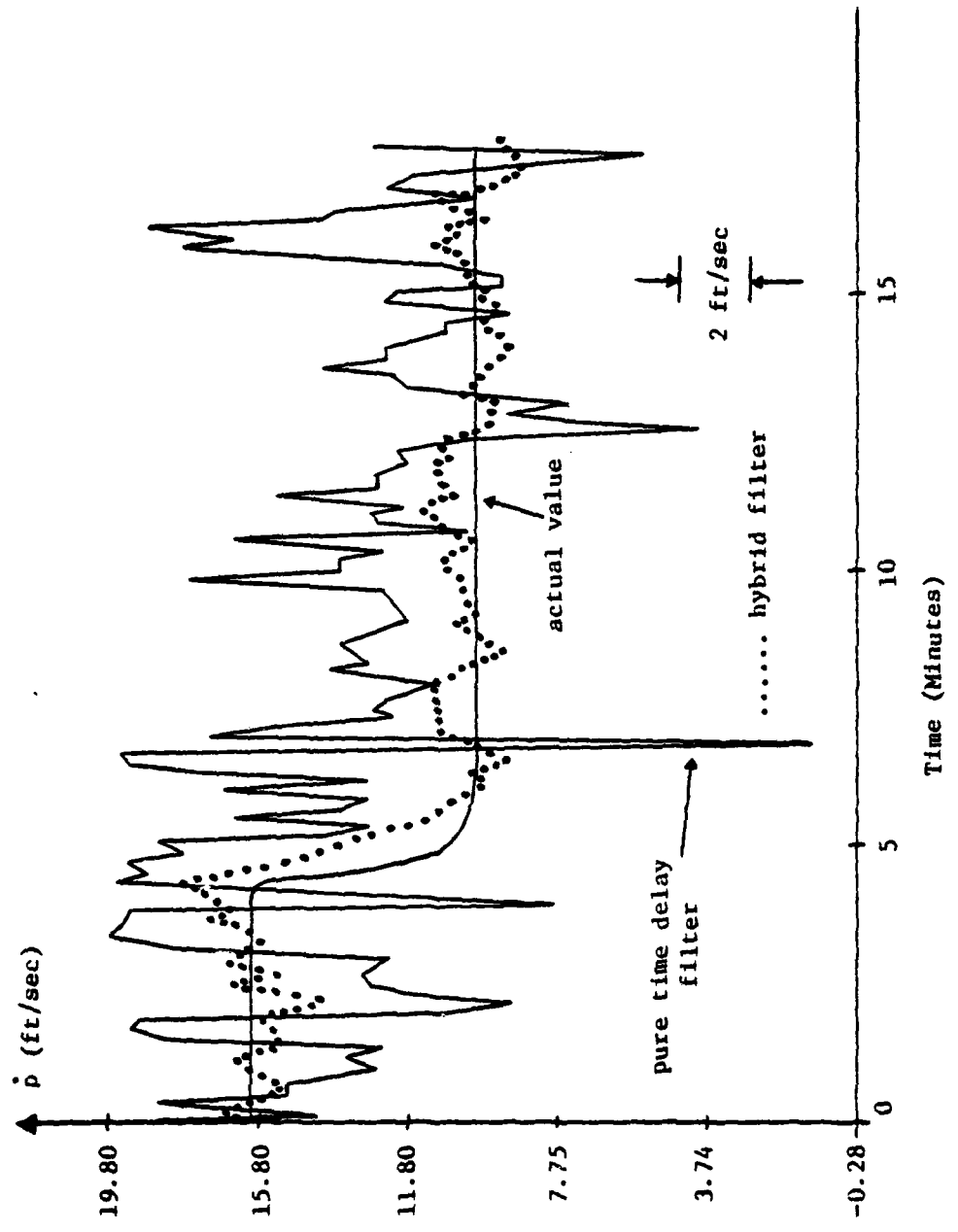


Figure 6.3.7 Estimates of the Source Radial Velocity Produced by Roth Filters with Very Low SNR on τ_1 and τ_2

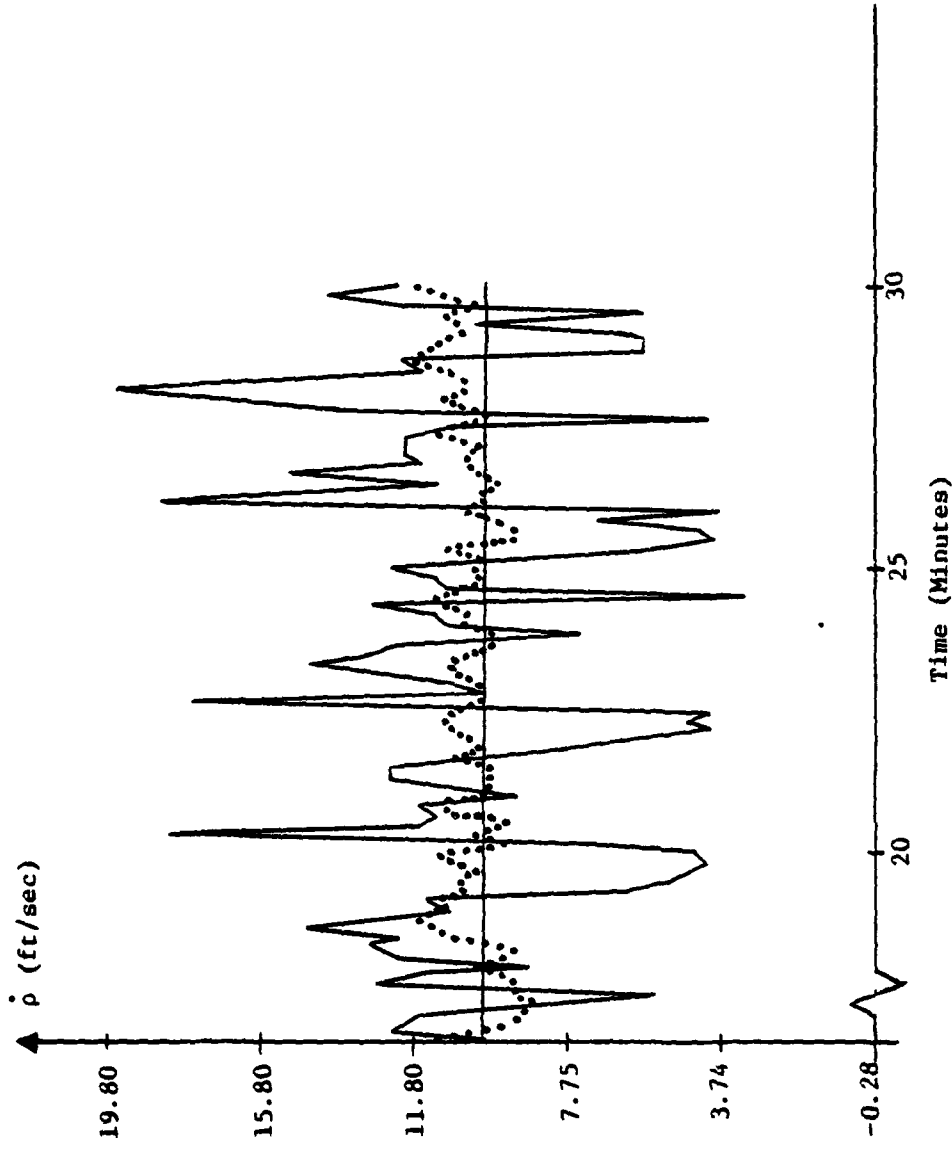


Figure 6.3.8 Continuation of Figure 6.3.7

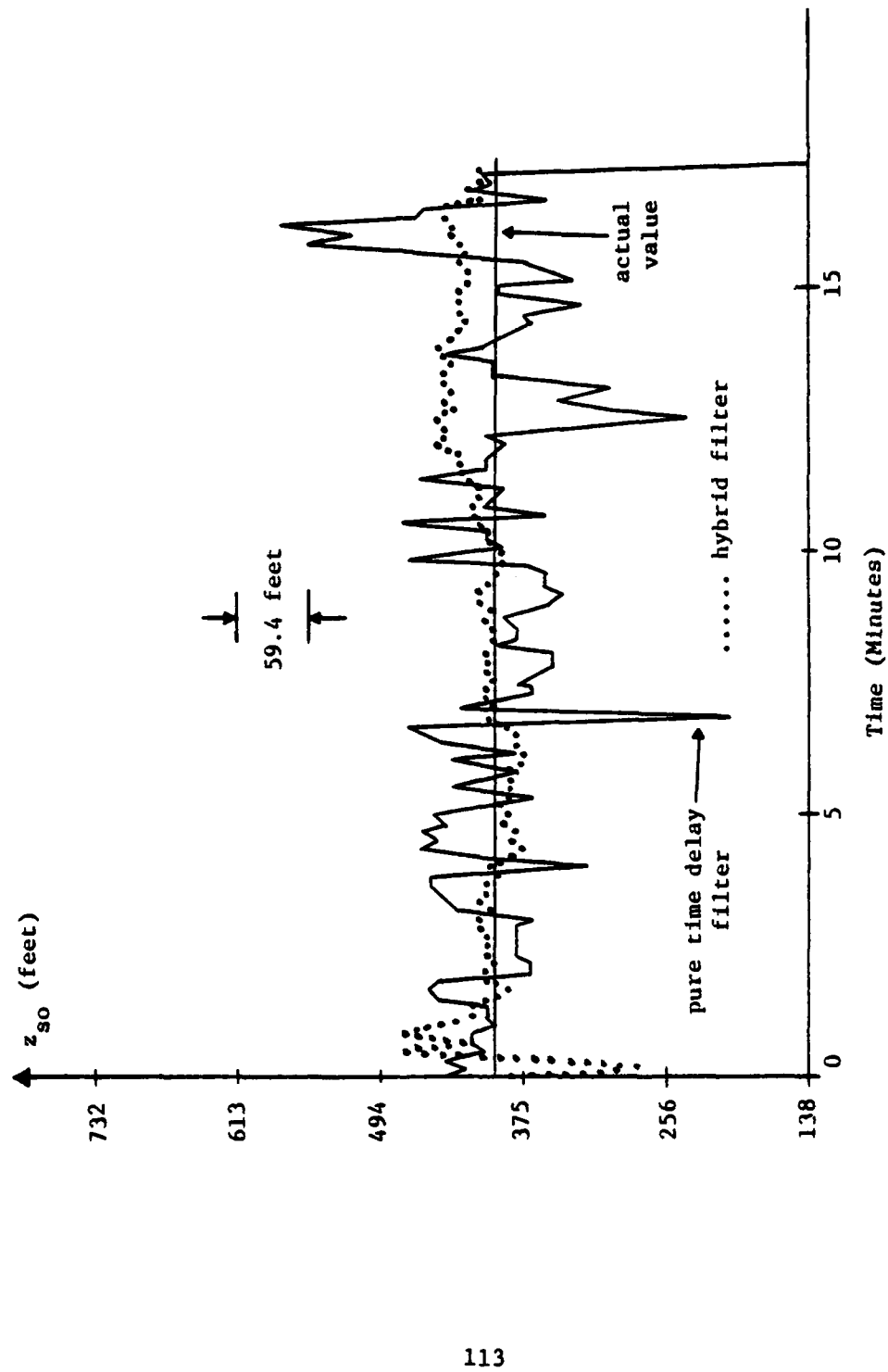


Figure 6.3.9 Estimates of Source Vertical Position Produced by Both Filters
 with Very Low SNR on τ_1 and τ_2

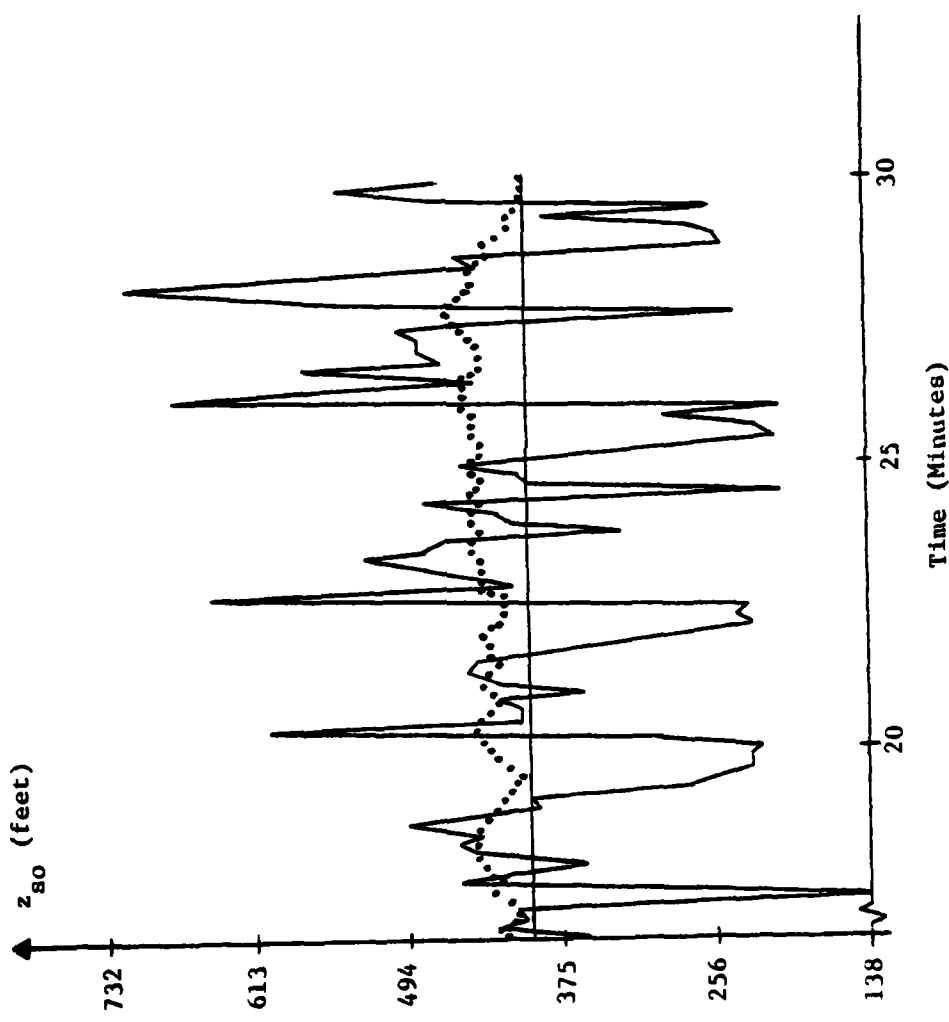


Figure 6.3.10 Continuation of Figure 6.3.9

The effect of the very low SNR on τ_2 in addition to that on τ_1 is immediately evident from Figure 6.3.5 and its continuation Figure 6.3.6 where the percent error produced by the pure time delay filter is from three to five times greater than the corresponding values in Figure 6.3.2. These large percent errors (13% - 25%) stand in marked contrast to the very small percent error (0% - 3%) produced by the hybrid filter when presented with the same measurement data.

In Figures 6.3.7 and 6.3.8 the hybrid filter's estimates of the Source radial velocity which are generally within ± 1 ft/sec of the true value are far superior to the highly oscillatory estimates produced by the pure time delay filter. The hybrid filter also responds much more rapidly to the Source maneuver at $t = 4$ minutes. For example, by $t = 6$ minutes, its estimates have converged to the new value of the Source radial velocity whereas the other filter exhibits a very sluggish response which lasts until $t = 12.5$ minutes. Thus the response time of the hybrid filter is one-fourth that of the pure time delay filter. This fast response by the hybrid filter is a direct result of embedding its adaptive feature in the Doppler frequency filter.

The estimates of the Source vertical position produced by the hybrid filter in Figures 6.3.9 and 6.3.10 continue to be generally within 30 feet of the true value. This error is entirely acceptable for the reasons stated earlier. The estimates produced by the pure time delay filter, on the other hand, are in error by several hundred feet for values of $t \geq 17$ minutes.

The progressive deterioration of the pure time delay estimates, originally encountered in Figures 6.3.2 - 6.3.4, is even more pronounced in Figures 6.3.5 - 6.3.10. The reason for this, of course, is that in

addition to a very low SNR on τ_1 , the SNR on τ_2 is much lower in the latter set of figures than is the case in Figures 6.3.2 - 6.3.4. The immunity to these low SNR ratios which the Adaptive Doppler frequency filter enjoys is what enables the hybrid filter to maintain its consistently superior performance in both series of tests.

These high quality estimates of both the Source radial and vertical positions produced by the hybrid filter under very low SNR on τ_1 and τ_2 tend to obscure the fact that the reduced order sonar time delay filter, like the pure time delay filter, is also an Extended Kalman filter. It is well known that the Extended Kalman filter algorithm displays large errors and biases under low signal-to-noise ratios. This fact makes the performance of the hybrid filter in this chapter all the more remarkable. In Figures 6.3.5, 6.3.6, 6.3.9 and 6.3.10, with a low SNR on τ_2 and an SNR on τ_1 which makes z_{τ_1} virtually useless most of the time, the estimates produced by the reduced order sonar time delay filter show a relatively small degradation compared to that suffered by the pure time delay filter. In addition, this good performance by the reduced order filter is maintained in the presence of an abrupt Source maneuver.

6.4 Conclusion

In this chapter an integrated Adaptive Doppler frequency-reduced order sonar time delay tracking filter is developed by combining the filters developed in Chapters 3 and 5. This hybrid filter exploits the best features of both constituent filters by using the high quality estimates of the Source radial velocity and control input provided by the Adaptive Doppler frequency filter to improve the

estimates of the Source radial and vertical position produced by the pure time delay filter. For example the immunity to sonar time delay measurement noise which the Adaptive Doppler frequency filter enjoys, has carried over to the reduced order sonar time delay filter. Under low SNR conditions on both time delays, the large errors in the estimates of the Source radial and vertical positions produced by the pure time delay filter of Chapter 3 are noticeably absent with the reduced order filter. In addition, the hybrid filter's response time to a maneuver by the Source is found to be one-fourth that of the pure time delay filter.

The parameter values used in this study of the hybrid filter may not be such as to yield optimal filter performance; therefore, any further investigation of this filter's characteristics should include a sensitivity analysis of these various parameters. Such an analysis might well yield a more "optimal" set than the one used here.

SUMMARY

Modeling of the target control input as a series of partially overlapping Gaussian curves worked well against air targets in the past, it was decided to apply this technique to the problem of passively tracking an underwater maneuvering Source from a moving Observer. In order to do this, it was necessary to carefully evaluate the benefits that the various coordinate systems have to offer given the generally higher nonlinear types of measurement data available for passive tracking. When polar coordinates were chosen as the most suitable coordinate system, a linearized polar model for the maneuvering Observer-

Source scenario was developed which solved the difficult problem of compensating for the Observer's own motion. This choice of polar coordinates represents a significant departure from the existing trends in the literature which generally show an unquestioned preference for rectangular coordinates. Indeed, one of the major contributions of this report is to show that for the small added complexity needed to compensate for Observer motion in polar coordinates, considerable filter simplification can be bought in the processing of all the types of available data--sonar time delays, bearing, and Source-emitted frequency spectra. With rectangular coordinates, on the other hand, where compensation for Observer motion is extremely simple, the filter is generally more complex than in the polar case. It is shown, for example, that in processing sonar time delays the linearized measurement matrix using rectangular coordinates is at least one order higher than that needed with polar coordinates.

Using partially overlapping Gaussian curves to model the Source control input and with measurement data consisting of both surface and bottom reflected sonar time delays, the estimates of the Source radial velocity produced by the polar filter were found to exhibit some oscillations even under high measurement SNR conditions.

As a result of these oscillations, a new technique using the Doppler effect was developed whereby high quality radial velocity estimates are obtained from the frequency spectra emitted by the Source. The processing of these spectra, which are either *unknown constant tones* or *narrowband random processes*, is a highly nonlinear estimation problem, which when implemented on the polar filter became linear and time varying.

Another important result of this report was to show how high quality information about the Source radial velocity and control input can be obtained from these unknown spectra using the Doppler effect. In addition, and in spite of the nonlinearity of these noisy frequency measurements, the information was obtained using only linear estimation techniques.

Next, an integrated filter was developed by combining the Doppler frequency filter with a reduced order sonar time delay filter. The estimates produced by this integrated filter are generally superior to those produced by the pure time delay filter. This superior performance was maintained under low SNR on both sonar time delays and represents a major contribution.

BIBLIOGRAPHY

- [1] A. H. Jazwinski, "Limited memory optimal filtering," IEEE Trans. Automat. Contr., vol. AC-13, Oct. 1968.
- [2] J. S. Thorp, "Optimal tracking of maneuvering targets," IEEE Trans. Aerosp. Electron. Syst., vol. AES-9, July 1973.
- [3] R. A. Singer, "Estimating optimal tracking filter performance for manned maneuvering targets," IEEE Trans. Aerosp. Electron. Syst., July, 1970.
- [4] R. L. Moose, "Adaptive estimator for passive range and depth determination of a maneuvering target (U)," U.S. Naval J. Underwater Acoustics, July 1973.
- [5] N. H. Gholson and R. L. Moose, "Maneuvering target tracking using adaptive state estimation," IEEE Trans. Aerosp. Electron. Syst., May 1977.
- [6] R. A. Howard, "System analysis of semi-Markov processes," IEEE Trans. Mil. Electron., vol. MIL-8, pp. 114-124, Apr. 1964.
- [7] R. L. Moose, H. F. VanLandingham, D. H. McCabe, "Modeling and Estimation for tracking maneuvering targets", IEEE Trans on AES, vol. AES-15-No 3. pp. 448-456, May 1979.
- [8] J. C. Hassab, "Passive Tracking of a Moving Source by a Single Observer in Shallow Water", Journal of Sound and Vibration (1976) 44 (1).
- [9] K. F. Gong, and J. S. Davis, "Evaluation of Target Motion Analysis in a Multipath Environment", NUSC Technical Report 4814, March 1976.
- [10] R. R. Tenney, et al, "A Tracking Filter for Maneuvering Sources", IEEE T.AC, Vol. AC-22, No.2, April 1977.
- [11] A. H. Jazwinski, Stochastic Processes and Filtering Theory, Academic Press, New York, 1970.
- [12] D. H. Halliday, and R. Resnick, Physics, John Wiley & Sons, Inc., New York, 1966.